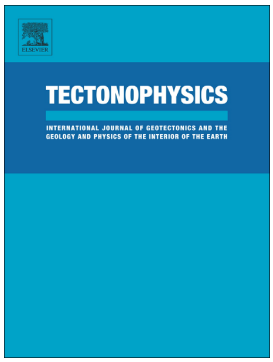

Quantitative relationship between aseismic slip propagation speed and frictional properties

Keisuke Ariyoshi, Jean-Paul Ampuero, Roland Bürgmann, Toru Matsuzawa, Akira Hasegawa, Ryota Hino, Takane Hori

PII: S0040-1951(19)30252-5
DOI: https://doi.org/10.1016/j.tecto.2019.06.021
Reference: TECTO 128151

To appear in: *Tectonophysics*

Received date: 24 January 2019
Revised date: 12 June 2019
Accepted date: 27 June 2019

Please cite this article as: K. Ariyoshi, J.-P. Ampuero, R. Bürgmann, et al., Quantitative relationship between aseismic slip propagation speed and frictional properties, Tectonophysics, https://doi.org/10.1016/j.tecto.2019.06.021

Quantitative relationship between aseismic slip propagation speed and frictional properties

Keisuke Ariyoshi[1], Jean-Paul Ampuero[2,3], Roland Bürgmann[4], Toru Matsuzawa[5], Akira Hasegawa[5], Ryota Hino[5], and Takane Hori[1]

[1]Japan Agency for Marine-Earth Science and Technology, Yokohama, Kanagawa, 236-0001, JAPAN

[2]Université Côte d'Azur, IRD, CNRS, Observatoire de la Côte d'Azur, Géoazur, 06560 Valbonne, FRANCE

[3]Seismological Laboratory, California Institute of Technology, Pasadena, CA 1125-2100, USA

[4]Department of Earth and Planetary Sciences, University of California, Berkeley, CA 94720-4767, USA

[5]Research Center for Prediction of Earthquakes and Volcanic Eruptions, Graduate School of Science, Tohoku University, Sendai, 980-8578, JAPAN

Corresponding author: Keisuke Ariyoshi (ariyoshi@jamstec.go.jp)

Quantitative relationship between aseismic slip propagation speed and frictional properties

Abstract

Recent observations show evidence of propagation of postseismic slip, which may contain information about the mechanical properties of faults. Here, we develop a new analytical relationship between the propagation speed of aseismic slip transients and fault frictional properties, modeled by a rate- and state-dependent friction law. The relationship explains the propagation speed of afterslip in 3-D numerical simulations to first order. Based on this relationship, we identify systematic dependencies of afterslip propagation speed on effective normal stress σ and frictional properties (the coefficients a and a-b which quantify the instantaneous and the steady-state velocity-dependence of friction, respectively, and the characteristic slip distance L of fault state evolution). Lower values of the parameter $A=a\sigma$ cause faster propagation in areas where the passage of the postseismic slip front induces large shear stress changes $\Delta\tau$ compared to A, which are typically located near the mainshock rupture. In areas where $\Delta\tau/A$ is small, typically more distant from the mainshock, afterslip propagation speed is more sensitive to $(a\text{-}b)\sigma$. The propagation speed is proportional to initial slip velocity and, under the condition that loading span is significantly shorter than the passage of postseismic slip, inversely proportional to L. The relationship developed here should be useful to constrain the frictional properties of faults based on observed propagation speeds, independently of rock laboratory experiments, which can then be used in predictive numerical simulations of aseismic slip phenomena.

1 Introduction

Thanks to the development of computational capabilities, numerical simulations of earthquake cycles based on rate- and state-dependent friction laws (RSF laws) (Dieterich, 1979; Ruina, 1983) are now a useful tool to understand complexities of fault slip. In particular, such models are useful to study the development of afterslip and its effect on driving aftershock sequences and triggering earthquakes (e.g, Kato, 2008; Ariyoshi et al., 2007a, 2015; Hyodo et al., 2016; Nakata et al., 2016). Relationships between aftershock seismicity rate and afterslip have been proposed in the framework of RSF models (e.g., Perfettini and Avouac, 2004, 2007). Lui and Lapusta (2016) demonstrate that in RSF models the shear stress increase due to postseismic slip affects the time advance of a triggered earthquake more strongly than the static stress increase caused by coseismic slip. To explain the space and time lag of triggered earthquakes, as observed for the 2003 off Tokachi – 2004 off Kushiro earthquakes (Murakami et al., 2006), the 1999 Izmit - Düzce earthquakes (Hussain et al., 2016; Hearn et al., 2002), and the 2004 Sumatra-Andaman – 2005 Nias earthquakes (Konca et al., 2008), it is important to know the propagation speed of postseismic slip that encourages their occurrence. However, such computational studies require many trial simulations (e.g., Kato, 2008; Dublanchet et al., 2013; Kaneko et al., 2013; Nakata et al., 2016) because a well-established relationship between frictional properties and afterslip propagation speed is lacking. In addition, earthquake triggering may be affected by changes of effective normal stress σ due to thermal pressurization and by their influence on stress drop (Lui and Lapusta, 2018), thus it is also necessary to understand the relationship between effective normal stress and afterslip propagation.

Previous numerical simulation studies have investigated the relationship between frictional properties and postseismic slip propagation, but have reached apparently discrepant conclusions. In RSF models, postseismic slip can be produced on the fault areas surrounding the mainshock rupture if they are frictionally stable, i.e. if their frictional parameter a-b, which quantifies the logarithmic-velocity-dependence of steady-state friction, is positive (Marone et al., 1991; Boatwright and Cocco, 1996). Kato (2004, 2007) concludes that the propagation speed decreases with distance from the mainshock rupture and with increasing values of $(a\text{-}b)\sigma$. This result is useful to estimate the value of $(a\text{-}b)$ assuming a value of σ (Dublanchet et al., 2013). On the other hand, Ariyoshi et al. (2007b) show that for a given value of $(a\text{-}b)$ the postseismic slip propagation speed depends separately on a and b, two parameters that quantify

the instantaneous velocity-dependence and the state-dependence of friction, respectively (see also Figure 3 in section 2.2).

Previous theoretical analysis has provided important insight into the problem of aseismic slip migration speed in RSF models. Shibazaki and Shimamoto (2007) found that afterslip propagation speed is proportional to the maximum slip velocity reached near the propagating front. Ampuero and Rubin (2008) introduced the relationship between propagation speed, maximum slip velocity and frictional properties in the context of RSF. These relationships are useful to infer frictional properties when both slip velocity and propagation speed have been observed, but do not allow a prediction of afterslip speed based only on friction parameters.

In this study, to advance our capabilities to infer fault properties from afterslip observations and to design realistic aseismic slip models, we develop a theoretical relationship between the postseismic slip propagation speed and frictional parameters of the RSF law, with approximations derived from results of earthquake cycle simulations. We also discuss the validity of the approximations, and use our new theoretical insight to interpret the results of previous numerical studies.

2 Model and numerical simulation method

To exclude complicating factors and isolate the effects of the frictional parameters of the RSF law on the postseismic slip propagation process, we adopt the simplified 3-D subduction plate boundary model of Ariyoshi et al. (2007b), which assumes homogeneous frictional properties in the region of postseismic slip. In this section, we review the simulation method, which is basically the same as in previous 3-D models (Hirose and Hirahara, 2002, 2004; Ariyoshi et al., 2007a) based on the quasi-dynamic approximation (Rice, 1993).

2.1 3-D plate boundary model

Our model involves a planar plate interface in a homogeneous elastic half-space, dipping 20 degrees from the free surface. The region of interest on the fault, in which a friction law is enforced, is divided into a grid of non-overlapping sub-faults (Figure 1). For simplicity, slip is limited to pure thrust slip. Outside this region the fault is assumed to slip at steady velocity V_{pl} given by the long-term plate convergence slip rate. In the quasi-dynamic approximation (Rice, 1993) the relation between along-dip shear stress τ_i at the center of the

i-th sub-fault at time *t* and slip u_j at the center of all sub-faults (all symbols used are listed in Table 1) is

$$\tau_i = \sum_{j=1}^{N} K_{ij}\{u_j(t) - V_{pl}t\} - \frac{G}{2\beta}\frac{du_i}{dt}, \quad (1)$$

where *N* is the total number of sub-faults and K_{ij} is a matrix of static stress transfer coefficients given by static dislocation theory (Okada, 1992) relating shear stress at the *i*-th sub-fault to the slip deficit at the *j*-th sub-fault relative to the convergence slip rate V_{pl} (Savage, 1983). The last term in Eq. (1) is introduced to incorporate radiation damping (Rice, 1993). *G* is rigidity, and β is the S wave speed.

Table 1. Symbols in Order of Appearance

Symbol	Definition	Value or Dimension	First Appearance
i	Index of focused (receiver) sub-fault	N.D.	(1)
j	Index of source (dislocation) sub-fault driving shear stress	N.D.	(1)
τ	Shear stress loaded by dislocation	Pa	(1)
K_{ij}	Green's function for static dislocation(i: receiver, j: source)	Pa/m	(1)
u	Amount of pure dip slip, uniform over a sub-fault	m	(1)
t	Time	sec	(1)
V_{pl}	Averaged plate convergence rate	1.3×10^{-9} m/sec	(1)
G	Rigidity	30 GPa	(1)
β	Shear wave speed	3.75 km/sec	(1)
μ	Friction coefficient	N.D.	(2)
σ	Effective normal stress	Pa	(2)
ρ_{r}	Density of rock	2.75×10^{3} kg/m	(3)
ρ_{w}	Density of water	1.0×10^{3} kg/m	(3)
g	Gravity acceleration	9.8 m/sec^2	(3)
z	Depth from free surface	m	(3)
a	Frictional parameter for the direct effect of RSF	N.D.	(4)
b	Frictional parameter for the evolution effect of RSF	N.D.	(4)
L	Characteristic slip distance of RSF	m	(4)
θ	State variable of RSF	sec	(4)
V_0	Reference slip velocity	1 μm/s	(4)

μ_0	Reference frictional coefficient at $V = V_0$	0.6	(4)
v	Poisson's ratio	0.25	Section 2.1
Δ_X	Grid size in the test simulation	m	Section 2.1
Δs	Release zone size	m	Figure 5ab
η	Geometrical factor	N.D.	(6)
$V_{\mathrm{slip}}^{\mathrm{max}}$	Maximum value of slip velocity (V)	m/sec	(7)
V_{prop}	Propagation speed of aseismic slip	m/sec	(7)
$\Delta\tau_b$	Breakdown stress drop	Pa	(7)
C	Constant value relating between $V_{\mathrm{slip}}^{\mathrm{max}}$ and V_{prop}	N.D.	(7)
$\Delta\tau$	Stress drop amount from the peak value as shown in Figure 5c	Pa	Section 2.3
$V_{\mathrm{prop}}^{\mathrm{sim}}$	Propagation speed of postseismic slip in the test simulation	m/sec	(7)
ΔT_i	Delay time at i-th point for postseismic slip passage	sec	Figure 5d
T	Total delay time along the propagation path	sec	Section 3.1
k	Spring stiffness of background loading on a slider in Figure 5b	Pa/m	(9)
x	Displacement of a slider in Figure 5b	m	(9)
V_{b}	Background loading velocity due to the plate motion	m/sec	(9)
f	Time history of normalized triggering displacement	N.D.	(9)
θ_{init}	Initial condition of state variable	sec	(14)
γ	Instability factor ($\gamma < 0$; not trigger postseismic slip)	m^{-1}	(16)
V_{fact}	Amplitude of slip velocity for an exponential function	m/sec	(17)
μ_{init}	Initial condition of frictional coefficient	N.D.	(17)
$V_{\mathrm{slip}}^{\mathrm{init}}$	Initial slip velocity (V) at the Surge Period in Figure 5c	m/sec	(20)
$\Delta\tau_0$	Shear stress increase in the Approach period	Pa	(23)
R, R'	Loading rate of friction coefficient in Figure 5d	1/sec	(24)
α	Ratio of R to R'	N.D.	(24)
F_{ramp}	Loading term in case of ramp function	N.D.	(27)
F_{step}	Loading term in case of step function	N.D.	(35)
V_{approx}^{step}	Applied approximation of $(V_{slip}^{init} \sim V_{pl})$ to V_{prop}^{step}	m/sec	(42)
V_{rough}^{step}	Applied approximation of $(\gamma \approx b/d_c)$ to V_{approx}^{step}	m/sec	(43)
V_{rough}^{linear}	Applied approximation of $(\gamma \approx b/d_c)$ to V_{prop}^{linear}	m/sec	(44)
V_{simple}^{step}	Approximation without Δs from the result of Figure 16	m/sec	(45)
V_{const}	Constant propagation speed (0.1-10 km/month in our model)	m/sec	(45)

Note. N.D. means Non Dimensional.

In RSF the shear stress is always equal to the frictional strength:

$$\tau = \mu\sigma, \quad (2)$$

where μ is the friction coefficient and σ the effective normal stress. Assuming hydrostatic fluid pressure, σ is given by

$$\sigma_{zz}(z) = (\rho_r - \rho_w)gz, \quad (3)$$

where ρ_r and ρ_w are the densities of rock and water, respectively, g is gravitational acceleration and z is depth and, given the shallow dip angle of the megathrust, we neglect the contribution of the horizontal component σ_{yy}. The friction coefficient is assumed to follow the RSF law (Dieterich, 1979; Ruina, 1983):

$$\mu = \mu_0 + a \log(V/V_0) + b \log(V_0\theta/L), \quad (4)$$

where V is the slip velocity, θ is a state variable, μ_0 is a reference friction coefficient at constant reference slip velocity V_0, a and b are friction parameters quantifying the importance of direct and evolution effects, respectively. To avoid computational instability at low slip velocity close to V=0 in Eq. (4), we set V_0=1 μm/s, a value comparable to postseismic slip velocity. The state variable is assumed to obey the aging (slowness) version of the state evolution equation (Ruina, 1983; Beeler et al. 1994):

$$d\theta/dt = 1 - V\theta/L, \quad (5)$$

where L is a characteristic slip distance of state evolution. Multiple state evolution laws have been proposed and their adequacy is still an active topic of research (e.g. Bhattacharya and Rubin, 2014). Our choice of Eq. (5) is primarily driven by its mathematical tractability in the derivation of analytical relationships that can provide useful insight into the problem. In particular, we do not account for possible stress-weakening effects (Nagata et al., 2012).

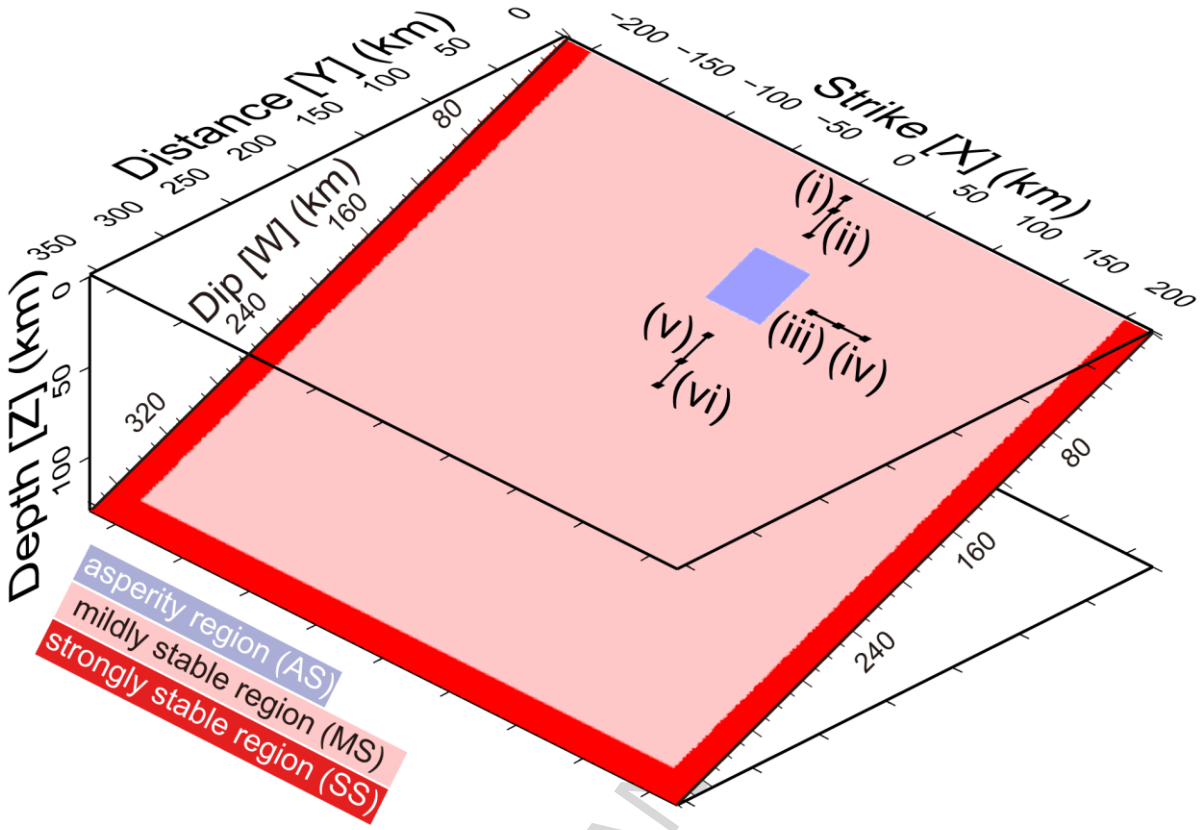

Figure 1. A numerical model of earthquake cycles on a subduction plate boundary dipping at 20 degrees (after Ariyoshi et al. (2007b)). The values of frictional parameters (a, b, L) are (0.002, 0.00272, 4 cm) for the asperity region (AS) and (0.005, 0.0001, 4 cm) for the strongly stable region (SS) and variable parameters as listed in Table 2 for the mildly stable region (MS). The coordinates (X, W) of the six segments are: (i): (0, 10) — (0, 20), (ii): (0, 20) — (0, 40), (iii): (40, 80) — (60, 80), (iv): (60, 80) — (80, 80), (v): (0, 120) — (0, 140), (vi): (0, 140) — (0, 160).

We solve the equations above using the Runge-Kutta method with adaptive step size control (Press, et al., 1992). The parameter values common to all the models presented here are listed in Table 1.

Since our aim is to focus on the postseismic slip process associated with a large earthquake, our fault model comprises three regions as shown in Figure 1: the asperity region (AS), the surrounding mildly stable region (MS), and the more distant strongly stable region (SS). In our reference model, a=0.002 and b=0.00272 in region AS, such that it is velocity-weakening (a-b<0) to allow for the nucleation of large earthquakes. The MS and SS regions are velocity-strengthening (a-b>0). In MS, a=0.002 and b=0.0019 such that a~b,

which promotes postseismic slip over an extended area. In SS, a=0.005 and b=0.0001 such that $a>>b$, which keeps the slip velocity close to steady at the outskirts of the model domain, smoothly transitioning to the constant slip velocity (V_{pl}) assumed outside. The characteristic slip distance is L =40 mm in all the regions in the reference model.

The computational grid size (Δ_X, the size of a sub-fault) is 2.5 km in SS, 1.25 km in MS, and 0.67 km in AS. The scale of Δ_X in AS is five times smaller than the traditional process zone size of Rice (1993) $h^*=\eta GL/\sigma(b-a)$, where η is a geometrical factor, and at least 1.3 times smaller than the revised theoretical size of the process zone (L_b), the small zone of frictional weakening in the vicinity of a slip front (Ampuero and Rubin, 2008; Perfettini and Ampuero, 2008):

$$L_b=\eta GL/\sigma b \quad (6)$$

2.2 Simulation results of postseismic slip propagation process

In order to guide our theoretical analysis, we carry a set of simulations varying some model parameters, as shown in Table 2, and examine the evolution of slip and stress. Frictional parameters in AS and SS for all of models in Table 2 are the same as the reference (Model A). All our models comprise only one asperity and produce events with perfectly periodic recurrence. The recurrence intervals and seismic moment magnitudes (listed in Table 2) are about 50 years and M_w 7, respectively, and depend on the frictional parameters of MS even if the frictional parameters of AS are fixed. The difference of simulation parameters between this study and Ariyoshi et al. (2007b) is that we modify Model I from $L'=L/20$ in Ariyoshi et al. (2007b) to $L'=L\times 2$ and that Δ_X in Ariyoshi et al. (2007b) for the outer part of MS is 2.5 km, to resolve better the length scale L_b and thus avoid the possibility of mesh size dependency. The simulation results and conclusions presented in the following sections do not depend significantly on Δ_X .

Table 2. Frictional properties and characteristics of interplate earthquake

Model	Friction parameters in MS	T_r (years)	M_w *1
A (ref.)	a=0.002, b=0.0019, L=4cm	49.5	7.3
B	σ'=467MPa (constant)	48.4	7.3
C	$\sigma'=\sigma/2$	55.0	7.5
D	b'=1.026b, $(a-b)'=(a-b)/2$	51.2	7.4

E	$a'=0.5a$, $b'=0.47b$, $(a-b)'=(a-b)$	56.3	7.6
F	$L'=L/2$	51.3	7.4
G	$\sigma'=\sigma/5$	62.1	7.6
H	$\sigma'=\sigma/10$	66.1	7.7
I	$L'=L\times 2$	48.6	7.3

Table 3. (See attached file).

A schematic description of the postseismic propagation process emerges from inspection of the temporal evolution of shear stress and slip. Figure 2a shows time-series of slip (dashed lines) and friction coefficient (solid lines) at several locations between (X, W)=(0, 110) and (0, 120) over a period spanning an earthquake and its postseismic slip. The postseismic slip propagates outward from AS. Figures 2b to 2g show snapshots of slip velocity at times indicated by arrows in Figure 2a. From these results, the propagation process of postseismic slip induces at a given point in MS six evolutionary stages, as shown schematically in Figure 2h:

- P-0, Preseismic period: shear stress remains constant and friction remains at steady state far from the mainshock, where stress changes due to preseismic slip are negligible.
- P-1, Coseismic period: shear stress increases suddenly due to coseismic slip.
- P-2, Approach period: shear stress gradually increases as the postseismic slip front approaches.
- P-3, Surge period: the postseismic slip front is now close and induces a faster increase of shear stress.
- P-4, Release period: the shear stress reaches its peak and drops to its minimum value while slip accelerates prominently.
- P-5, Deceleration period: slip slows down progressively and shear stress converges to the level of P-1.

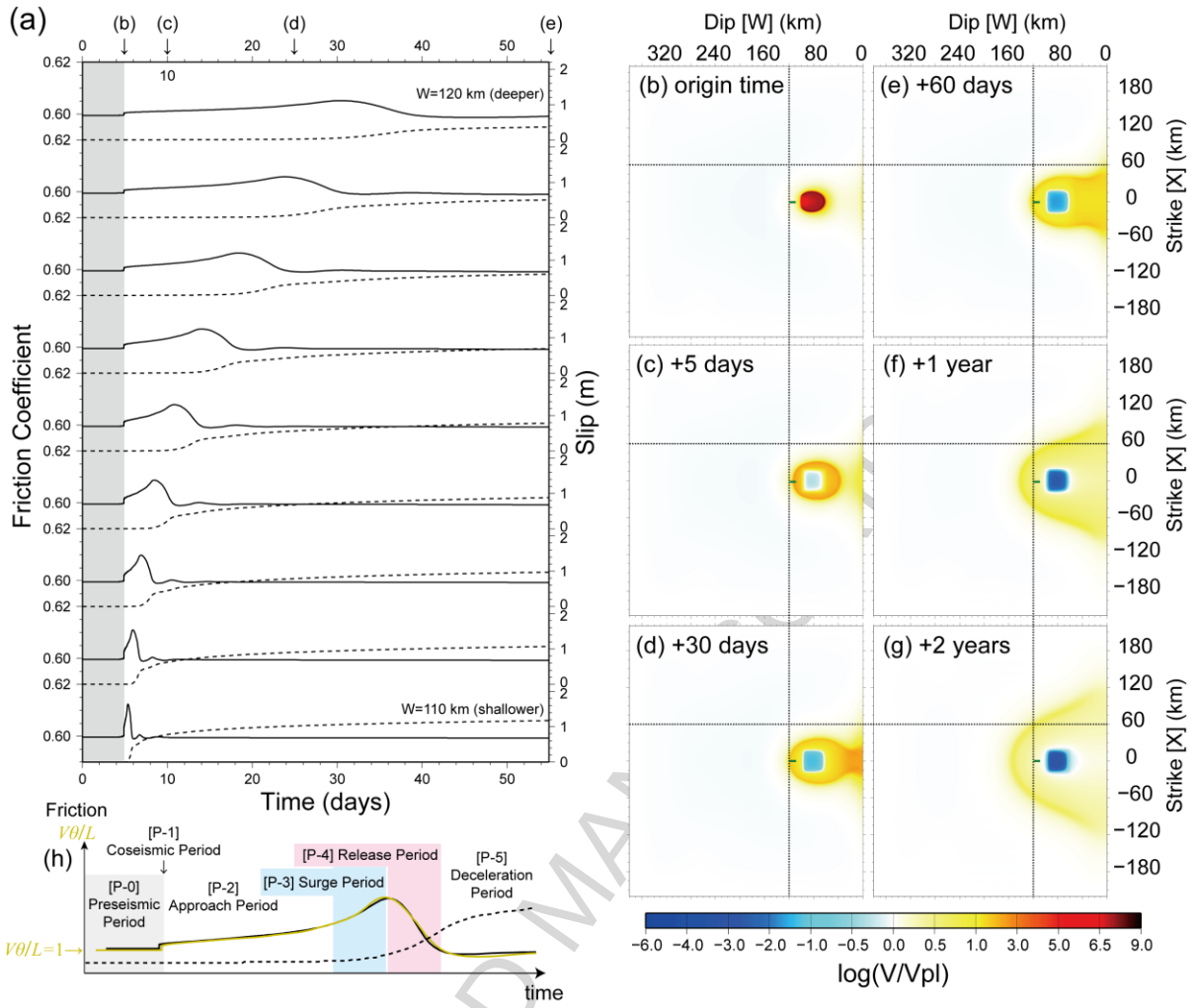

Figure 2. Postseismic slip in model A. This model produces characteristic Mw 7.3 events every 49.5 years. (a) Evolution of cumulative slip (dashed lines) and friction coefficient (solid lines) on the plate interface following a characteristic earthquake, at sub-faults situated every 1.25 km along the dip direction from W=110 (bottom) to W=120 km (top) at X=0 as shown by short green lines in (b-g). The gray band indicates the preseismic period. (b)-(g) Snapshots of slip velocity normalized by plate convergence rate (V_{pl}). Dotted lines along X=60 and W=120 are for reference, to help appreciate the propagation of postseismic slip. The time of snapshots (b) to (e) is indicated by arrows at the top of (a). (h) Evolutionary stages for one of the sub-faults. The dark yellow curve shows the evolution of $V\theta/L$. The postseismic slip propagation process comprises six periods: [P-0] Preseismic, [P-1] Coseismic, [P-2] Approach, [P-3] Surge, [P-4] Release, and [P-5] Deceleration.

Our simulations illustrate how the frictional parameters a and b affect postseismic propagation speed. We define the onset time of postseismic slip at a given point of the fault

as the time when shear stress reaches its maximum, which approximately corresponds to the onset time of postseismic slip acceleration at the transition between stages P-3 and P-4. We define the range of postseismic slip propagation as the region where maximum slip velocity V_{slip}^{max} is greater than $2V_{pl}$. Figure 3 shows the spatial distribution of postseismic slip onset time, relative to the earthquake origin time, for each of the models in Table 2. Comparison of Figures 3a and 3d shows that reducing by half the value of (a-b) causes little difference in the propagation speed (the interval between contours is similar) but increases the range of postseismic slip. Comparison between Figures 3a and 3e shows that the propagation speed depends on the values of a and b separately, even if (a-b) is held constant. Theoretical insight on these dependencies is developed in section 3. In the next section, we review the known relationship between propagation speed and maximum slip velocity.

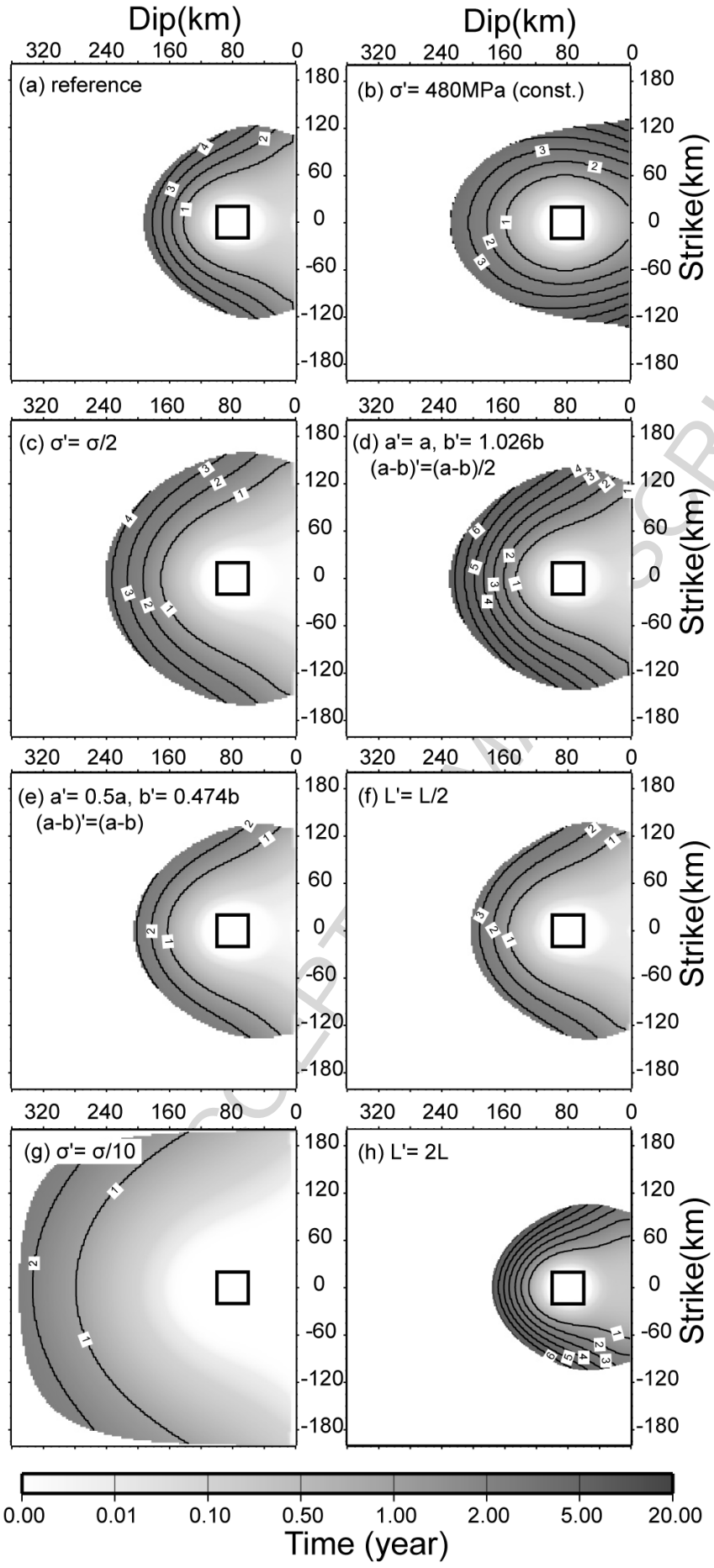

Figure 3. Onset times of postseismic slip (in years after the mainshock) for the eight models listed in Table 2. The square denotes the asperity (AS) region. Contours in the regions where the sliding velocities never exceed twice V_{pl} are not shown.

2.3 Relationship between propagation speed and maximum slip velocity

Following Perfettini and Ampuero (2008), we investigate the relationship between postseismic propagation speed (V_{prop}), maximum slip velocity ($V_{\text{slip}}^{\text{max}}$), shear stress drop in the Release period ($\Delta\tau$) and effective normal stress (σ). Shibazaki and Shimamoto (2007) applied a known theoretical relationship between rupture speed and peak slip velocity of dynamic ruptures (Ida, 1973; Ohnaka and Yamashita, 1989) to discuss properties of observed slow slip event propagation (e.g., Ozawa et al., 2002; Miyazaki et al., 2006). For very slow ruptures (much slower than seismic wave speeds), the relationship is

$$V_{slip}^{max} = \frac{\Delta\tau_b}{CG} V_{prop}. \quad (7)$$

where $\Delta\tau_b$ is the breakdown stress drop, defined as the difference between the peak and residual shear stresses near the propagating slip front, and C is a coefficient of order 1.

We calculate the postseismic propagation speed in our simulations, $V_{\text{prop}}^{\text{sim}}$, between the endpoints of each segment in Figure 1 as the ratio between their distance and the difference of their postseismic onset times. The values of these quantities along the 6 fault segments indicated in Figure 1 are reported in Table 3. Figure 4 shows a log-log plot of $V_{\text{prop}}^{\text{sim}}$ as a function of $(G/\Delta\tau)V_{\text{slip}}^{\text{max}}$, based on values from our simulations results, where $\Delta\tau$ is the stress drop in the Release period and $V_{\text{slip}}^{\text{max}}$ is evaluated at the midpoint of each segment. We find that $V_{\text{prop}}^{\text{sim}}$ is roughly proportional to $(G/\Delta\tau)V_{\text{slip}}^{\text{max}} / V_{\text{pl}}$., consistently with Eq. (7).

Ampuero and Rubin (2008) introduced a specific version of Eq. (7) in the context of rate-and-state friction models, noting that $\Delta\tau_b = b\sigma \ln\left(V_{slip}^{max}\theta_i/L\right)$ where θ_i is the value of the state variable before the arrival of the postseismic front. After validating this relationship on rate-and-state afterslip simulations, Perfettini and Ampuero (2008) discussed its implications for postseismic slip. Roland and McGuire (2009) rewrite Eq. (7) by using an approximation by Rubin (2008) as

$$V_{slip}^{max} = \frac{b\sigma}{G}\ln\left(V_{slip}^{max}\theta_i/L\right) V_{prop} \sim \frac{b\sigma}{5G} V_{prop}. \quad (8)$$

However, application of the relationships in Eqs. (7) and (8) to actual observations is limited because they only provide an estimate of V_{prop} if V_{slip}^{max} is known, but not a prediction of either V_{slip}^{max} or V_{prop} without direct observations. Obviously, a theory that would predict them based on rheological parameters would be more useful. In the next section, we describe

the postseismic slip propagation speed as a function of frictional and geometrical fault properties, instead of maximum slip velocity.

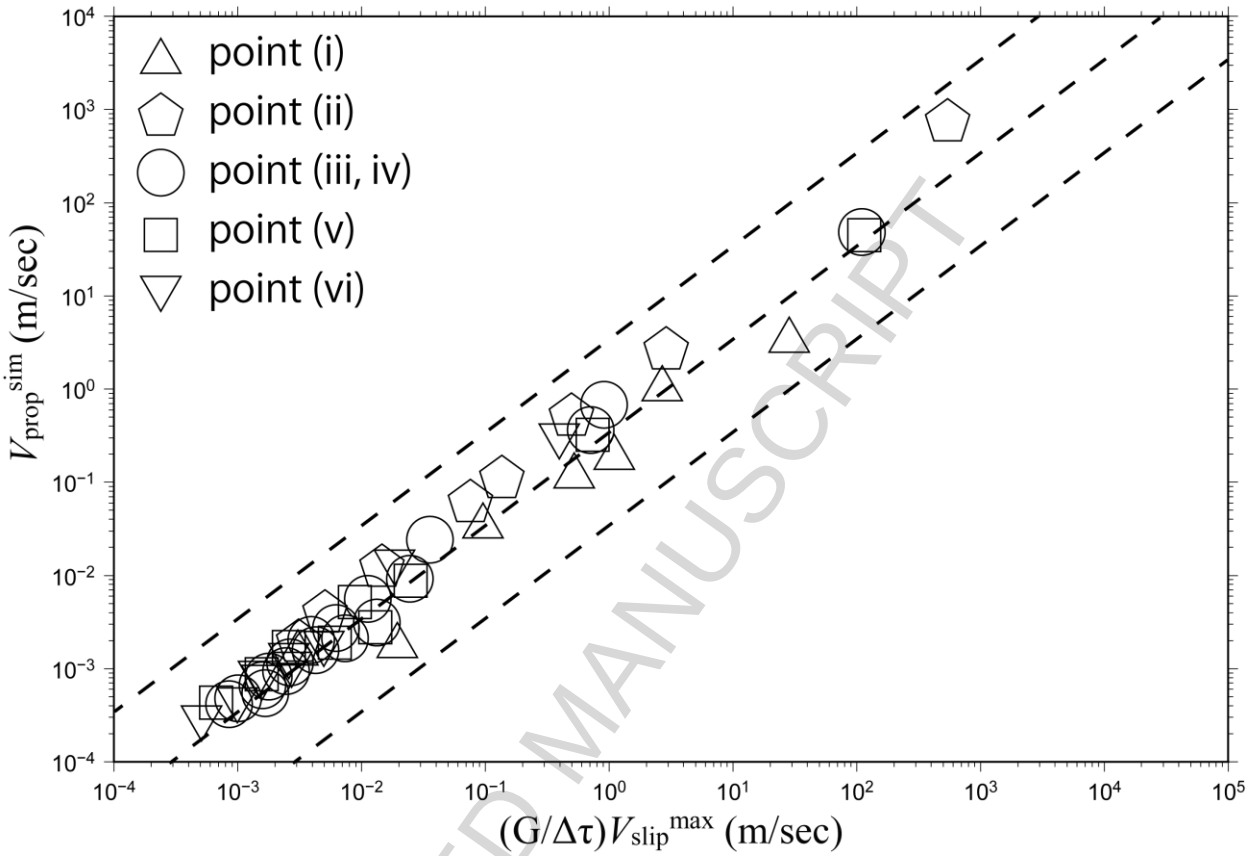

Figure 4. Relationship between the maximum slip velocity (V_{slip}^{max}) and the propagation speed of postseismic slip in the simulations (V_{prop}^{sim}) compared to Eq. (7) from all models listed in Table 2. Each symbol represents a segment in Figure 1. We calculate V_{prop}^{sim} between endpoints of each segment and V_{slip}^{max} at the midpoint of each segment. Dashed lines indicate agreement between theory and simulation results within one order of magnitude (1/10 to 10 times).

3 Theoretical Analysis

3.1 Conceptual postseismic slip propagation process

Figure 5 shows a schematic illustration of our concept. We define the Release Zone as the region where, at a given time, the coefficient is decaying from its peak to its residual value.

Figure 5a shows the spatial extent (Δs) of the Release Zone for the segments (i), (ii), (v) and (vi). What controls Δs is discussed later, in sections 5.2 and 5.3. The propagation path of postseismic slip from the earthquake source (AS) to a receiver point (in MS) is divided into segments equal to Δs. With this choice, the onset of the Release period of a point corresponds approximately to the onset of the Surge period of the point at a distance of Δs along the path, as shown in Figure 5b. Therefore, the arrival time T of postseismic slip at a given point corresponds to the sum of the Surge period durations ΔT_i along the propagation path, $T = \Sigma(\Delta T_i)$. In the next section, we develop approximate equations for the delay time ΔT_i as a function of frictional parameters, effective normal stress and shear stress change due to postseismic slip.

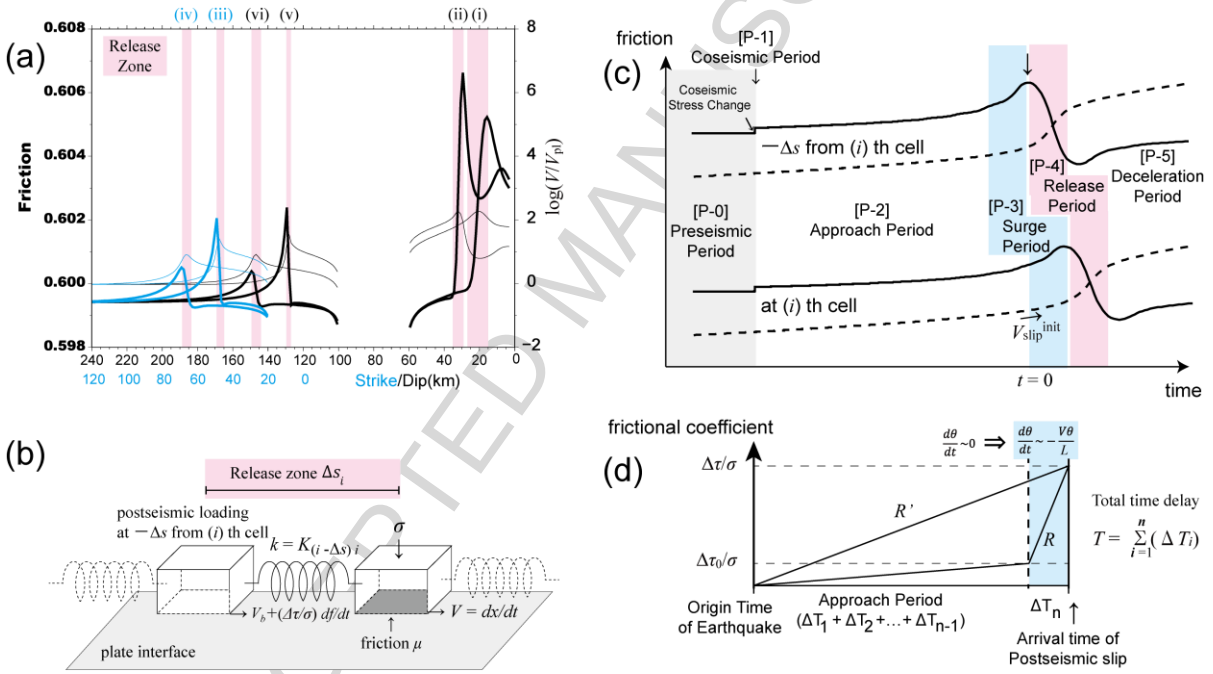

Figure 5. (a) Spatial extent of the Release Zone (pink bands) determined by the along-strike distributions of friction coefficient for segments (i), (ii), (v) and (vi) (cyan color) and along-dip (black color) for the segments (iii) and (iv) (solid curves), at times T=0.064, 0.03, 0.34, 1.4, 0.43, and 1.3 years from the origin time of the earthquake, respectively. The distribution of the logarithm of slip velocity normalized by V_{pl} is shown by thin curves. (b) Spring-slider system representation of the postseismic slip propagation process. (c) Comparison of slip (dashed curve) and friction coefficient (solid curve) between two points in the postseismic slip area separated by a distance equal to the Release Zone size Δs_i. (d) Two approximations of the shear stress loading at a point induced by slip on another point at

distance Δs_i: as ramp (two linear segments) and as linear functions of time after the earthquake occurrence.

3.2 Analytical derivation of delay time and propagation speed

Gomberg et al. (1998) solved the equations of the RSF law introduced by Dieterich (1994) to obtain approximate analytical equations for the evolution of pre- and coseismic slip. Here we review their analytical derivation, and extend it to postseismic slip to determine the delay time (ΔT_i).

We make use of an analogy between the continuum numerical simulation and a massless multi-spring-slider system as shown in Figure 5d. A slider corresponds to a discrete segment of MS with size Δs (the local Release Zone size). The stiffness k corresponds to the static stress transfer coefficient between the Release Zone and a neighboring point at a distance Δs : $k = \eta G/\Delta s$. The shear stress of the massless spring-slider system subject to the loading shown in Figure 5d is

$$\tau = k\,(V_b\,t - x(t)) + \Delta\tau\, f(t) = \mu(t)\,\sigma, \qquad (9)$$

where $x(t)$ is the slider displacement, $\Delta\tau$ is the amplitude of the shear loading due to the approaching postseismic slip, $f(t)$ is the normalized loading history, and V_b is the background slip velocity at the loading point (equal to V_{pl} if there are no stress perturbations). We neglect the stress interactions beyond distance Δs (beyond the neighboring Release Zone) because we focus on the Surge period at the point of interest. Interactions with more distant points become important later, during the Deceleration period.

The sliding velocity $V(t) = dx(t)/dt$ is obtained from Eq. (4) as

$$V(t) = V_0 \exp(\{\mu(t) - \mu_0 - b\ln(V_0\theta/L)\} / a)\,. \qquad (10)$$

Substituting Eq. (9) into Eq. (10), we get

$$V(t) = V_0 \exp(\{(kV_b/\sigma)\,t + (\Delta\tau/\sigma)\,f(t) - k\,x(t)/\sigma - \mu_0 - b\ln(V_0\theta/L)\} / a)\,. \qquad (11)$$

As shown in the Surge period of Figure 5c, the shear stress suddenly increases whereas the sliding velocity remains low. According to Eq. (5), the state variable θ increases rapidly. The evolution of $V\theta/L$ (Figure 6) is similar to that of the friction coefficient (Figure 2h). Its value is approximately 1 in the Preseismic, Approach and Deceleration periods, and becomes much larger than 1 between the Surge and Release periods. Therefore, V and θ in the Surge period satisfy

$$V\theta/L >> 1 \qquad (12)$$

i.e. the slider is well above steady state. This condition is discussed in section 5.1. Under this condition, Eq. (5) can be approximated as

$$d\theta(t) / dt \approx - V\theta/L \, . \tag{13}$$

Integrating Eq. (13) in time, we obtain

$$\theta(t) \approx \theta_{\text{init}} \exp\{- x(t)/L\}. \tag{14}$$

Here, we set the origin time (t=0) between the Approach and Surge periods, and the initial conditions $\theta_{\text{init}} = \theta(0)$ and $x(0)$=0. Thus the state variable θ decreases monotonically as slip accumulates in the Surge period. In the Release period, the slip velocity increases and θ decreases, which eventually violates the condition of Eq. (12). Therefore, the approximation in Eq. (13) is only valid between the Surge and Release periods, as shown in Figure 6. Substituting Eq. (14) into Eq. (11)

$$V(t) = \mathrm{d}x/\mathrm{d}t = V_{\text{fact}} \exp(\{(kV_b/\sigma)\, t + (\Delta\tau/\sigma)\, f(t) + x(t)\gamma\} / a) \, , \tag{15}$$

where

$$\gamma = b/L - k/\sigma \, . \tag{16}$$

$$V_{\text{fact}} = V_0 \exp(\{\mu_{\text{init}} - \mu_0 - b\ln(V_0\, \theta_{\text{init}}/L)\} / a) \, . \tag{17}$$

The value of γ depends on the ratio $\Delta s/L_b = b\sigma/kL$ and is positive (γ >0), as listed in Table 3.

Here, we consider the initial condition at the onset of the Surge period (V_{slip}^{init} as shown in Figure 5c). From Figure 6, the value of $V\theta/L$ at the initiation of the Surge period on the deeper part is nearly 1, thus $\mathrm{d}\theta/\mathrm{d}t \sim 0$. In the shallower part, $\mathrm{d}\theta/\mathrm{d}t$ has a small negative value (-1 at most), thus the evolution (last) term of Eq. (4) decreases as $b\log(V_0\{\theta_{\text{init}} - t\}/L)$. Since $\Delta T_i << L/V_0$ in the shallower part in Figure 6, the value of $b\log(V_0\{\theta_{\text{init}} - \Delta T_i\}/L)$ can be approximated as $b\log(V_0\theta_{\text{init}}/L)$, thus we can also consider $\mathrm{d}\theta/\mathrm{d}t \sim 0$ for the shallower part. This gives

$$\theta_{init} = L/V_{slip}^{init}, \tag{18}$$

$$\mu_{init} = \mu_0 + (a - b)\log\left(V_{slip}^{init}/V_0\right). \tag{19}$$

Substituting Eq. (19) into Eq. (17),

$$V_{fact} = V_{slip}^{init}. \tag{20}.$$

Integrating Eq. (15), we obtain

$$\int_0^x \exp\left\{-\gamma x'/a\right\} dx' = V_{slip}^{init} \int_0^t \exp\left\{\frac{kV_b t' + \Delta\tau \cdot f(t')}{a\sigma}\right\} dt', \tag{21}$$

where the integrals span the Surge Period of the sub-fault. Where postseismic slip reaches peak slip velocities much higher than V_{slip}^{init}, we can adopt an approximation similar to that made by Gomberg et al. (1998) and define the onset time of postseismic slip as the time when

the slip predicted by Eq. (21) (and thus the slip velocity) becomes infinite. The left-hand side can be integrated as $\frac{a}{\gamma}\left\{1-\exp\left(-\frac{\gamma}{a}x\right)\right\}$, which for infinite x becomes $\frac{a}{\gamma}$. The delay time (ΔT_i) can thus be determined by solving the following condition:

$$\frac{a}{\gamma} = V_{slip}^{init}\int_0^{\Delta T_i}\exp\left\{\frac{kV_b t' + \Delta\tau\cdot f(t')}{a\sigma}\right\}dt' \qquad (22)$$

To make further progress, we consider three approximate loading time functions $f(t)$: (i) ramp function, (ii) linear function, and (iii) step function.

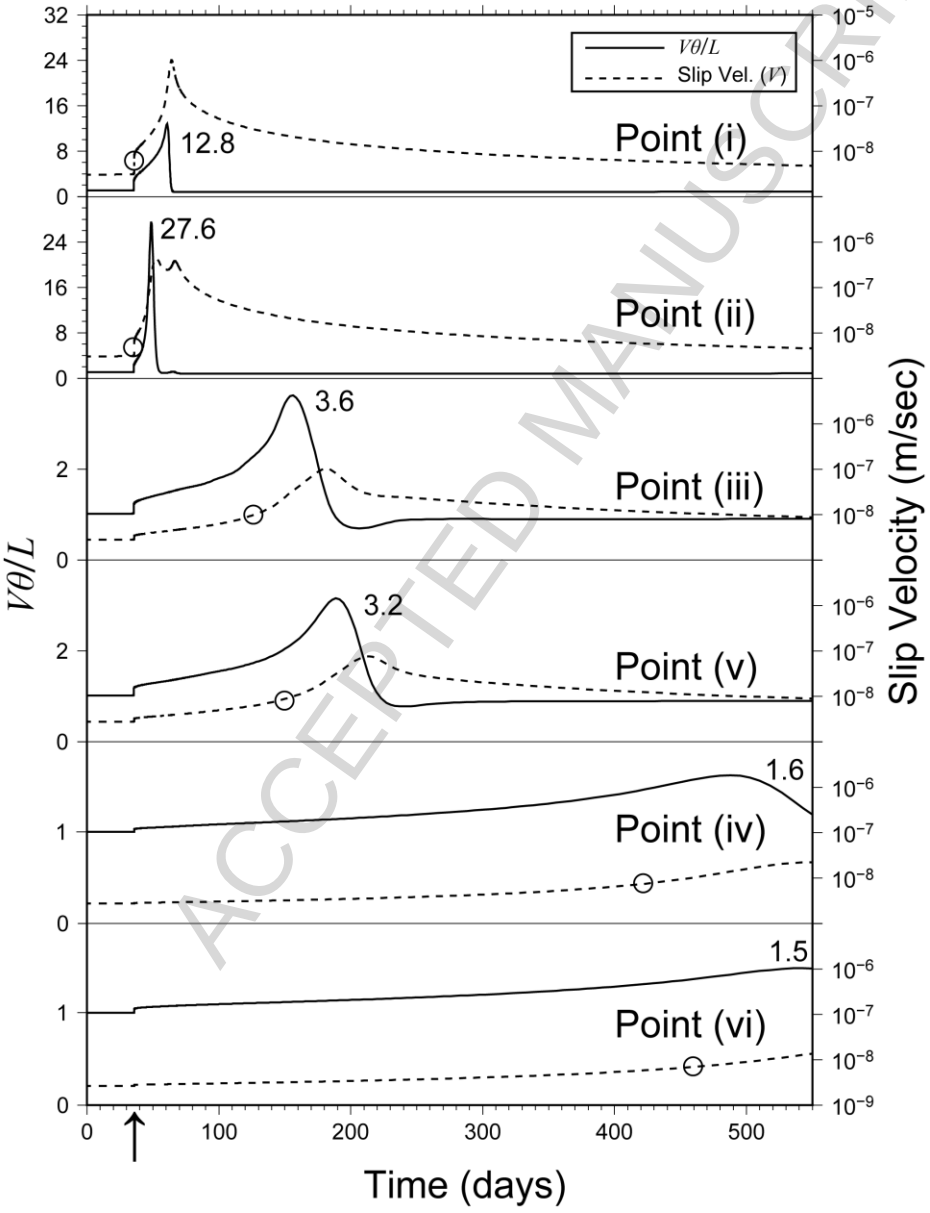

Figure 6. The time history of slip velocities (dashed lines) and $V\theta/L$ (solid lines) at the midpoints of the segments (i) to (vi) in model A. The vertical arrow on the bottom indicates the onset time of the event. Circles represent the possible value of V_{slip}^{init}. Note that the vertical scale of $V\theta/L$ is different among the points.

3.2.1 Ramp function

From Figure 5d, we approximate $f(t)$ as a ramp function determined by its amplitude ($\Delta\tau$) and its rate (R). We define $\Delta\tau$ and $\Delta\tau_0$ as the stress increase due to postseismic slip during the Approach and Surge periods and during only the Approach period, respectively. R and R' are the average rates of change of friction coefficient during the Surge period and during the Approach and Surge periods, respectively. For simplicity, we adopt the following approximations:

$$\Delta\tau \gg \Delta\tau_0 \text{ (or } (\Delta\tau - \Delta\tau_0) \sim \Delta\tau) \tag{23}$$

$$R = \alpha R' \quad (\alpha > 1) \tag{24}$$

In this case, $f(t)$ is expressed as

$$f(t) = t\,\sigma R/\Delta\tau \quad \text{if } 0 \le t \le \Delta\tau/\sigma R, \tag{25}$$

$$f(t) = 1 \quad \text{if } t \ge \Delta\tau/\sigma R.$$

Plugging Eq. (25) into Eq. (22) and integrating we obtain

$$\Delta T_i^{ramp} = \frac{a\sigma}{kV_b} \log\left(F_{ramp} + \frac{kV_b}{\gamma\sigma V_{slip}^{init}}\right) - \frac{\Delta\tau}{kV_b} \tag{26}$$

where

$$F_{ramp} = \frac{\sigma R}{kV_b + \sigma R}\left[\exp\left\{\frac{\Delta\tau(1 + kV_b/\sigma R)}{a\sigma}\right\} + \frac{kV_b}{\sigma R}\right]. \tag{27}$$

The propagation speed V_{prop} is

$$V_{prop}^{ramp}(a, b, L, \sigma, k, \Delta\tau, R \mid i) = \Delta s_i / \Delta T_i^{ramp}. \tag{28}$$

In Eq. (26), ΔT_i^{ramp} is inversely proportional to k, thus it is proportional to Δs_i. The latter cancels out from Eq. (28) and we get:

$$V_{prop}^{ramp} = \frac{\eta G V_b}{a\sigma \log\left(F_{ramp} + \frac{kV_b}{\gamma\sigma V_{slip}^{init}}\right) - \Delta\tau}. \tag{29}$$

3.2.2 Linear function

When we know only the rate of long-term shear stress loading (R), such as the loading induced by secular deformation, $f(t)$ can be assumed as a linear function:

$$f(t) = t\,\sigma R/\Delta\tau \tag{30}$$

Substituting Eq. (30) into Eq. (22), we get

$$\Delta T_i^{linear} = \frac{a\sigma}{kV_b + R\sigma} \log\left(1 + \frac{kV_b + R\sigma}{\gamma\sigma V_{slip}^{init}}\right) \tag{31}$$

$$V_{prop}^{linear}(a,b,L,\sigma,k,R \mid i) = \frac{\eta G V_b\,(1+R\sigma/kV_b)}{a\sigma \log\left(1+\frac{kV_b+R\sigma}{\gamma\sigma V_{slip}^{init}}\right)} \quad (32)$$

3.2.3 Step function

When we know only the amplitude of the shear stress loading ($\Delta\tau$) or the Surge period is expected to be short enough, $f(t)$ can be simply assumed as a step function from coseismic loading or other sudden event. In this case, we find

$$\Delta T_i^{step} = \frac{a\sigma}{kV_b} \log\left(1+\frac{kV_b}{\gamma\sigma V_{slip}^{init} F_{step}}\right) \quad (33)$$

$$V_{prop}^{step}(a,b,L,\sigma,k,\Delta\tau \mid i) = \frac{\eta G V_b}{a\sigma \log\left(1+\frac{kV_b}{\gamma\sigma V_{slip}^{init} F_{step}}\right)} \quad (34)$$

where

$$F_{step} = \exp\left(\frac{\Delta\tau}{a\sigma}\right). \quad (35)$$

3.3 Comparison of propagation speeds between the simulated results and the analytical solutions

To evaluate the validity of the approximations in Eqs. (29, 32, 34), we compare the predicted propagation speeds with the simulation results. We take the total delay time T and amplitude of shear stress loading $\Delta\tau$ from the simulation time histories (as shown in Figure 2a) to calculate the rate of frictional coefficient due to shear stress loading $R = \Delta\tau/\sigma T$. By applying the values of frictional parameters in MS (Table 2), we calculate the propagation speeds $V_{\mathrm{prop}}^{\mathrm{ramp}}$, $V_{\mathrm{prop}}^{\mathrm{linear}}$ and $V_{\mathrm{prop}}^{\mathrm{step}}$ from Eqs. (29), (32) and (34), respectively. Because it is difficult to estimate the value of α in advance, we compare two end member cases: a ramp function with $\alpha = 1$ ($R = R'$) and the case $\alpha = \infty$ equivalent to a step function, both with the same load amplitude $\Delta\tau$. In addition, we consider a linear increase case with $\alpha = 1$ by applying R to Eq. (32) because it is also difficult to know in advance the duration time of the Approach and Surge periods.

Figure 7 shows the ratio of the three analytical estimates of propagation speed to the numerically simulated one as a function of the maximum slip velocity ($V_{\mathrm{slip}}^{\mathrm{max}}$) normalized by the secular slip rate imposed by plate convergence. The analytical expressions agree with the

simulated propagation speed within one order of magnitude (1/10 to 10 times difference, as indicated by the gray band in Figure 7) for a wide range of slip velocities (spanning seven orders of magnitude) and for propagation along both strike and dip directions. This result shows that our theoretical relationships are generally useful to estimate V_{prop} from the frictional properties if we can estimate the values of $\Delta\tau$ and R in advance. For the shallow up-dip segment (i), however, the three estimates underestimate the propagation speed by up to several orders of magnitude, which will be discussed in section 5.1.

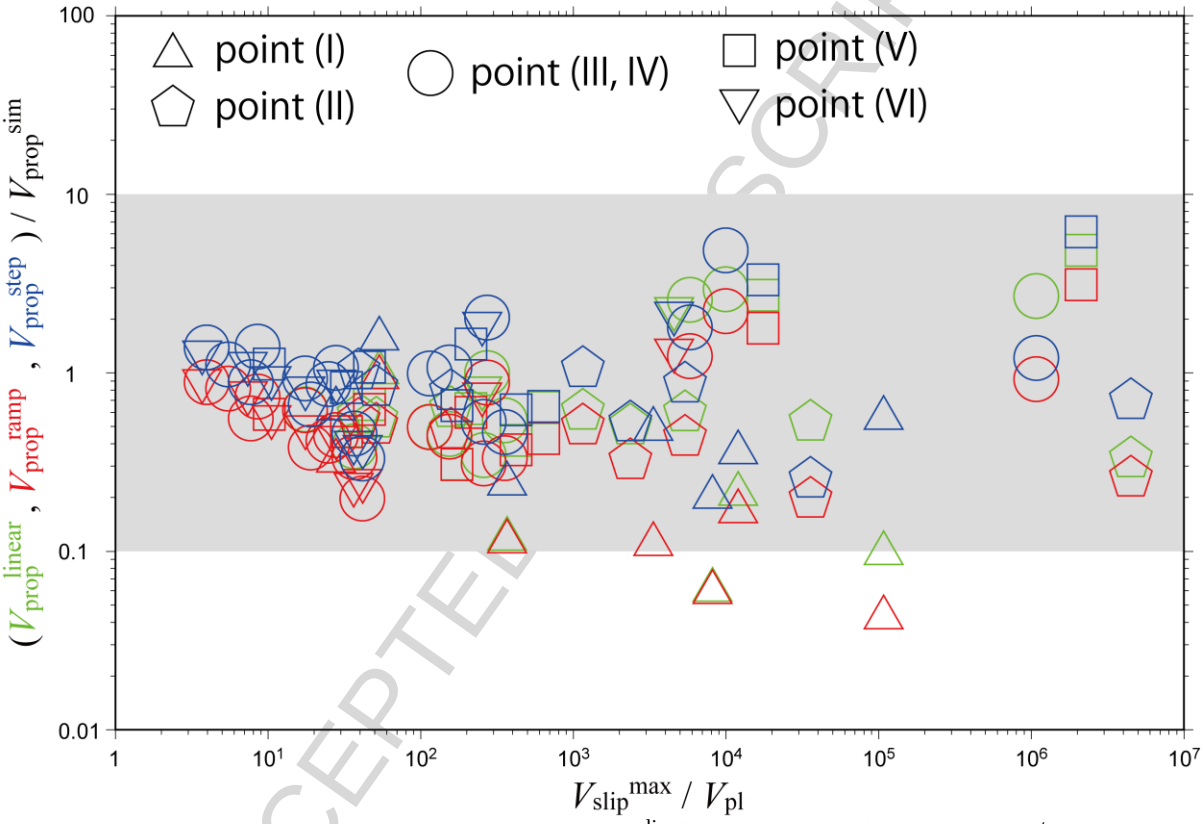

Figure 7. Comparison between the analyzed (V_{prop}^{linear}: green, V_{prop}^{ramp}: red, V_{prop}^{step}: blue) and the simulated (V_{prop}^{sim}) postseismic slip propagation speed, as a function of maximum slip velocity (V_{slip}^{max}) normalized by plate convergence rate (V_{pl}). Gray colored background represents the range in which the analyzed propagation speed is within one order of magnitude of the simulation results.

We find that the estimate V_{prop}^{ramp} tends to be smaller than both V_{prop}^{step} and V_{prop}^{linear} (Table 3). This difference arises because the amplitude of shear stress loading $\Delta\tau$ in the linear function case depends on ΔT_i^{linear} by $\Delta\tau^{linear} = R\sigma\Delta T_i^{linear}$, while for the ramp and step

functions it has a given constant value. When $\Delta T_i^{ramp} > \Delta\tau/\sigma R$, $f(t)^{ramp} < f(t)^{linear}$ from the definition of Eqs. (25) and (30), which means $\Delta\tau^{\text{linear}} > \Delta\tau^{\text{ramp}}$ for the same rate R in the linear and ramp functions. For a same $\Delta\tau$ in the step and ramp functions, the relation $V_{\text{prop}}{}^{\text{ramp}} < V_{\text{prop}}{}^{\text{step}}$ is robust because $F_{ramp} > F_{step}$ from mathematical comparison between Eqs. (27) and (35). An instantaneous increase of shear stress loading leads to faster propagation speed than a gradual one.

From these results, we confirm the general relationship between postseismic slip propagation speed and frictional properties, at least far from the free surface. In the next section, we adopt step and ramp functions to derive relations that do not depend on the amplitude of shear stress loading ($\Delta\tau$).

4 Relationship between postseismic slip propagation speed, frictional properties and initial slip velocity

4.1 Dependence on initial slip velocity and background loading velocity

We first evaluate the effect of the initial slip velocity of the Surge period (V_{slip}^{init} as shown in Figure 5c) on the postseismic slip propagation speed. Figure 8 shows the analytical estimates $V_{\text{prop}}{}^{\text{ramp}}$ and $V_{\text{prop}}{}^{\text{step}}$ for segments (ii) and (iii) as a function of V_{slip}^{init} for different values of $\Delta\tau$ (0.1 to 10.1 MPa). The input parameters that are different among all the segments are k, $\Delta\tau$, Δs and T as listed in Table 3 (T is used only for the ramp function). For simplicity, we assume that the value of Δs is fixed, which is discussed in section of 5.2.

Figures 8a and 8b show a linear relationship between V_{prop}^{step} and V_{slip}^{init}, which is consistent with the following approximation to Eq. (34):

$$V_{prop}^{step} \approx \frac{\eta\gamma G}{ak}\exp\left(\frac{\Delta\tau}{a\sigma}\right)V_{slip}^{init} \quad \text{if} \quad \frac{kV_b}{\gamma\sigma V_{slip}^{init}F_{step}} = \frac{V_b/V_{slip}^{init}}{\left(\frac{b\sigma}{kL}-1\right)\exp\left(\frac{\Delta\tau}{a\sigma}\right)} \ll 1. \qquad (36)$$

From Table 3, the value of $\frac{k}{\gamma\sigma F_{step}}$ is sufficiently smaller than 1. Thus the approximation of Eq. (36) is robustly applicable for $V_{slip}^{init} \geq V_b \sim V_{pl}$ in Figures 8ab. Figures 8ab and Eq. (36) show that the ratio $V_{prop}^{step}/V_{slip}^{init}$ depends strongly on $\Delta\tau$.

Figures 8c and 8d show that the estimate V_{prop}^{ramp} is asymptotically proportional to V_{slip}^{init} for large values of V_{slip}^{init}. This arises because $f(t)$ becomes a linear function when

$\Delta s_i / V_{prop}^{ramp} = \Delta T_i^{ramp} < \Delta\tau/\sigma R$. Then if $\frac{kV_b + R\sigma}{\gamma\sigma V_{slip}^{init}} = \frac{V_b + R\sigma/k}{\left(\frac{b\sigma}{kL} - 1\right) V_{slip}^{init}} \ll 1$, Eq. (32) can be approximated as

$$V_{prop}^{linear} \approx \frac{\eta\gamma G}{ak} V_{slip}^{init} \qquad (37)$$

The condition $\frac{kV_b + R\sigma}{\gamma\sigma V_{slip}^{init}} < 0.1$ for segments (ii) and (iii) corresponds to $V_{slip}^{init} > 1.6\times10^{-7}$ m/sec (= 56 V_{pl}) and $V_{slip}^{init} > 4.0\times10^{-9}$ m/sec (= 1.4 V_{pl}), respectively. Under that condition, the ratio $V_{prop}^{linear}/V_{slip}^{init}$ is asymptotically independent of $\Delta\tau$ as shown by Eq. (37).

The background loading velocity V_b and the additional shear loading rate R for the linear function do not influence these estimates of V_{prop} if V_{slip}^{init} is much larger than V_b or independent of V_b and R.

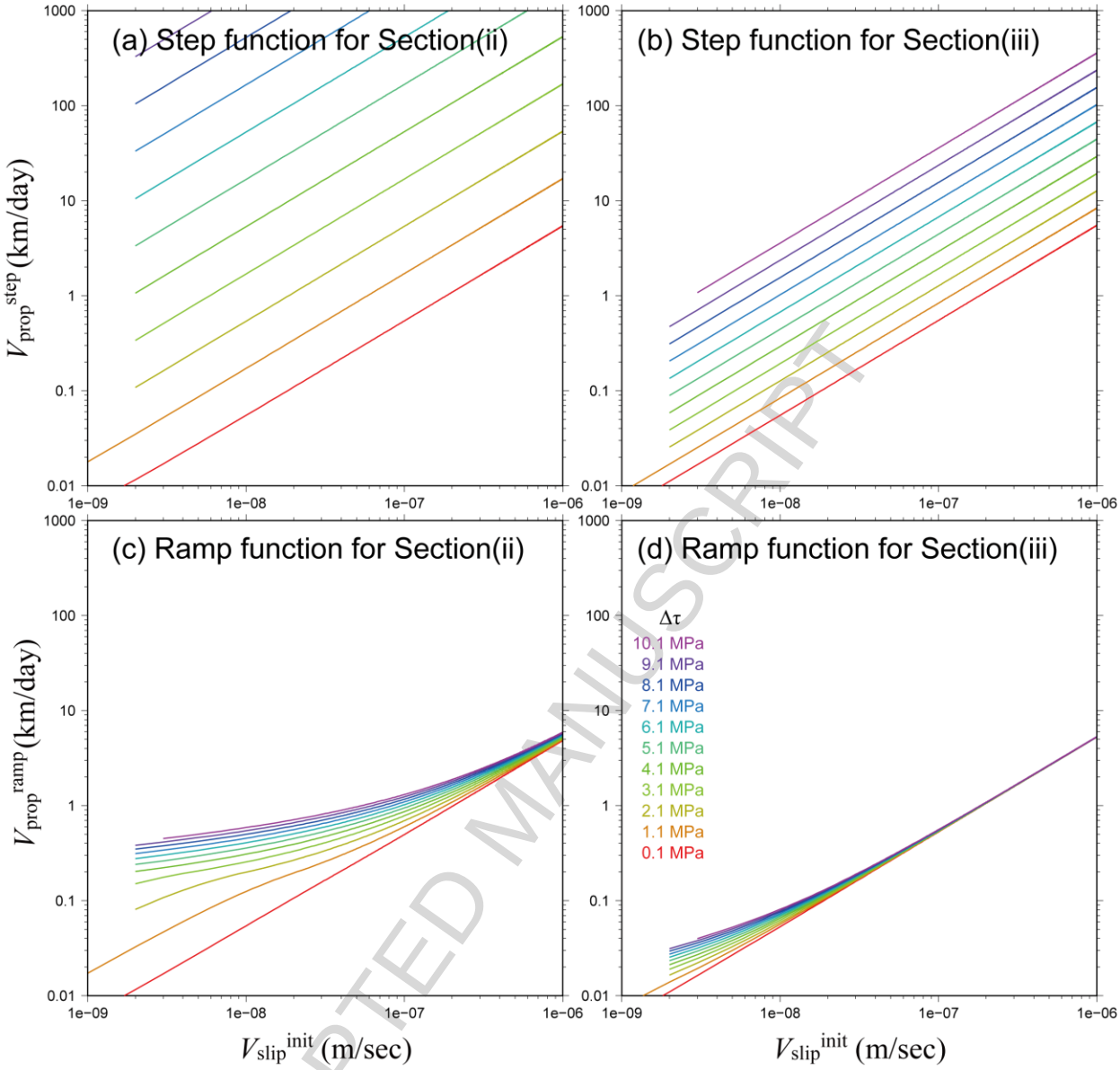

Figure 8. Theoretical relationship between the propagation speed of postseismic slip and initial slip velocity under the steady state condition (V_{slip}^{init}) for two approximations of the shear stress loading, (a, b) a step function V_{prop}^{step} and (c, d) ramp function V_{prop}^{ramp}, for (a, c) segment (ii) and (b, d) segment (iii). Colors indicate the amplitude of the shear stress loading (see legend in (d)).

4.2 Dependence on effective normal stress

Figure 9 shows V_{prop}^{ramp} and V_{prop}^{step} for segments (ii) and (iii) as a function of effective normal stress. To understand the role of the stiffness k, we focus on V_{prop}^{step} because step function is independent of $R = \alpha R' = \Delta\tau/T$, where T is different between Segments and

Models as shown in Table 3. In Figures 9a and 9b, where the only difference is the stiffness k due to the different crack mode II or III, the colored curves have similar shapes. In the upper horizontal axis of Figure 9, we converted normal stress to depth assuming hydrostatic fluid pressure by applying Eq. (3) and approximately treating the dependence of k on depth as negligible except for segment (i) as suggested in Table 3. This allows to readily grasp the depth dependence of V_{prop}.

In Figure 9, because we adopt the fixed value of Δs=5.0 and 3.75 km for segments (ii) and (iii) of Model A for simplicity, the value of γ becomes negative when

$$\sigma < kL/b = \eta GL/(b\Delta s) \quad (38).$$

Considering the values of k, L and b of Model A, the critical σ for segments (ii) and (iii) from Table 3 are 118 and 27.4 MPa, respectively. The range of effective normal stresses lower than the critical value are indicated in Figure 9 by a gray band. The condition of slip propagation with γ<0 is discussed in section 5.4.

As introduced in the case of the ramp function for Eq. (25), there is a transition from ramp to linear function when V_{prop}^{ramp} becomes higher such that $\Delta s_i/V_{prop}^{ramp} = \Delta T_i^{ramp} < \Delta\tau/\sigma R$. In Figure 9c, there are kinks aligned along the horizontal dotted line, while in Figure 9d the kink appears at a low value V_{prop}^{ramp} ≈0.0154 km/day. Figure 9 shows that there is little dependency of V_{prop}^{ramp} on $\Delta\tau$ if $\Delta\tau$ < 0.1 MPa; V_{prop}^{ramp} is then almost constant at 0.0147 km/day. These results are valid for both step and ramp functions.

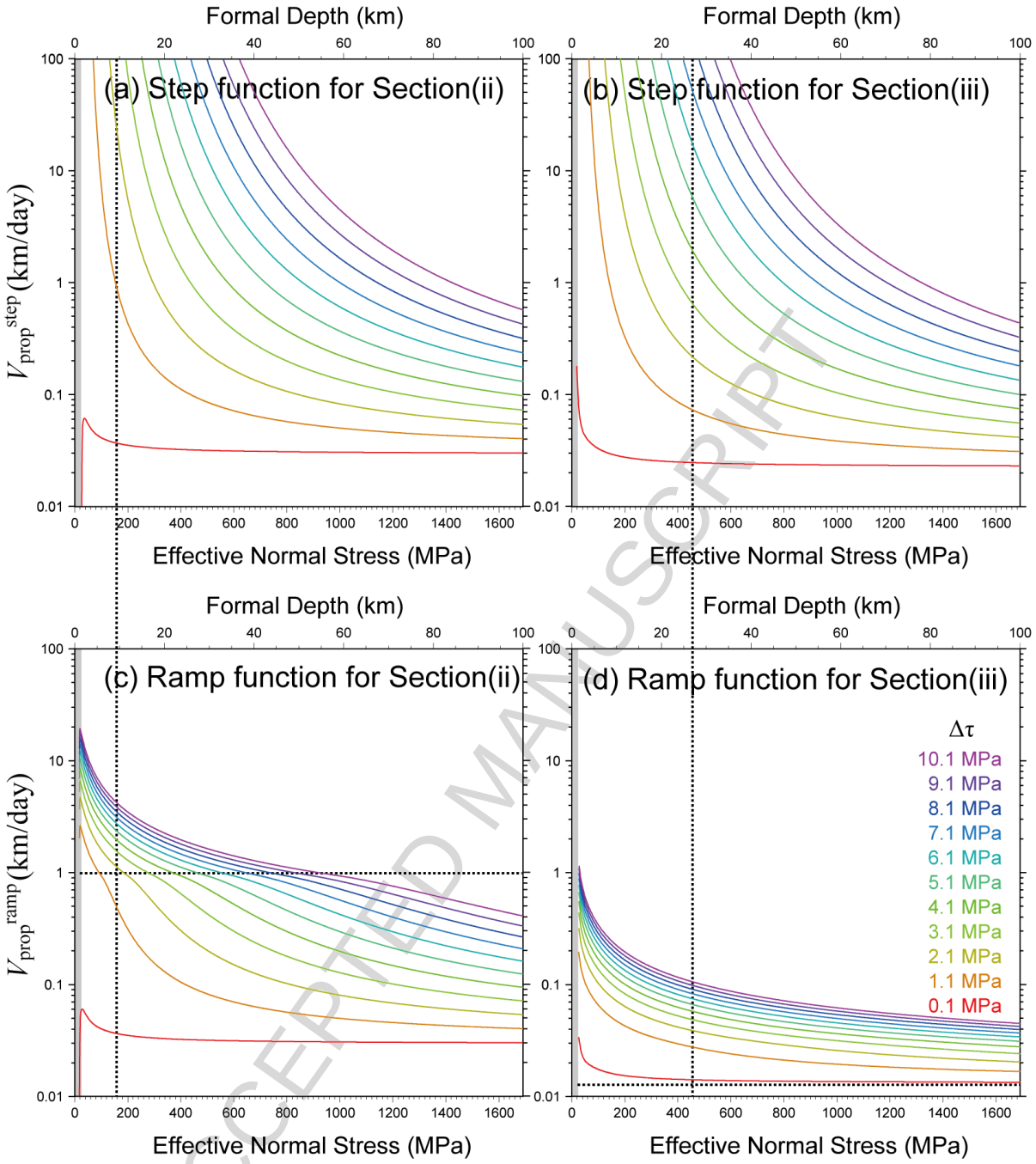

Figure 9. Theoretical relationship between the propagation speed of postseismic slip and effective normal stress (or depth converted from Eq. (3)) for two approximations of the shear stress loading, (a, b) step function V_{prop}^{step} and (c, d) ramp function V_{prop}^{ramp}, for (a, c) segment (ii) and (b, d) segment (iii). Colors indicate the amplitude of the shear stress loading. Vertical dotted lines represent the depth corresponding to the Points (ii) and (iii). Horizontal dotted lines in (c, d) indicate the transition from ramp to linear function when $\Delta T_i^{ramp} < \Delta\tau/\sigma R$. Gray colored background represents the unsolved region because of $\gamma < 0$.

4.3 Dependence on the frictional parameters *a* and *b*

Figure 10 shows $V_{\text{prop}}^{\text{ramp}}$ and $V_{\text{prop}}^{\text{step}}$ for segments (ii) and (iii) as a function of the frictional parameter *a*. From Figures 10a and 10b, the dependence of $V_{\text{prop}}^{\text{step}}$ on *a* is similar to its dependence on the effective normal stress, in that a lower value of *a* leads to an exponentially higher propagation speed.

Figures 10c and 10d show that the relationship between V_{prop}^{ramp} and *a* seems approximately similar to V_{prop}^{step} before the transition from linear to ramp function, and becomes a linear relation after the transition. This linear relationship for smaller values of *a* is explained directly from Eq. (32). In Figures 10c and 10d, some curves are cut at the lowest *a* values because ΔT_i^{ramp} approaches zero, which means postseismic slip occurs immediately after the initiation of shear stress loading.

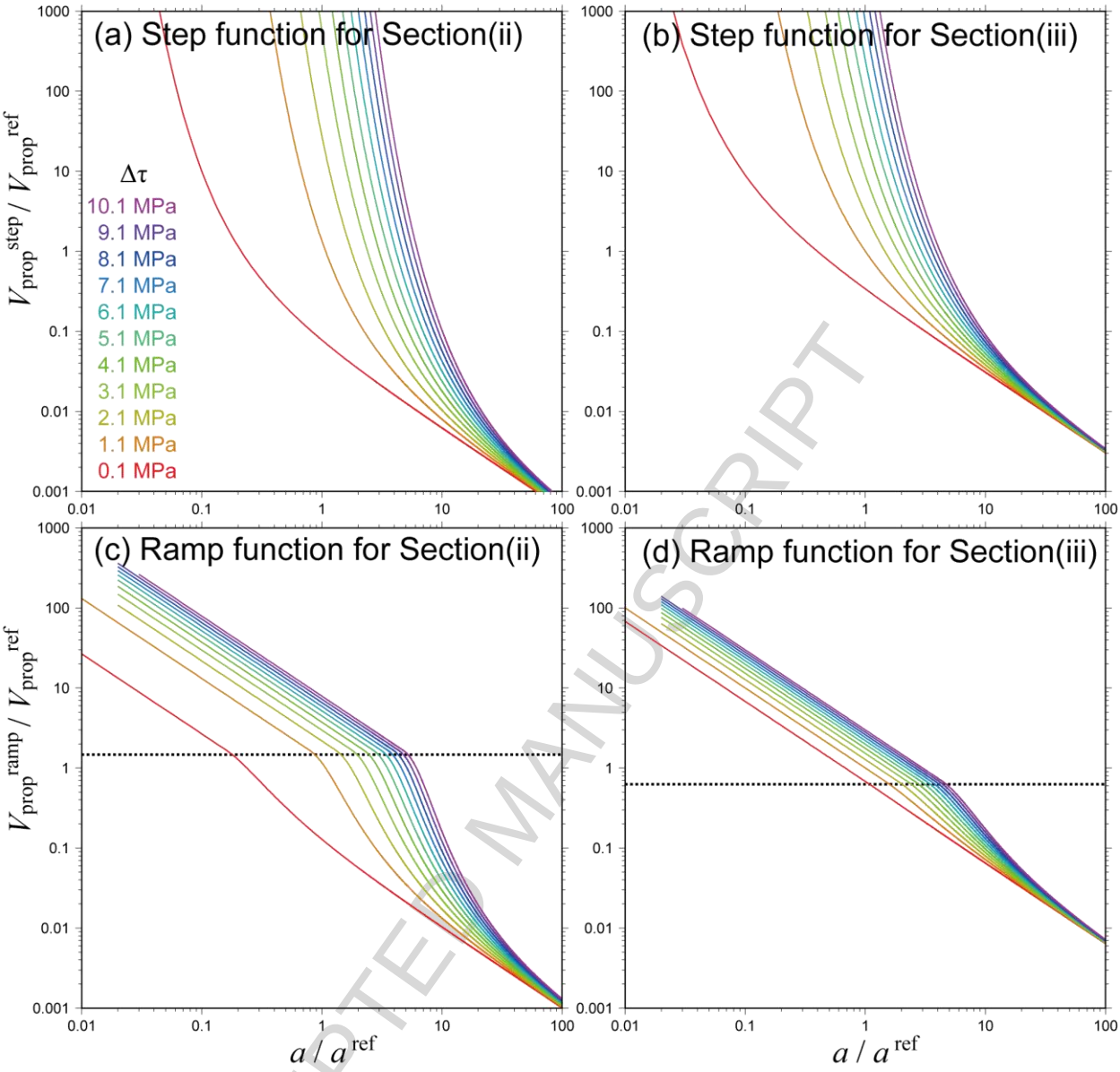

Figure 10. Theoretical relationship between the propagation speed of postseismic slip and frictional parameter "a" for two approximations of the shear stress loading, (a, b) step function V_{prop}^{step} and (c, d) ramp function V_{prop}^{ramp}, for (a, c) segment (ii) and (b, d) segment (iii). Colors indicate the amplitude of the shear stress loading. Dotted lines represent the transition from linear to ramp function.

Figure 11 shows the same as Figure 10 but as a function of the frictional parameter b. Figures 11a and 11b show a linear relationship between V_{prop}^{step} and b, which can be explained by an approximation similar to that leading to Eq. (36):

$$V_{prop}^{step} \approx \frac{\eta G V_b}{a\sigma \log\left(\frac{kV_b}{\gamma\sigma V_{slip}^{init}}\right) - \Delta\tau} \quad \text{if} \quad \frac{kV_b}{\gamma\sigma V_{slip}^{init} F_{step}} \gg 1. \tag{39}$$

From Eq. (16) and $b\sigma/kL$ >>1 for most of results from Table 3, when b is large enough to approximately satisfy

$$\gamma \approx b/L\ , \tag{40}$$

a linear relationship emerges between V_{prop}^{step} and b. Otherwise, Eq. (39) suggests a non-linear relationship.

In the ramp function case, Figures 11c and 11d are similar to Figures 8c and 8d. This is explained from Eq. (37) by applying Eq. (40).

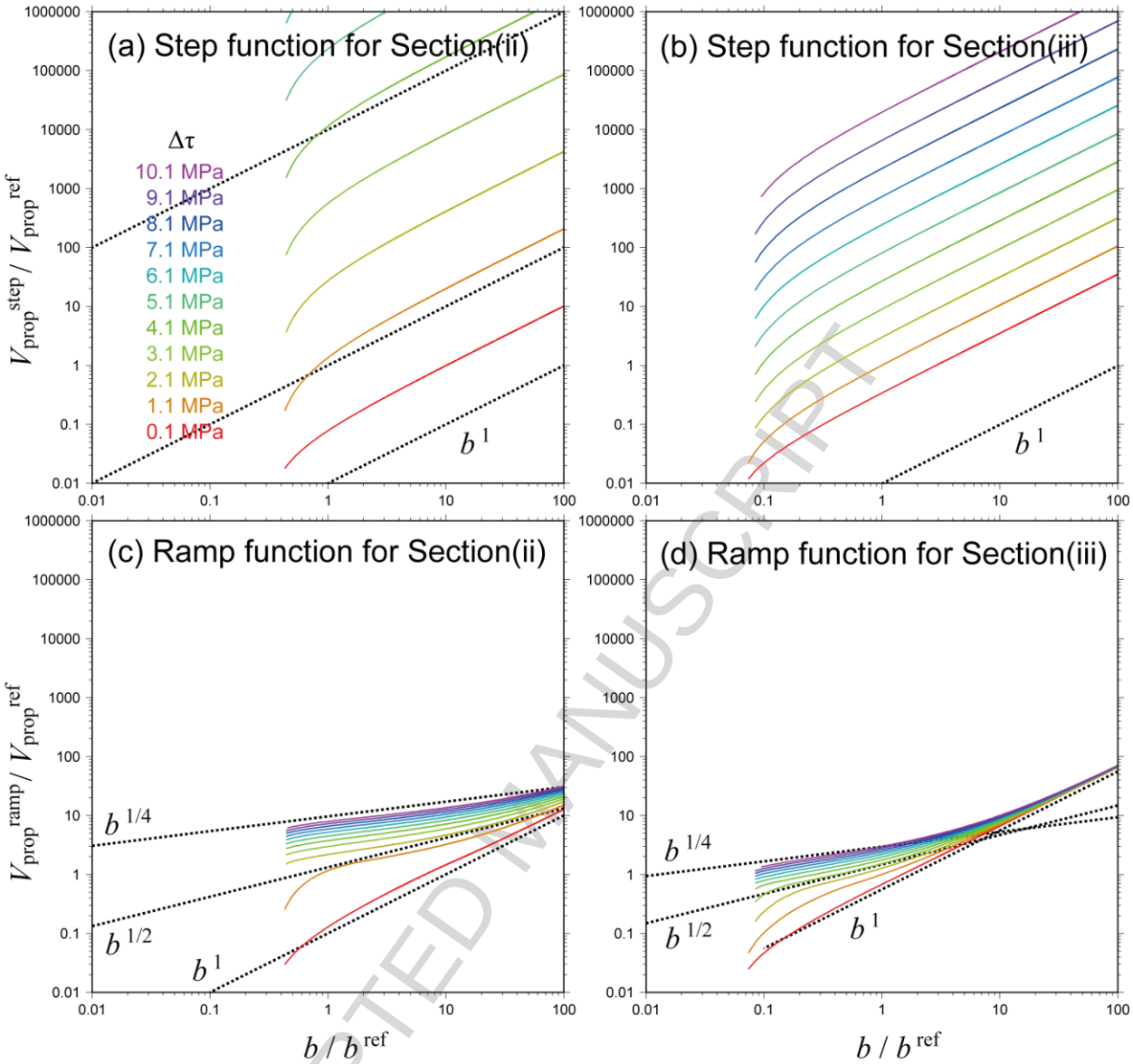

Figure 11. Theoretical relationship between the propagation speed of postseismic slip and frictional parameter "*b*" for two approximations of the shear stress loading, (a, b) step function V_{prop}^{step} and (c, d) ramp function V_{prop}^{ramp}, for (a, c) segment (ii) and (b, d) segment (iii). Colors indicate the amplitude of the shear stress loading.

4.4 Dependence on the frictional parameters $(a\text{-}b)^{const}$ and L

Figure 12 shows the same as Figure 10 but as a function of frictional parameters *a* and *b*, while keeping a constant value of *a*-*b*. by adding the same value to both as $a_{ref}+C$ and $b_{ref}+C$ The results in Figure 12 can be explained as a combination of the results in Figures 10 and 11. For the lower shear stress loading ($\Delta\tau$ = 0.1 MPa), the propagation speed is

approximately independent of the value of a, because a has a largely inversely proportional effect, as suggested by Eq. (36) or Eq. (37) with negligible $\Delta\tau$ (see red curve in Figure 10), that cancels out the linear effect of b. For the higher shear stress loading ($\Delta\tau$ > 0.1 MPa), higher values of a and b make the propagation speed lower, because the exponential dependence on a is stronger than the linear dependence on b. Thus the propagation speed is not simply a function of a-b for fixed $\Delta\tau$ > 0.1 MPa.

Figure 13 shows the same as Figure 11 but as a function of the frictional parameter L. This dependence is explained in almost the same way as the dependence on b. For Models A and F in segment (v), where Δs is the same and we approximately apply $\gamma \approx b/L$ in Eqs. (36, 37) because of $b\sigma/kL$ =17 and 33 (>>1) from Table 3, respectively, $V_{\mathrm{prop}}^{\mathrm{sim}}$ of Model F (L=2cm) is almost twice larger than that of Model A (L=4cm). However, we cannot apply this approximation to other models, because of significantly different value of Δs, $\Delta\tau/a\sigma$. The spatiotemporal change of Δs is discussed in the section of 5.2.

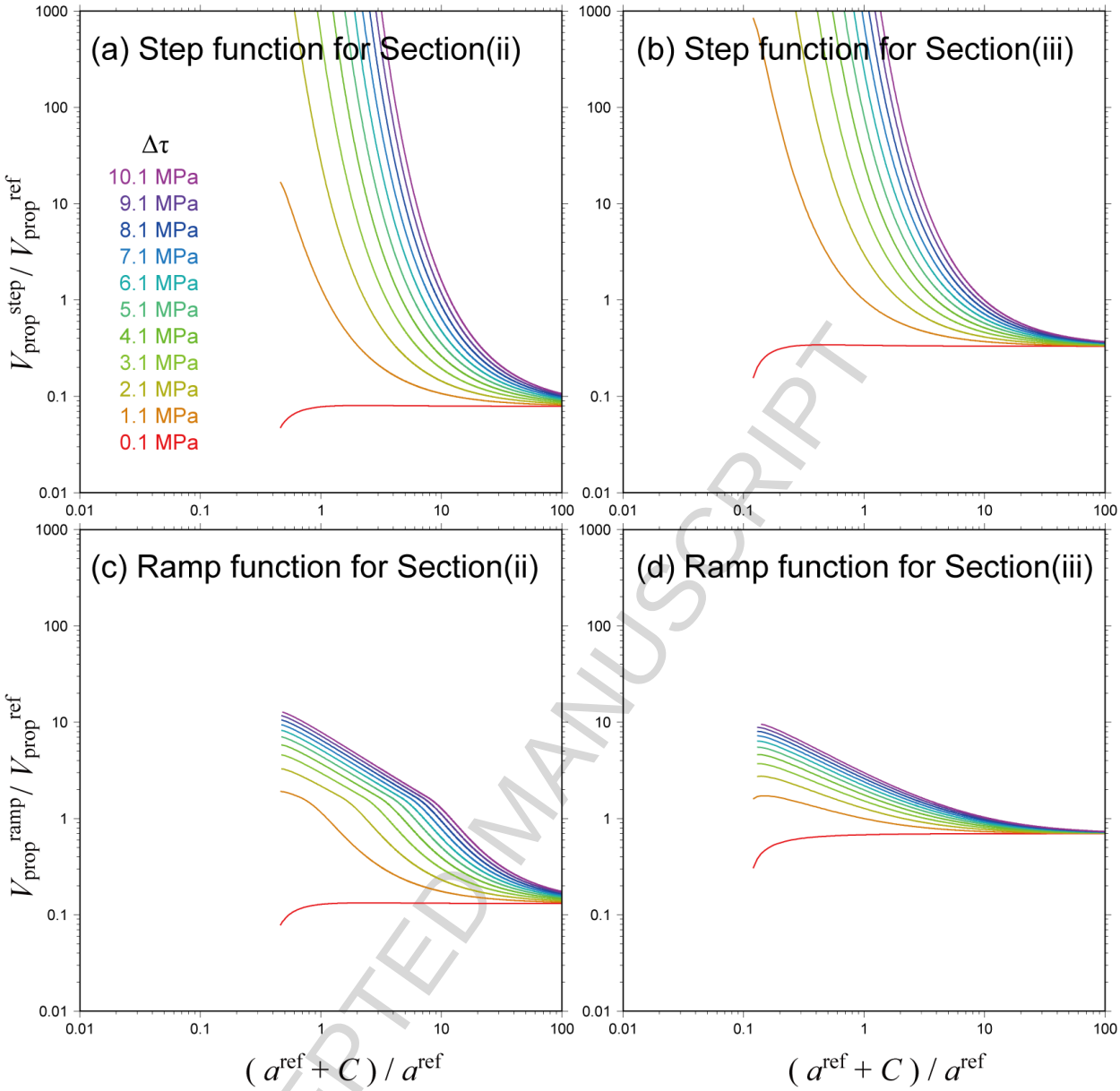

Figure 12. Theoretical relationship between the propagation speed of postseismic slip and frictional parameters "*a*" & "*b*" by adding the same value to both as "*a*+*C*" & "*b*+*C*" under the constant value of (*a*-*b*) for two approximations of the shear stress loading, (a, b) step function V_{prop}^{step} and (c, d) ramp function V_{prop}^{ramp}, for (a, c) segment (ii) and (b, d) segment (iii). Colors indicate the amplitude of the shear stress loading.

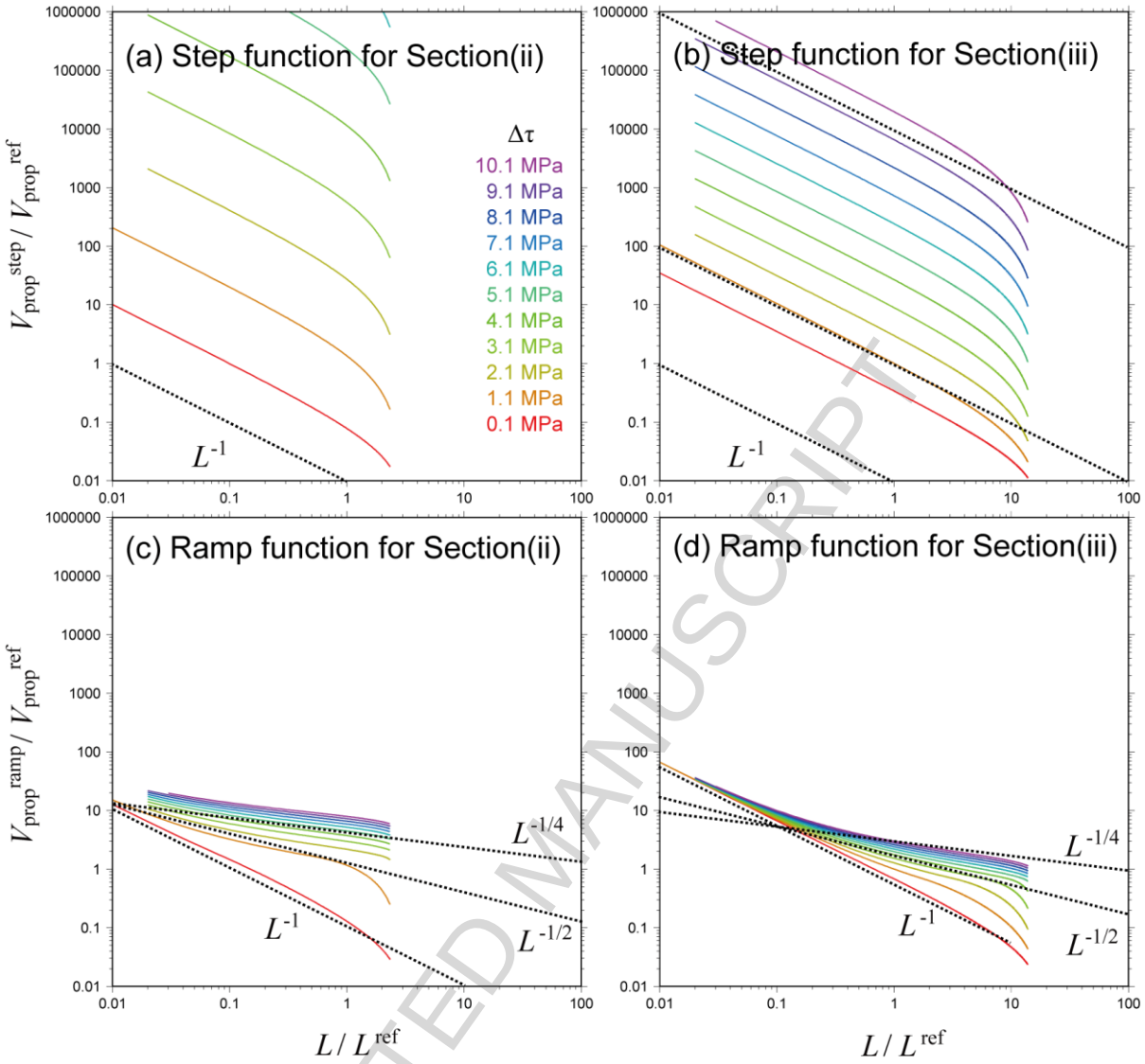

Figure 13. Theoretical relationship between the propagation speed of postseismic slip and frictional parameter "L" for two approximations of the shear stress loading, (a, b) step function V_{prop}^{step} and (c, d) ramp function V_{prop}^{ramp}, for (a, c) segment (ii) and (b, d) segment (iii). Colors indicate the amplitude of the shear stress loading.

5 Discussion

5.1 Validity of approximations and effect of free surface

Though most of our theoretical and simulation results agree within one order of magnitude (Figure 7), we discuss the validity of our approximations in order to understand the remaining discrepancies.

We assumed $V\theta/L >> 1$ in Eq. (13) for the Surge Period. Figure 6 shows the time history of $V\theta/L$. For the segments (iv) and (vi), far from the earthquake rupture area, the shear stress loading is too small and the maximum values of $V\theta/L$ are 1.61 and 1.53, respectively. Hence the approximation is invalid at distant points.

For the shallower segment (i), Figure 7 shows that the analytical propagation speed is much smaller than the simulated one. From Figure 6, the maximum value of $V\theta/L$ at point (i) is 12.8, which is large enough to satisfy our assumption, so the underestimation must be due to other factors. Figures 2b and 2g show that an additional slip front is generated near the surface and propagates in the down dip direction where it encounters the postseismic slip front propagating up-dip from the earthquake source region, as seen in Figure 2d. In this study, we automatically calculate the time of maximum shear stress, without distinguishing these two postseismic slip fronts. This causes our application of the analytical relationship to misestimate the propagation speed in locations where the down-going slip front arrives earlier than the up-going front. From these results, high values of $\Delta\tau/\sigma$ at sufficiently large depth are desirable to apply Eqs. (29, 32, 34).

In this study, our model considers only pure dip slip. We adopted this simplification to limit the computational cost. In our experience, simulations without fixed slip direction on planar faults led to slip almost parallel to the direction of back-slip in all the stages of the earthquake cycle. In strike-slip faults (e.g., Rice, 1993), the artificial slip propagation due to the free surface condition might be moderated because of smaller stiffness for strike slip.

We assumed a hydrostatic depth profile of effective normal stress (Eq. 3). For subduction zones, in-situ drilling observations show that pore pressure is nearly equal to hydrostatic pressure (e.g., Saffer et al., 2015) while it can be nearly equal to lithostatic pressure at seismogenic depth (Hasegawa et al., 2011). Thus the effective normal stress at depth may be much smaller than expected from Eq. (3). If we consider the elevated pore pressure (e.g., Moreno et al., 2014), the propagation speed would be higher than simulation results expected from Eq. (3) as shown in Figure 9. The precise estimation of postseismic propagation speed may independently constrain the depth profile of effective normal stress.

5.2 Spatiotemporal change of the release zone size

As shown in Table 3, the size of Δs is significantly larger than L_b ($b\sigma/kL >> 1$) and different along the fault, even comparing places where the frictional properties are the same. For instance, in all models Δs is larger in segment (iv) than in segment (iii).

Viesca and Dublanchet (2019) demonstrate that slow slip behavior under linear rate-strengthening friction exhibits diffusive spreading of postseismic slip, with slip velocity decaying as $1/t$ and slip growing logarithmically with t. In their result, postseismic slip is self-similar in the sense that it is invariant upon re-scaling of distance and friction between two times T and T' as $X'=XT'/T$ and $\mu'=\mu T/T'$. We use the approximation of $\log(1+\Delta X)\sim\Delta X$ and the same for V in Eq. (4), where we assume the perturbation terms are much smaller than their steady-state values ($\Delta X/X$, $\Delta\mu/\mu$ <<1).

In Figure 14 we assess the self-similarity of the space-time evolution of friction for Models A and I. This figure suggests that the re-scaled curves approximately fit the original ones, which means that the re-scaling roughly explains the time evolution and that the time change of Δs can be explained by the self-similar scaling $\Delta s'= \Delta s\ (T'/T)$. This conversion is only applicable to homogeneous frictional properties, thus not in the along dip direction in our model. In our theoretical relationship, the magnitude of the main shock is reflected in the shear stress loading and the release zone size. For example, for a larger main shock, $\Delta\tau$ is larger and Δs is shorter. However, it is difficult to estimate the release zone size directly from observations. The effect of frictional parameters on Δs is discussed in the next section.

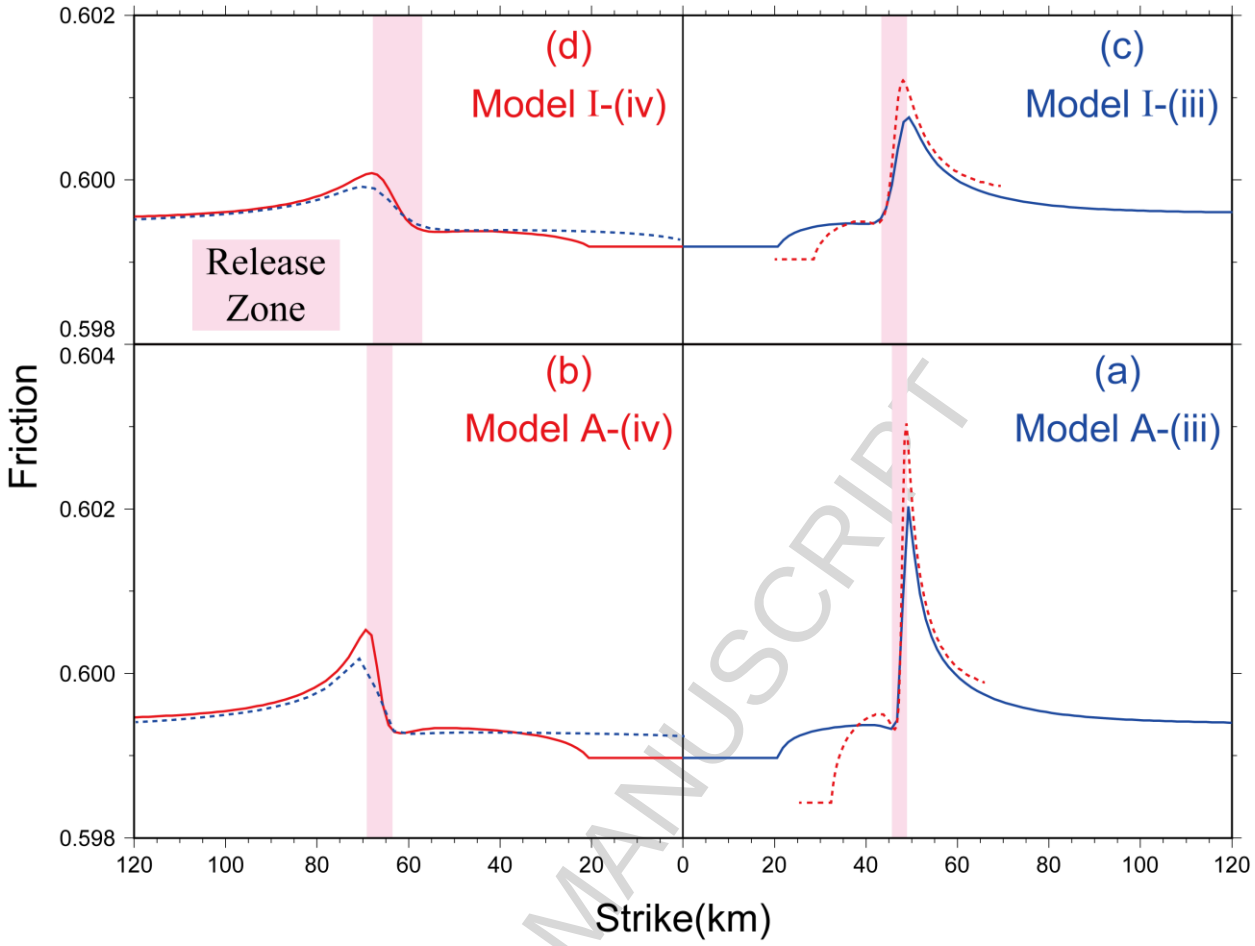

Figure 14. Comparison of spatial distribution of friction coefficient between original (solid) curves at time T and converted (dotted) ones at time T' in segments (iii) and (iv) for Models A and I when friction coefficient has peak value as shown in Figure 5a. The values of (X', μ') for the dotted curves are converted by $X'=X(T'/T)$ and $\mu'=\mu(T/T')$, where the value of T is listed in Table 3.

5.3 Simplified relationship for application to actual observations

As mentioned in section 4.1, it is necessary to know the value of V_{slip}^{init} in order to estimate the propagation speed of postseismic slip. From Figure 6, V_{slip}^{init} is not significantly different among observation points and it is roughly equal to V_{pl}(=2.9×10^{-9} m/sec). Therefore, it can be roughly approximated as

$$V_{slip}^{init} \approx V_{pl}. \qquad (41)$$

Substituting Eq. (41) into Eq. (36) gives

$$V_{prop}^{step} \approx \frac{\eta\gamma G}{ak} \exp\left(\frac{\Delta\tau}{a\sigma}\right) V_{pl} \equiv V_{approx}^{step}, \qquad (42)$$

Figure 15 shows the comparison between V_{prop}^{sim} and V_{approx}^{step} in the same way as in Figure 7. The comparison suggests that V_{approx}^{step} can also explain V_{prop}^{sim} within one order of magnitude over a wide range of slip velocities. Thus the approximation of Eq. (42) is valid in our simulation. This is because $F_{ramp} \approx F_{step}$ between Eqs. (27) and (35) for $kV_b \ll R\sigma$, which means $V_{prop}^{ramp} \approx V_{prop}^{step}$ (From Table 3, for example, we find the lowest value of $R\sigma=\Delta\tau/T$ at Point IV for Model B. In this case, k=1.1MPa/m, $R\sigma=\Delta\tau/T$ =7.4×10^{-9} MPa/sec, and we approximate V_b as V_{pl} = 9 cm/year = 2.8×10^{-9} m/sec, kV_b is about 2.3 times larger than $R\sigma$. Most of other points satisfy $kV_b \ll R\sigma$ because the value of T is much shorter than that at Point IV for Model B).

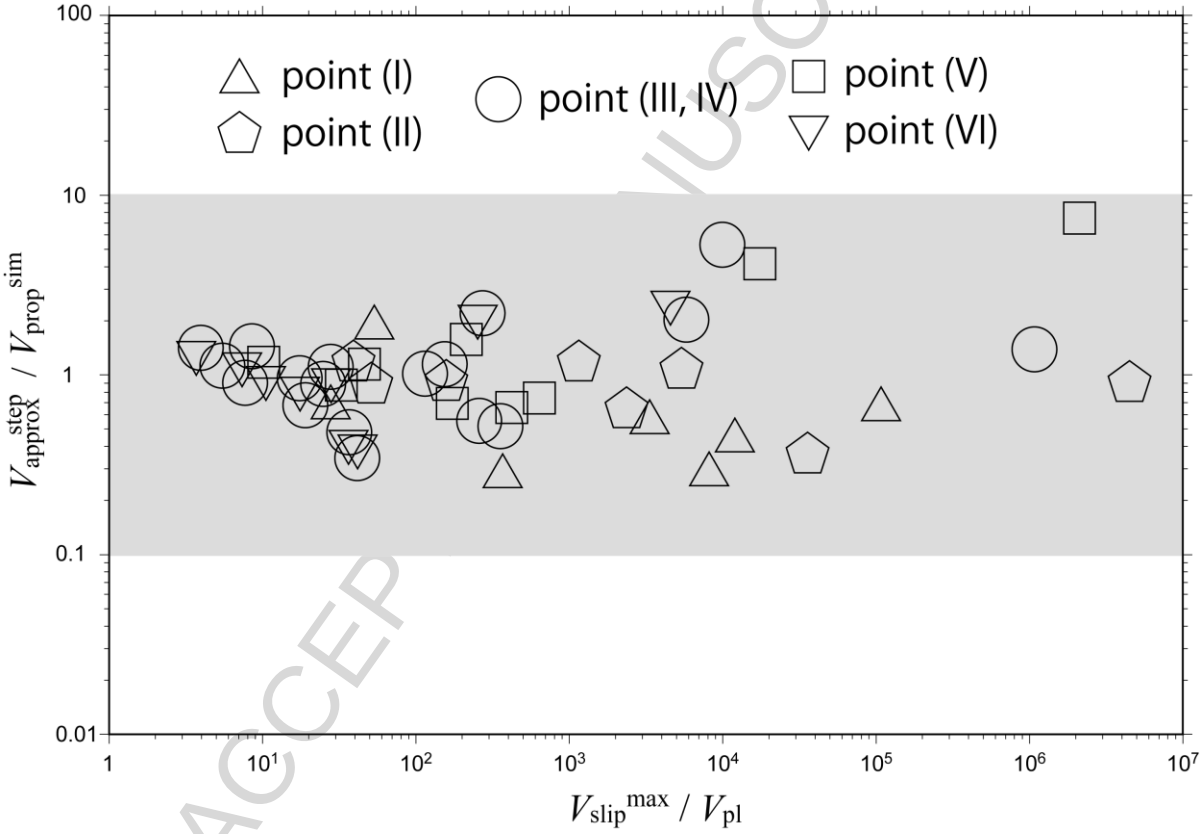

Figure 15. Same as Figure 7 but the approximated V_{prop}^{step} (V_{approx}^{step}: black) in Eq. (42) instead of Eq. (34).

Under that condition, the propagation speed can be roughly approximated by applying Eq. (40) to Eq. (42) as

$$V_{prop}^{step} \approx \frac{\eta bG}{akL}\exp\left(\frac{\Delta\tau}{a\sigma}\right)V_{pl} = \frac{b\Delta s}{aL}\exp\left(\frac{\Delta\tau}{a\sigma}\right)V_{pl} \equiv V_{rough}^{step}. \quad (43)$$

Compared to the test simulation results, V_{rough}^{step} in Eq. (43) describes the main characteristics of the relationship derived from Eq. (34) as follows: (i) the propagation speed is proportional to b/L, (ii) if $\Delta\tau$ is large the propagation speed depends exponentially on $1/a\sigma$, (iii) if $\Delta\tau$ is small the propagation speed is independent of σ and inversely proportional to a.

In the linear loading function case, Eq. (37) is roughly approximated by applying Eq. (40) as

$$V_{prop}^{linear} \approx \frac{\eta bG}{akL} V_{slip}^{init} = \frac{b\Delta s}{aL} V_{slip}^{init} \equiv V_{rough}^{linear}. \quad (44)$$

This is the same as Eq. (44) if $\Delta\tau$=0, but V_{slip}^{init} in Eqs. (37) and (44) may be greater than that of the more abrupt step function. Since the rate of the total shear stress loading is changed from kV_b to $k(V_b + R\sigma/k)$ at t=0, V_{slip}^{init} should be in the range between V_b and $V_b + R\sigma/k$ in case of negligible acceleration. This condition is also true of the ramp function. However, it is difficult to predict the value of V_{slip}^{init} only on the basis of the numerical simulation inputs.

The simplified relationships in Eqs. (43, 44) include the size of release zone (Δs), which is not derived analytically but measured from numerical simulation results. It is difficult to estimate Δs directly from observations. To investigate the dependency of the propagation speed on the size of the release zone from Eq. (43), Figure 16 shows the relationship between the propagation speed normalized by $\exp(\Delta\tau/a\sigma)$ and Δs normalized by L_b, which suggests that the propagation speed is independent of Δs and roughly approximated as

$$V_{prop}^{step} \approx V_{const} \exp\left(\frac{\Delta\tau}{a\sigma}\right) \equiv V_{simple}^{step}. \quad (V_{const} \sim 0.1 \text{ to } 10 \text{ km/month}) \quad (45)$$

This expression also explains the simulated propagation speed within one order of magnitude (1/10 to 10 times difference, as indicated by the gray band in Figure 16) except for the shallowest point. Therefore, $V_{\text{simple}}^{\text{step}}$ is practically applicable to actual observations because it is independent of Δs, though we cannot discuss the dependency on frictional parameters b or L.

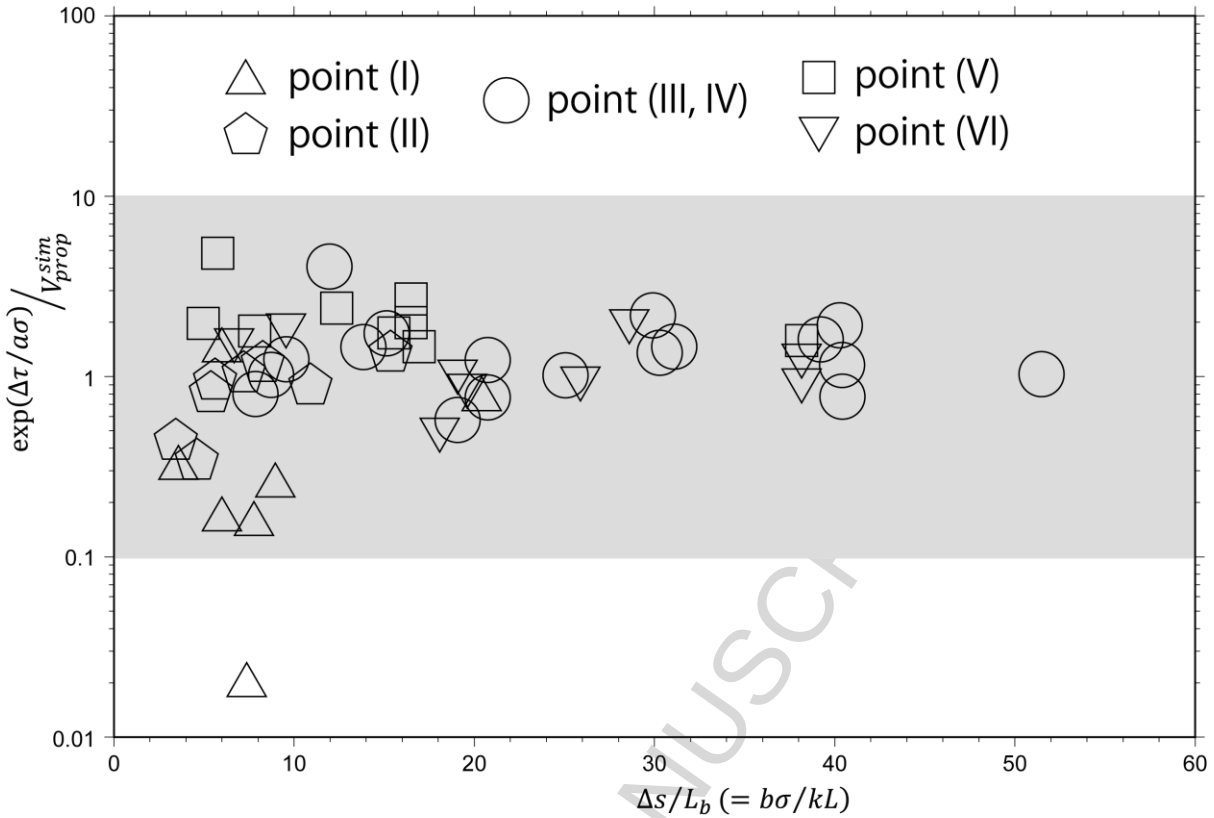

Figure 16. The relationship between $V_{\mathrm{prop}}^{\mathrm{sim}}$ and $V_{\mathrm{simple}}^{\mathrm{step}} = \exp(\Delta\tau/a\sigma)$ as a function of the release zone Δs normalized by critical cell size L_b in case of V_{const} ~ 1.0 km/month. Gray colored background represents the range within one order of magnitude of the simulation results.

From Eqs. (43)(45), Δs is approximately described as a function of frictional parameters:

$$\Delta \mathrm{s} \approx (a/b)\left(V_{const}/V_{pl}\right)L \equiv \Delta \mathrm{s}^{appro}(a,b,L). \quad (46)$$

This expression is useful to estimate the relative size of the release zone in case that we can neglect the effects of σ, $\Delta\tau$, and the spatiotemporal change as discussed in section 5.2. To investigate the validity of Eq. (46), we compare Δs between Models A, D, E, F, and J, where the value of σ is the same each other. Figure 17 shows the relationship between the approximately estimation (Δs_{appro}) for Models (D, E, F, and J) relative to Model A from Eq. (46) and the simulation results (Δs_{sim}). The figure suggests that all the relative size of the release zone for Model D, E, F, and J is well explained in the range of 0.5 to 2.0 times, though we cannot discuss it more quantitatively unless we perform additional models with broad range of the frictional parameters and finer mesh size than this study (Δ_X=1.25km).

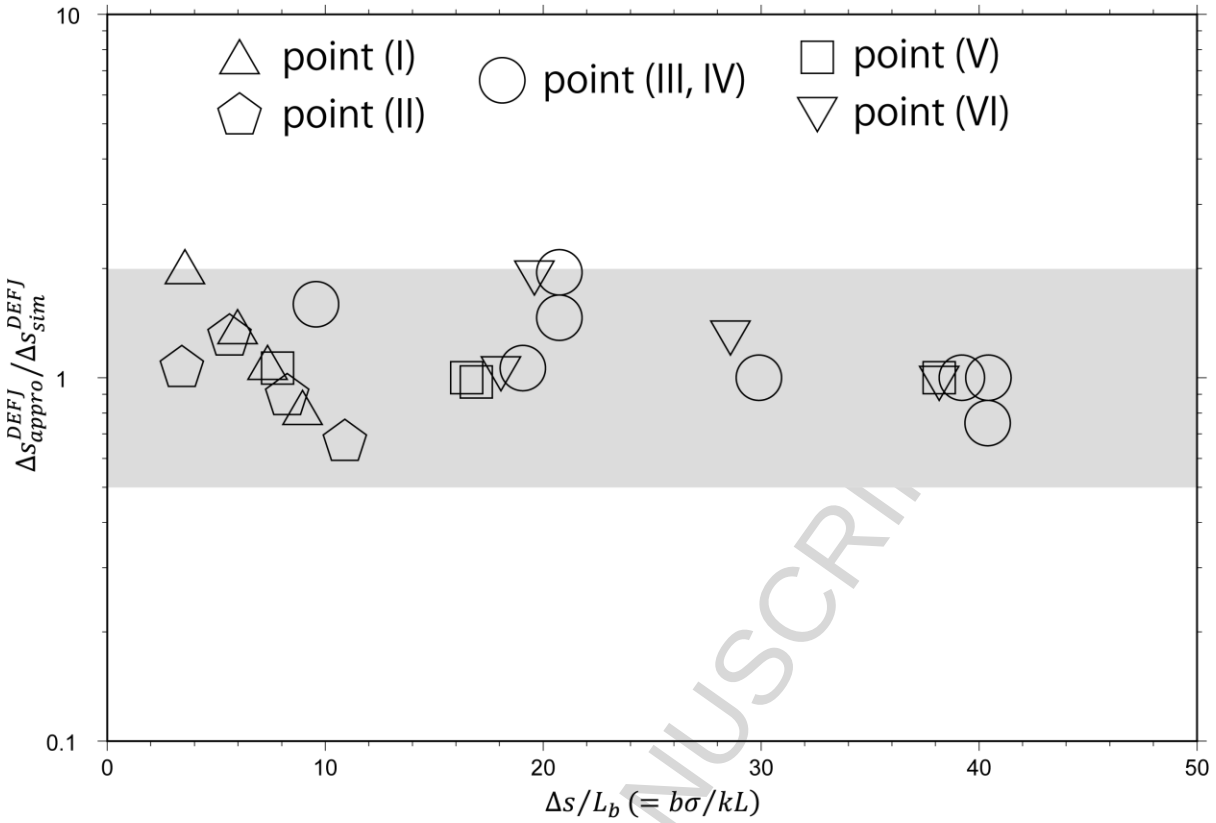

Figure 17. The relationship between approximation from Eq. (46) (Δs_{appro}^{DEFJ}) and the simulated result (Δs_{sim}^{DEFJ}) as a function of the release zone Δs normalized by critical cell size L_b, where Δs_{appro}^{DEFJ} is estimated by $\Delta s_{appro}^{DEFJ} = (a^{DEFJ}/a^{A})(b^{A}/b^{DEFJ})(L^{DEFJ}/L^{DEFJ})\Delta s_{sim}^{A}$. Gray colored background represents the range within twice/half of magnitude of the simulation results.

5.4 Interpretation of previous results on the basis of analytical relationships

As mentioned in the introduction section, previous studies of the effect of frictional properties on propagation speed led to apparently contradictory results. In this section, we interpret those results from the perspective of the insight developed here.

The unsolved problem of whether the postseismic slip propagation depends on $(a\text{-}b)\sigma$ or $a\sigma$ is reconciled as follows. If the rate of shear stress loading is much larger than that of background loading as demonstrated in section 5.3, we rewrite V_{prop} as

$$V_{prop}^{ramp} \approx V_{prop}^{step} \approx \left(\frac{b}{a}\right)\frac{\eta G}{kL}\exp\left(\frac{\Delta\tau}{a\sigma}\right)V_b. \quad (47)$$

If $a\sigma$ is large, the exponential term is close to 1 and $V_{\mathrm{prop}}{}^{(a\text{-}b)\mathrm{const}}$ is nearly constant because both a and b have the same linear effect on propagation speed as shown in Figures 10 and 11 for $\Delta\tau$ = 0.1 MPa. This condition can explain the dependency of V_{prop} on $(a\text{-}b)\sigma$ as

shown in Kato (2004, 2007). If (a-b) is not strongly positive and σ is small, this condition can explain the dependency of V_{prop}^{step} on $a\sigma$ as $\exp\left(\frac{\Delta\tau}{a\sigma}\right)$ in Eq. (47).

Ariyoshi et al. (2007b) pointed out that the effective normal stress is a key parameter of postseismic slip propagation speed because the propagation speed in simulations is faster in the shallower part of subduction zones than in deeper parts, as shown in Figures 2b to 2g. This may be explained by the dependence of propagation speed on effective normal stress found here (see also Figure 9).

From Figure 3, the postseismic slip propagation speed appears independent of distance from the asperity and effective normal stress. This can be explained from Figures 9c and 9d, because V_{prop}^{ramp} is not changed for higher effective normal stress, even if $\Delta\tau$ is large. This characteristic is more predominant for the lower loading rates R' ($=\Delta\tau/\sigma T$) in segments (iv) to (vi) as listed in Table 3.

Postseismic slip is usually much larger than the characteristic slip distance in numerical simulations (e.g., Kato, 2008; Hyodo et al., 2016; Nakata et al., 2016), thus a large part of it may happen near steady-state. But slip in the Surge period, which occurs well above steady state (Eq. 13), is not negligible everywhere, as shown in Figure 5c. In regions with small values of $\Delta\tau/\sigma$, which are far from the main shock rupture or have high effective normal stress, slip remains close to steady state even during the passage of the postseismic front (Figure 6). Thus the steady-state rate-strengthening approximation, equivalent to assume b=0 or L=0 (e.g., Perfettini and Avouac, 2007; Barbot et al., 2009), is more appropriate in the region with small $\Delta\tau/\sigma$. Our theoretical relationship based on V_{simple}^{step} is applicable under the rate-strengthening approximation because Eq. (45) does not involve the state variable. But if the value of $V\theta/L$ is much larger than 1, the delay time between the Surge and Release periods is shorter (Figure 6): the rate-strengthening approximation in Eq. (45) overestimates the delay time in areas where $\Delta\tau/\sigma$ is large. Indeed, Figure 16 shows that V_{simple}^{step} tends to underestimate the propagation speed in the shallower part of the fault (points I and II), while it tends to better explain it in the deeper part (points III to VI).

Hyodo and Hori (2013) adopt a large characteristic slip distance (L=5 m) near the trench as a barrier region and small one (L=5 cm) in the other regions as a source region of megathrust earthquake, where the value of (a-b) is negative for the region shallower than 30 km depth, in order to model complicated earthquake cycles along the Nankai Trough. Their simulation result shows that both coseismic (18 m) and postseismic (4 m) slip reaches the

trench in a M9.0 megathrust earthquake, while only 1 meter postseismic slip propagate there in a M8.6 megathrust earthquake. This can be explained by the critical effective normal stress in Eq. (38). The region near the trench with d_c=5 m has $B = b\sigma$ = 40 and 140 kPa at depth of 5 and 10 km in their model, respectively (Hyodo, private communication). Their length of L_b is about 1.1 and 3.8 $\times 10^3$ km. Since the size of the barrier region is smaller than L_b, it cannot produce slip propagation as modeled by Figure 5d because the distance between the edge of source region for megathrust earthquake and trench is shorter than Δs ($> L_b$), which means $\gamma<0$. Slip propagation in the region of $\gamma<0$ requires sufficient energy of shear stress loading against the resistance force ($kL—b\sigma$), which is driven by slip in the region where large slip has already occurred. The time history of the shear stress loading depends on the slip amount in the region where large slip has already passed and geometrical factors of the region (such as area, focal depth, dip angle, and crack mode). In their simulation, the amounts of shear stress loading for the M8.6 and M9.0 are thought to be smaller and greater than the rest of the resistance force in the region near the trench of the barrier region with L=5 m. This may explain why postseismic slip can occur near the trench only for the M9.0 earthquake, which would be applicable to modeling other frictionally unstable barrier regions (e.g., Hori and Miyazaki, 2010; Nakata et al., 2016). In other words, the shallower part of the 2011 Tohoku earthquake might have low effective normal stress and/or long characteristic slip distance. This quantification is a subject of our future study.

Some afterslip transients exhibit spatiotemporally variable behavior that may provide insight on the spatial variability of friction properties. For instance, following the 2014 South Napa earthquake (Wei et al., 2015; Floyd et al., 2016), afterslip rapidly propagated upward from the main shock source region, but downward propagation was slower and discontinuous, or triggered at some distance, leaving a slip gap between the areas of coseismic slip and deeper afterslip (Floyd et al., 2016). Our relationship suggests that the value of $a\sigma$ on the West Napa Fault increases with depth so that deeper afterslip propagation is slower. The slip gap area could be a frictionally unstable zone (a-b<0) with large characteristic slip distance acting as a barrier.

As demonstrated by observations following the 2011 Tohoku earthquake, postseismic deformation is thought to be a combination of afterslip, viscoelastic relaxation (e.g., Sun et al., 2014; Agata et al., 2019) and poroelastic rebound (Barbot and Fialko, 2010). The contribution to transient deformation due to asthenosphere flow is predominant in the landward surface area (Barbot, 2018), depending on the rheology of the upper mantle and the magnitude of the event

(Lambert and Barbot, 2016). Viscosity is generally different between lower- and middle- crust by a factor of more than ten and its boundary is complicated (e.g., Rousset et al., 2012; Sun et al., 2014). In addition, aseismic slip is thought to account for as much as 50–70% of the slip budget on the seismogenic portion of observed megathrust earthquake cycles (Perfettini et al., 2010). These results indicate that it is important to extract the contribution of afterslip in order to estimate viscoelastic properties from observed crustal deformation.

6 Summary and Conclusions

In this study, we develop theoretical relationships between the propagation speed of postseismic slip and fault-frictional properties on faults governed by rate-and-state friction. The propagating front of postseismic slip is defined as the locus of peak friction coefficient. The theoretical relations provide adequate order-of-magnitude estimates of the results of 3D numerical simulations of afterslip. We derive the following trends:

1. Lower values of effective normal stress σ increase propagation speed exponentially if the amplitude of shear stress loading $\Delta\tau$ induced by the afterslip front is much larger than $a\sigma$. Otherwise, the propagation speed is independent of effective normal stress.
2. The frictional parameter a has a similar exponential effect on propagation speed than σ, but if $\Delta\tau/a\sigma$ is small propagation speed is inversely proportional to a.
3. The propagation speed depends strongly on $a\sigma$ if $\Delta\tau/a\sigma$ is large, on $(a\text{-}b)\sigma$ otherwise.
4. The propagation speed depends linearly on the frictional parameter $\sigma b/L$ under certain conditions.
5. The propagation speed is proportional to the slip velocity ahead of the afterslip front , which in practice can be approximated as the long-term plate velocity V_{pl}.
6. The propagation speed is well approximated as $\frac{\eta bG}{akL}\exp\left(\frac{\Delta\tau}{a\sigma}\right)V_{pl}$, when the shear stress loading rate is much greater than the background loading rate and $\Delta s >> L_{\mathrm{b}}$.

Acknowledgments

We would like to thank Robert Viesca for kindly introducing us to his ongoing research. Discussions at the 10th ACES international workshop were fruitful to improve our model. The present study used the Earth Simulator and the supercomputing resources at the Cyberscience Center of Tohoku University. This study was partly supported by JSPS

KAKENHI Grant Numbers JP 15KK0218, JP15H01148, JP15H04228, JP16H06477, and for Research project for compound disaster mitigation on the great earthquakes and tsunamis around the Nankai trough region. GMT software (Wessel and Smith, 1998) was used to draw a number of the figures.

References

Agata, R., Barbot, S.D., Fujita, K., Hyodo, M., Inuma, T., Nakata, R., Ichimura, T., Hori, T., 2019. Rapid mantle flow with power-law creep explains deformation after the 2011 Tohoku mega-quake. Nat. Commun. 10, 1385, doi:10.1038/s41467-019-08984-7

Ampuero, J.-P., Rubin, A.M., 2008. Earthquake nucleation on rate and state faults—Aging and slip laws. J. Geophys. Res. 113, B01302, doi:10.1029/2007JB005082

Ariyoshi, K., Matsuzawa, T., Hino, R., Hasegawa, A., 2007a. Triggered non- similar slip events on repeating earthquake asperities: Results from 3D numerical simulations based on a friction law. Geophys. Res. Lett. 34, L02308, doi:10.1029/2006GL028323

Ariyoshi, K., Matsuzawa, T., Hasegawa, A., 2007b. The key frictional parameters controlling spatial variations in the speed of postseismic-slip propagation on a subduction plate boundary. Earth Planet. Sci. Lett. 256, 136-146.

Ariyoshi, K., Uchida, N., Matsuzawa, T., Hino, R., Hasegawa, A., Hori, T., Kaneda, Y., 2015. A trial estimation of frictional properties, focusing on aperiodicity off Kamaishi just after the 2011 Tohoku earthquake. Geophys. Res. Lett. 41, 8325–8334, doi:10.1002/2014GL061872

Barbot, S., 2018. Asthenosphere flow modulated by megathrust earthquake cycles. Geophys. Res. Lett. 45, 6018– 6031, doi:10.1029/2018GL078197

Barbot, S., Fialko, Y., Bock, Y., 2009. Postseismic deformation due to the Mw 6.0 2004 Parkfield earthquake: Stress-driven creep on a fault with spatially variable rate-and-state friction parameters. J. Geophys. Res. 114, B07405, doi:10.1029/2008JB005748

Barbot, S. and Fialko, Y., 2010. A unified continuum representation of post‐seismic relaxation mechanisms: semi‐analytic models of afterslip, poroelastic rebound and viscoelastic flow. Geophys. J. Int. 182, 1124-1140, doi:10.1111/j.1365-246X.2010.04678.x

Beeler, N.M., Tullis, T.E., Weeks, J.D., 1994. The roles of time and displacement in the evolution effect in rock friction. *Geophys. Res. Lett.* 21(18), 1987-1990.

Bhattacharya, P., Rubin, A.M., 2014. Frictional response to velocity steps and 1‐D fault nucleation under a state evolution law with stressing‐rate dependence, J. Geophys. Res. Solid Earth 119, 2272‐2304, doi:10.1002/2013JB010671.

Boatwright, J., Cocco, M., 1996. Frictional constraints on crustal faulting. J. Geophys. Res. 101, 13895-13909.

Dieterich, J., 1979. Modeling of rock friction: 1. Experimental results and constitutive equations. J. Geophys. Res. 84, 2161-2168.

Dieterich, J., 1994. A constitutive law for rate of earthquake production and its application to earthquake clustering. J. Geophys. Res. 99(B2), 2601–2618, doi:10.1029/93JB02581

Dublanchet, P., Bernard, P., Favreau, P., 2013. Interactions and triggering in a 3-D rate-and-state asperity model. J. Geophys. Res. Solid Earth 118, 2225‐2245, doi:10.1002/jgrb.50187.

Floyd, M. A., et al., 2016. Spatial variations in fault friction related to lithology from rupture and afterslip of the 2014 South Napa, California, earthquake. Geophys. Res. Lett. 43, 6808–6816, doi:10.1002/2016GL069428.

Gomberg, J., Beeler, N.M., Blanpied, M.L., Bodin, P., 1998. Earthquake triggering by transient and static deformations. J. Geophys. Res. 103(B10), 24411–24426, doi:10.1029/98JB01125

Hasegawa, A., Yoshida, K., Okada, T., 2011. Nearly complete stress drop in the 2011 Mw 9.0 off the Pacific coast of Tohoku Earthquake. Earth Planets and Space 63:35, doi:10.5047/eps.2011.06.007

Hearn, E.H, Bürgmann, R., Reilinger, R.E., 2002. Dynamics of İzmit Earthquake Postseismic Deformation and Loading of the Düzce Earthquake Hypocenter. Bull. Seism. Soc. Am. 92, 172–193.

Hirose, H., Hirahara, K., 2002. A model for complex slip behavior on a large asperity at subduction zones. Geophys. Res. Lett. 29(22), 2068, doi:10.1029/2002GL015825

Hirose, H., Hirahara K., 2004. A 3-D Quasi-static Model for a Variety of Slip Behaviors on a Subduction Fault. Pure Appl. Geophys. 161, 11-12, 2417-2431.

Hussain, E., Wright, T.J., Walters, R.J., Bekaert, D., Hooper, A. Houseman, G.A., 2016. Geodetic observations of postseismic creep in the decade after the 1999 Izmit earthquake, Turkey: Implications for a shallow slip deficit. J. Geophys. Res. 121, 2980–3001, doi:10.1002/2015JB012737

Hyodo, M., Hori, T., Kaneda, Y., 2016. A possible scenario for earlier occurrence of the next Nankai earthquake due to triggering by an earthquake at Hyuga-nada, off southwest Japan. Earth Planets and Space 68(6), doi:10.1186/s40623-016-0384-6

Ida, Y., 1973. The maximum acceleration of seismic ground motion. Bull. Seism. Soc. Am. 63, 959-968.

Kaneko, Y., Fialko, Y., Sandwell, D. T., Tong, X., Furuya, M., 2013. Interseismic deformation and creep along the central section of the North Anatolian Fault (Turkey): InSAR observations and implications for rate-and-state friction properties, J. Geophys. Res. Solid Earth, 118, 316–331, doi:10.1029/2012JB009661.

Kato, N., 2004. Interaction of slip on asperities: Numerical simulation of seismic cycles on a two-dimensional planar fault with nonuniform frictional property. J. Geophys. Res. Solid Earth 109, B12306, doi:10.1029/2004JB003001

Kato, N., 2007. Expansion of aftershock areas caused by propagating post-seismic sliding. Geophys. J. Int. 168, 77-808.

Kato, N. (2008). Numerical simulation of recurrence of asperity rupture in the Sanriku region, northeastern Japan. J. Geophys. Res. 113, B06302, doi:10.1029/2007JB005515.

Konca, A. O., Avouac, J., Sladen, A., Meltzner, A.J., Sieh, K., Fang, P., Li, Z., Galetzka, J., Genrich, J., Chlieh, M., Natawidjaja, D.H., Bock, Y., Fielding, E.J., Ji, C., Helmberger, D.V., 2008. Partial rupture of a locked patch of the Sumatra megathrust during the 2007 earthquake sequence. Nature 456, 631–635.

Lambert, V., Barbot, S., 2016. Contribution of viscoelastic flow in earthquake cycles within the lithosphere - asthenosphere system, Geophys. Res. Lett. 43, 10,142- 10,154, doi:10.1002/2016GL070345.

Lui, S.K.Y., Lapusta, N., 2016. Repeating microearthquake sequences interact predominantly through postseismic slip. Nat. Commun. 7, 13020, doi:10.1038/ncomms13020.

Lui, S.K.Y., Lapusta, N., 2018. Modeling high stress drops, scaling, interaction, and irregularity of repeating earthquake sequences near Parkfield. J. Geophys. Res.: Solid Earth 123, 10,854–10,879, doi:10.1029/2018JB016472

Marone, C.J., Scholtz, C.H., Bilham, R., 1991. On the mechanics of earthquake afterslip, J. Geophys. Res., 96(B5), 8441– 8452, doi:10.1029/91JB00275.

Masuti, S., Barbot, S.D., Karato, S., Feng, L., Banerjee, P., 2016. Upper-mantle water stratification inferred from observations of the 2012 Indian Ocean earthquake. Nature 538, 373-377, doi: 10.1038/nature19783

Miyazaki, S., Segall, P., McGuire, J., Kato, T. Hatanaka, Y., 2006. Spatial and temporal evolution of stress and slip rate during the 2000 Tokai slow earthquake. J. Geophys. Res. 111, B03409, doi:10.1029/2004JB003426

Moreno, M., Haberland, C., Oncken, O., Rietbrock, A., Angiboust, S., Heidbach, O., 2014. Locking of the Chile subduction zone controlled by fluid pressure before the 2010 earthquake. Nat. Geosci. 7, 292–296.

Murakami, M., Suito, H., Ozawa, S., Kaidzu, M., 2006. Earthquake triggering by migrating slow slip initiated by M8 earthquake along Kuril Trench, Japan. *Geophys. Res. Lett.* 33, L09306, doi:10.1029/2006GL025967

#Nakata, R., Hori, T., Hyodo, M., & Ariyoshi, K. (2016). Possible scenarios for occurrence of M~7 interplate earthquakes prior to and following the 2011 Tohoku-Oki earthquake based on numerical simulation. *Scientific Reports*, 6, 25704, doi:10.1038/srep25704

Nagata, K., Nakatani, M., Yoshida, S., 2012. A revised rate- and state-dependent friction law obtained by constraining constitutive and evolution laws separately with laboratory data. J. Geophys. Res. 117, B02314, doi:10.1029/2011JB008818.

Ohnaka, M., Yamashita, T., 1989. A cohesive zone model for dynamic shear faulting based on experimentally inferred constitutive relation and strong motion source parameters. *J. Geophys. Res.* 94, 4089–4104.

Okada, Y., 1992. Internal deformation due to shear and tensile faults in a halfspace, Bull. Seism. Soc. Am. 82, 1018-1040.

Ozawa, S., Murakami, M., Kaidzu, M., Tada, T., Sagiya, T., Hatanaka, Y., Yarai H., Nishimura, T., 2002. Detection and monitoring of ongoing aseismic slip in the Tokai Region, Central Japan. Science 298, 1009–1012.

Perfettini, H., Ampuero, J.-P., 2008. Dynamics of a velocity strengthening fault region: Implications for slow earthquakes and postseismic slip. *J. Geophys. Res*. 113, B09411, doi: 10.1029/2007JB005398.

Perfettini, H., Avouac, J.-P., 2004. Postseismic relaxation driven by brittle creep: A possible mechanism to reconcile geodetic measurements and the decay rate of aftershocks, application to the Chi-Chi earthquake, Taiwan. J. Geophys. Res. 109, B02304, doi:10.1029/2003JB002488.

Perfettini, H., Avouac, J.-P., 2007. Modeling afterslip and aftershocks following the 1992 Landers earthquake. J. Geophys. Res. 112, B07409, doi:10.1029/2006JB004399.

Perfettini, H., Avouac, J.-P., Tavera, H., Kositsky, A., Nocquet, J.-M., Bondoux, F., Chlieh, M., Sladen, A., Audin, L., Farber, D.L., Soler, P., 2010. Seismic and aseismic slip on the Central Peru megathrust. Nature 465, 78-81, doi:10.1038/nature09062

Press, W.H., Flannery, B.P., Teukolsky, S.A., Vetterling, W.T., 1992. Numerical Recipes. 2nd. ed., Cambridge Univ. Press, New York.

Rice, J. R., 1993. Spatio-temporal complexity of slip on a fault. J. Geophys. Res. 98, 9885-9907.

Roland, E., McGuire, J.J., 2009. Earthquake swarms on transform faults. Geophys. J. Int. 178, 1677–1690, doi:10.1111/j.1365-246X.2009.04214.x

Rousset, B., Barbot, S., Avouac, J.-P., Hsu, Y.-J., 2012. Postseismic deformation following the 1999 Chi-Chi earthquake, Taiwan: Implication for lower-crust rheology. J. Geophys. Res. 117, B12405, doi:10.1029/2012JB009571.

Rubin, A.M., 2008. Episodic slow slip events and rate-and-state friction. J. Geophys. Res. 113, B11414, doi:10.1029/2008JB005642

Rubin, A.M., Ampuero, J.-P., 2005. Earthquake nucleation on (aging) rate and state faults. J. Geophys. Res. 110, B11312, doi:10.1029/2005JB003686.

Ruina, A., 1983. Slip instability and state variable friction laws. J. Geophys. Res. 88, 10,359-10,370.

Saffer, D.M., 2015. The permeability of active subduction plate boundary faults. Geofluids 15, 193-215.

Savage, J.C., 1983. A dislocation model of strain accumulation and release at a subduction zone. J. Geophys. Res. 88, 4984-4996.

Shibazaki, B., Shimamoto, T., 2007. Modelling of short-interval silent slip events in deeper subduction interfaces considering the frictional properties at the unstable–stable transition regime. Geophys. J. Int. 171, 191-205.

Sun, T., Wang, K., Iinuma, T., Hino, R., He, J., Fujimoto, H., Kido, M., Osada, Y., Miura, S., Ohta, Y. Hu, Y., 2014. Prevalance of viscoelastic relaxation after the 2011 Tohoku-oki earthquake. Nature 514, 84-87, doi:10.1038/nature13778

Viesca, R. C., Dublanchet, P., 2019. The slow slip of viscous faults. J. Geophys. Res.: Solid Earth 124, doi:10.1029/2018JB016294

Wei, S., Barbot, S., Graves, R., Lienkaemper, J.J., Wang, T., Hudnut, K., Fu, Y., Helmberger, D., 2015. The 2014 Mw 6.1 South Napa Earthquake: A Unilateral Rupture with Shallow Asperity and Rapid Afterslip. Seism. Res. Lett. 86 (2A), 344–354, doi:10.1785/0220140249

Wessel, P. Smith, W.H.F., 1998. New, improved version of the Generic Mapping Tools released. Eos Trans AGU 79, 579.

Table 3. Comparison of simulated propagation speed (V_{prop}^{sim}) and analyzed ones (V_{prop}^{step}, V_{approx}^{step}, V_{prop}^{ramp}, and V_{prop}^{linear}) with some of input parameters (the amount of shear stress change $\Delta\tau$ and total delay time T) and maximum slip velocity normalized by plate convergence rate (V_{slip}^{max} / V_{pl}) at the midpoint of each section. The values of $b\sigma/kL$ and $\frac{k}{\gamma\sigma F_{step}}$ are used for validity of approximations for Eqs. (40, 43, 44) and (36, 37, 39, 42 - 44), respectively.

Seg., Dir.	Depth, σ (km, MPa)	Model	k (MPa/m)	V_{prop}^{sim} (km/month)	V_{prop}^{linear} (km/month)	V_{prop}^{ramp} (km/month)	V_{prop}^{step} (km/month)	V_{approx}^{step} (km/month)	Δs (km)	$\Delta\tau$ (MPa)	T (sec)	V_{slip}^{max} / V_{pl}	$b\sigma/kL$	$\frac{k}{\gamma\sigma F_{step}}$
i dip	4.7 79.4**	A	0.49	87	10	9.9	21	24	10	0.41	2.2e6	367	7.8	1.1e-2
		B	1.1	3.8	1.2	1.2*	2.4	2.5	5	0.98	1.6e7	27.8	20	1.8e-2
		C	0.32	2.6e+3	546	435	934	1121	15	0.48	5.7e4	1.2e4	6.0	4.7e-4
		D	1.1	477	29	28	96	133	5	0.79	4.1e5	8.14e3	3.6	2.6e-2
		E	0.49	8.6e+3	833	365	4764	5511	10	0.41	1.2e5	1.1e5	7.4	9.5e-4
		F	0.84	3.0e+2	33	33*	145	163	6.25	0.69	5.0e5	3.3e3	9.0	1.7e-3
		G	0.61	—***	5.6e5	3.6e5	7.2e5	8.7e5	20	0.41	7.1e1	4.9e6	5.8	3.7e-7
		H	0.24	—***	3.7e6	8.5e5	1.0e6	2.8e6	20	0.22	1.1e1	1.4e7	1.6	2.2e-6
		J	0.32	4.6	4.6	4.3	7.1	8.4	15	0.29	6.6e6	54	6.0	3.2e-2
ii dip	9.8 166**	A	1.1	32	20	15	25	29	5.0	1.2	4.7e5	158	7.2	4.9e-3
		B	1.4	5.0	2.7	2.5	4.1	4.4	3.75	1.8	2.7e6	51	15	1.0e-2
		C	0.74	1330	796	581	1153	1416	7.5	1.2	1.9e4	5.4e3	5.4	2.1e-4
		D	1.4	284	143	92	150	182	3.75	1.9	5.0e4	2.4e3	3.4	8.1e-4
		E	1.1	6826	3.6e3	1.3e3	1.7e3	2.5e3	5.0	1.3	2.6e3	3.6e4	3.4	1.0e-3
		F	1.4	157	95	79	166	183	3.75	1.6	2.1e5	1.2e3	11	8.1e-4
		G	0.34	1.91e6	6.3e5	4.9e5	1.3e6	1.7e6	15	0.89	54	4.5e6	4.6	4.2e-7
		H	0.24	—***	4.8e6	2.2e6	3.4e6	4.9e6	20	0.47	8.8	1.9e7	3.2	3.2e-7
		J	0.48	10.3	6.0	5.6	11	12	11.25	0.83	3.9e6	39	8.3	1.1e-2
iii strike	26.9 454**	A	0.71	2.4	1.0	1.0*	2.1	2.2	3.75	1.1	1.4e7	25	30	1.0e-2
		B	0.71	2.1	1.33	1.31	1.97	2.03	3.75	1.1	6.4e6	18	31	1.3e-2
		C	0.71	14.6	6.6	6.4	16	17	3.75	1.5	1.3e6	154	15	2.8e-3
		D	1.1	8.1	2.8	2.5	4.3	4.5	2.5	2.1	1.1e7	259	21	1.1e-2
		E	0.71	24	13	8.0	11	12	3.75	1.2	3.3e5	355	9.6	3.9e-3
		F	1.1	5.5	2.73	2.72	5.4	5.6	2.5	1.7	2.2e6	115	40	4.0e-3
		G	0.36	938	2.8e3	2.1e3	4.6e3	5.0e3	7.5	1.5	5.8e3	9.9e3	12	2.4e-5
		H	0.275	1.3e5	3.4e5	1.2e5	1.5e5	1.7e5	10	1.05	59	1.1e6	7.8	3.4e-7

		J	0.36	1.2	0.9	0.9*	1.7	1.8	7.5	0.91	3.2e7	8.6	8.6	1.3e-2
iv strike	26.9 454**	A	0.54	1.7	0.96	0.96*	1.5	1.6	5.0	0.52	4.0e7	7.7	40	1.4e-2
		B	0.43	1.4	1.1	1.1*	1.6	1.6	6.25	0.35	4.7e7	5.5	51	1.4e-2
		C	0.43	5.2	2.4	2.4*	5.6	5.8	6.25	0.76	8.1e6	28	25	7.8e-3
		D	1.1	4.1	0.81	0.81*	1.356	1.413	2.5	1.04	3.3e7	41	21	1.6e-2
		E	0.54	7.0	2.7	2.4	3.2	3.4	5.0	0.64	1.2e7	37	19	1.4e-2
		F	1.1	3.0	1.2	1.2*	2.0	2.1	2.5	0.77	8.8e6	19	40	1.1e-2
		G	0.31	62.4	62	55	127	137	8.75	0.82	3.0e5	273	14	8.7e-4
		H	0.275	1.8e3	4.5e3	2.2e3	3.2e3	3.6e3	11.25	0.68	4.8e3	5.8e3	8.7	7.2e-5
		J	0.275	1.1	0.95	0.95*	1.49	1.52	7.5	0.91	7.8e7	4.0	14	1.5e-2
v dip	44.0 744**	A	2.1	2.3	1.06	1.05	1.9	2.0	2.5	2.2	5.6e6	33	17	1.4e-2
		B	1.4	4.4	3.0	2.8	4.8	5.1	3.75	1.9	2.6e6	46	16	8.9e-3
		C	1.4	13	8.4	8.0	19	21	3.75	2.6	9.9e5	213	12	2.7e-3
		D	2.1	7.2	3.0	2.7	4.5	4.7	2.5	3.5	1.2e6	421	17	6.0e-3
		E	2.1	23	15	10	15	17	2.5	2.8	1.7e6	640	7.8	3.6e-3
		F	4.3	4.9	1.52	1.51	3.2	3.4	1.25	3.0	2.0e6	172	16.5	8.3e-3
		G	1.4	836	2.3e3	1.5e3	2.8e3	3.5e3	3.75	2.6	3.4e3	17520	6.6	3.4e-5
		H	0.61	1.2e5	5.6e5	3.6e5	7.2e5	8.7e5	8.75	1.97	3.4e1	2.1e6	5.8	3.7e-7
		J	1.1	1.1	0.66	0.66*	1.25	1.31	10	0.5	7.8e7	10	10	2.1e-2
vi dip	50.9 861**	A	1.1	1.2	0.93	0.93*	1.4	1.4	5.0	0.79	4.5e7	7.3	38	1.7e-2
		B	0.86	2.3	1.3	1.3*	2.17	2.23	6.25	0.76	2.3e7	11	26	2.0e-2
		C	1.1	3.6	1.6	1.6*	3.2	3.4	5.0	1.2	1.0e7	28	19	1.4e-2
		D	2.1	2.9	0.72	0.72*	1.1	1.2	2.5	1.7	9.0e6	42	20	2.1e-2
		E	1.1	4.9	1.1	1.1*	2.0	2.1	5.0	0.78	1.5e7	36	18	2.4e-2
		F	2.1	2.1	1.0	1.0*	1.7	1.8	2.5	1.2	1.2e7	18	38	1.3e-2
		G	0.86	36	30	27	68	76	6.25	1.5	4.6e5	252	9.5	1.7e-3
		H	0.6	8.2e2	1.9e3	1.1e3	1.8e3	2.1e3	8.75	1.2	9.2e3	4.7e3	6.7	1.3e-4
		J	0.71	0.78	0.70	0.70*	1.01	1.03	7.5	0.78	8.6e7	3.7	29	2.3e-2

* V_{prop}^{ramp} is the same value as V_{prop}^{linear} because of $0 \leq \Delta T^{ramp} \leq \Delta\tau/\sigma R$ in Eq. (25).
** The value of σ is calculated from Eq. (3), which is applicable to Model A, D, E and F. The other Models are applied to the condition listed in Table 2.
*** The value of V_{prop}^{sim} could not be obtained because of spontaneous propagation, which is not applied to Figures ??.

Highlights:

- We derive a new theoretical relation between aseismic slip propagation speed, rate-and-state friction properties and normal stress.
- We quantitatively explain, to first order, the afterslip propagation speed obtained in simulations.
- Key parameters of the propagation speed are shear stress loading, effective normal stress and direct term of the friction law.

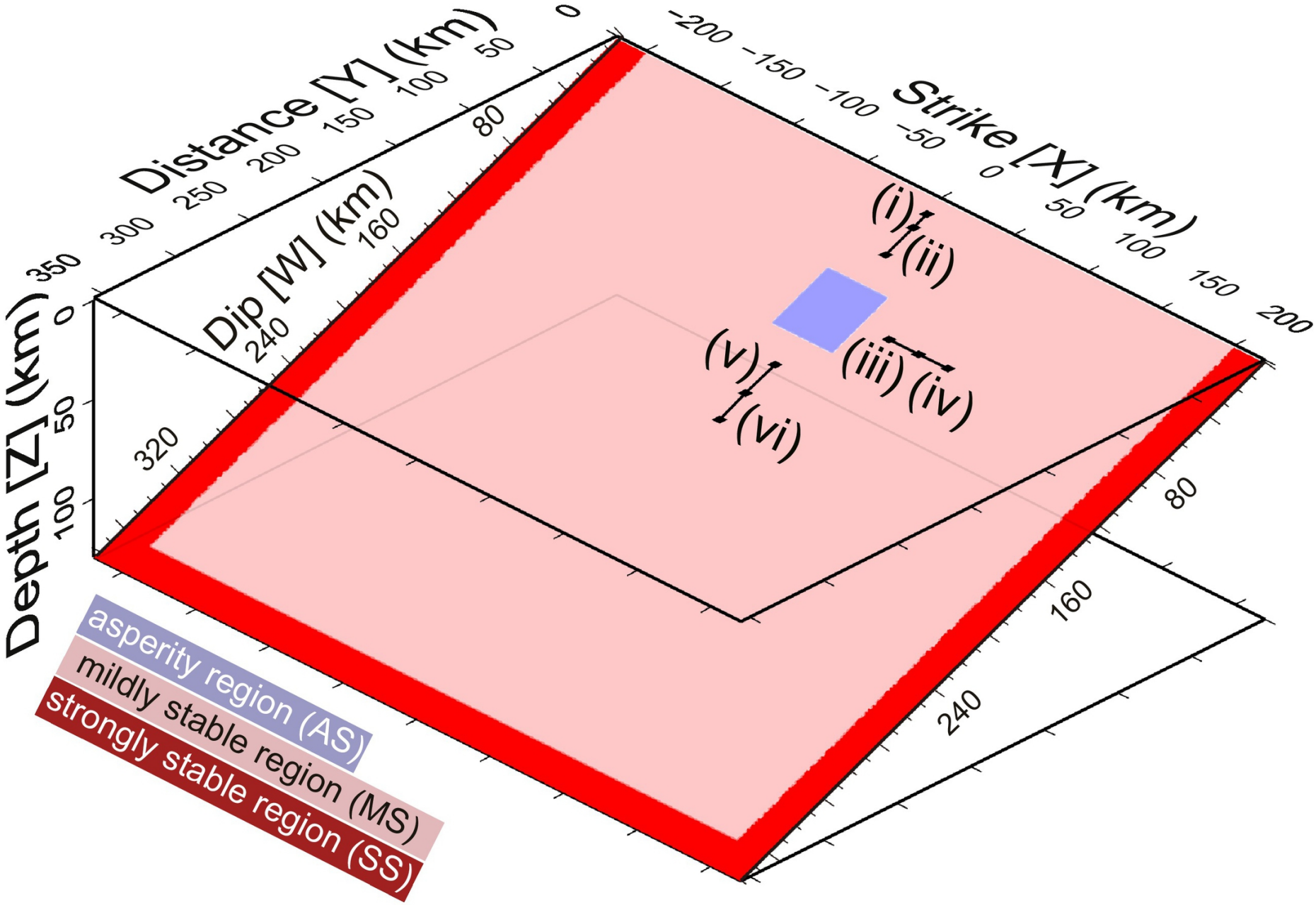
Distance [Y] (km)
0
50
100
150
200
250
300
350
Strike [X] (km)
-200
-150
-100
-50
0
50
100
150
200
Depth [Z] (km)
0
50
100
Dip [W] (km)
80
160
240
320
(i)
(ii)
(iii)
(iv)
(v)
(vi)
asperity region (AS)
mildly stable region (MS)
strongly stable region (SS)

Figure 1

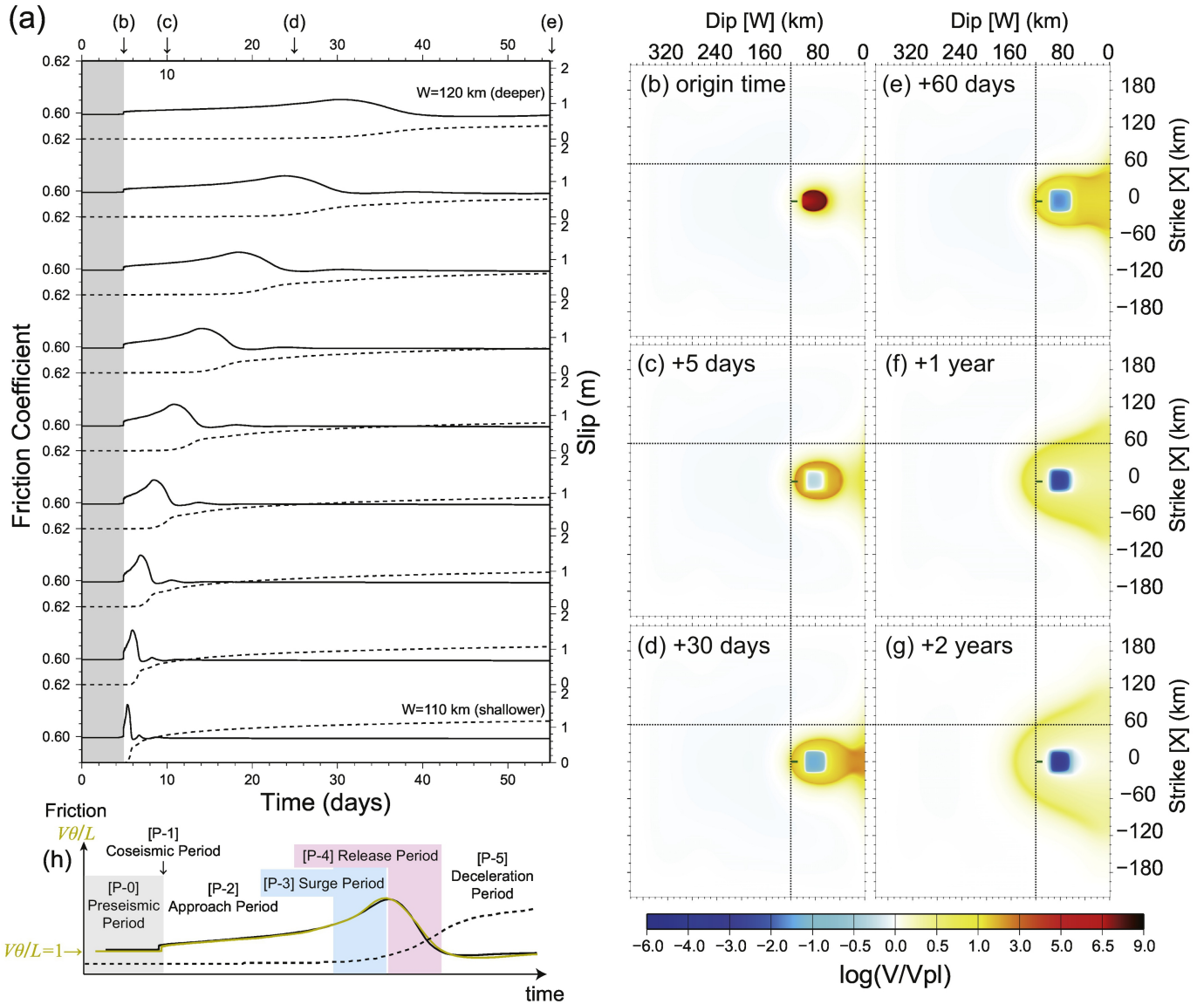
(a)
(b)
(c)
(d)
(e)
W=120 km (deeper)
W=110 km (shallower)
Friction Coefficient
Slip (m)
Time (days)
Friction
Vθ/L
[P-0] Preseismic Period
[P-1] Coseismic Period
[P-2] Approach Period
[P-3] Surge Period
[P-4] Release Period
[P-5] Deceleration Period
Vθ/L=1
time
Dip [W] (km)
(b) origin time
(c) +5 days
(d) +30 days
(e) +60 days
(f) +1 year
(g) +2 years
Strike [X] (km)
log(V/Vpl)

Figure 2

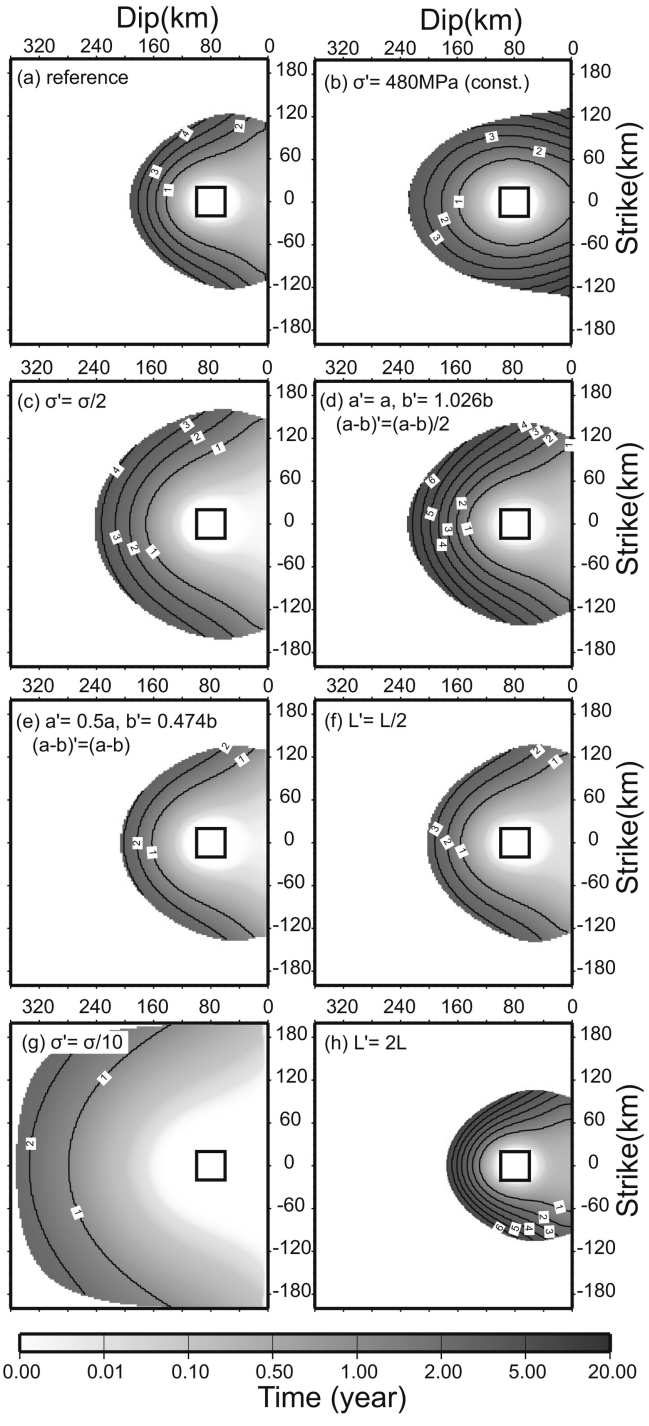
Dip(km)
Dip(km)
320 240 160 80 0
(a) reference
(b) σ'= 480MPa (const.)
(c) σ'= σ/2
(d) a'= a, b'= 1.026b
(a-b)'=(a-b)/2
(e) a'= 0.5a, b'= 0.474b
(a-b)'=(a-b)
(f) L'= L/2
(g) σ'= σ/10
(h) L'= 2L
180 120 60 0 -60 -120 -180
Strike(km)
0.00 0.01 0.10 0.50 1.00 2.00 5.00 20.00
Time (year)

Figure 3

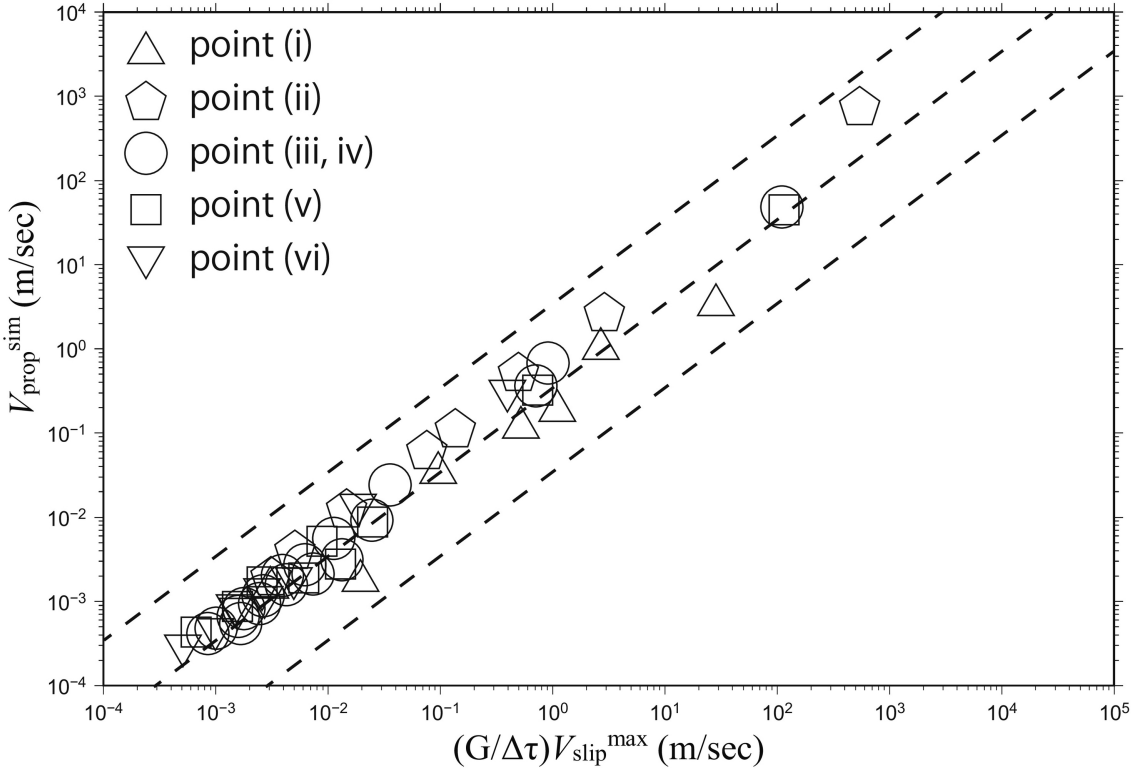
point (i)
point (ii)
point (iii, iv)
point (v)
point (vi)
$V_{\mathrm{prop}}^{\mathrm{sim}}$ (m/sec)
$(G/\Delta\tau)V_{\mathrm{slip}}^{\mathrm{max}}$ (m/sec)
10^{-4}
10^{-3}
10^{-2}
10^{-1}
10^{0}
10^{1}
10^{2}
10^{3}
10^{4}
10^{5}

Figure 4

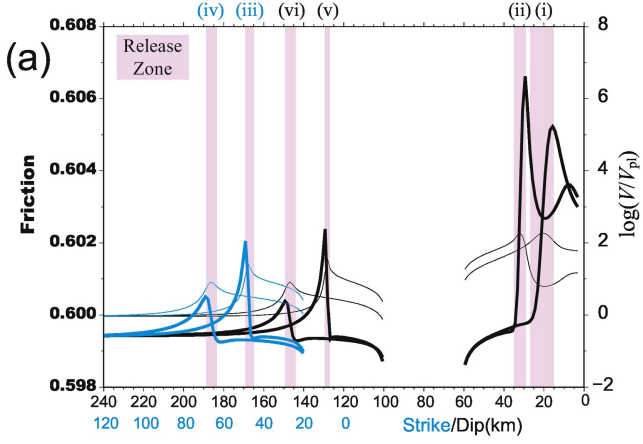
(a)
(iv) (iii) (vi) (v)
(ii) (i)
Release Zone
Friction
0.608
0.606
0.604
0.602
0.600
0.598
8
6
4
2
0
−2
log(V/V_pl)
240 220 200 180 160 140 120 100 80 60 40 20 0
120 100 80 60 40 20 0
Strike/Dip(km)

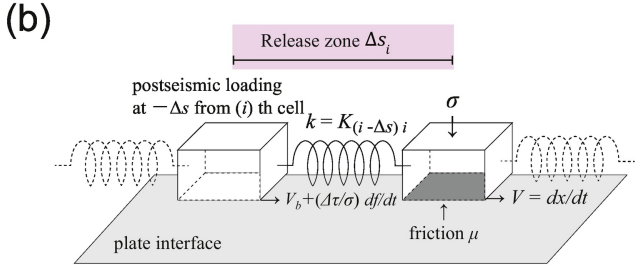
(b)
Release zone Δs_i
postseismic loading
at −Δs from (i) th cell
k = K_(i -Δs) i
σ
V_b+(Δτ/σ) df/dt
V = dx/dt
plate interface
friction μ

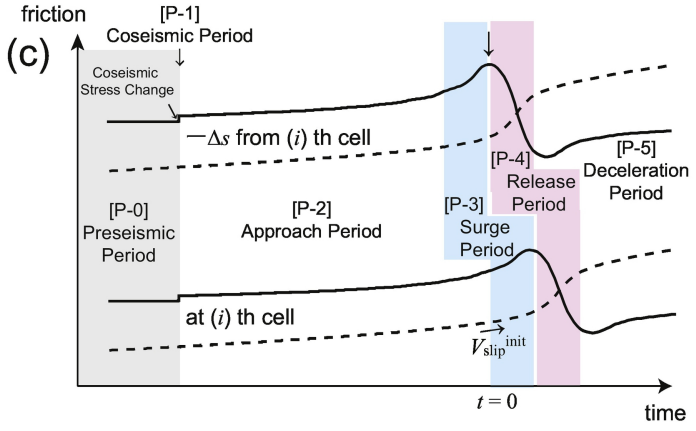
(c)
friction
[P-1]
Coseismic Period
Coseismic Stress Change
−Δs from (i) th cell
[P-0]
Preseismic Period
[P-2]
Approach Period
[P-3]
Surge Period
[P-4]
Release Period
[P-5]
Deceleration Period
at (i) th cell
V_slip^init
t = 0
time

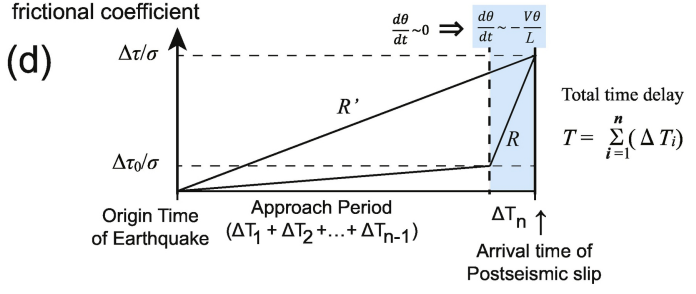
(d)
frictional coefficient
dθ/dt ~0 ⇒ dθ/dt ~ Vθ/L
Δτ/σ
Δτ0/σ
R'
R
Total time delay
T = Σ_(i=1)^n (ΔTi)
Origin Time of Earthquake
Approach Period
(ΔT1 + ΔT2 +...+ ΔTn-1)
ΔTn
Arrival time of Postseismic slip

Figure 5

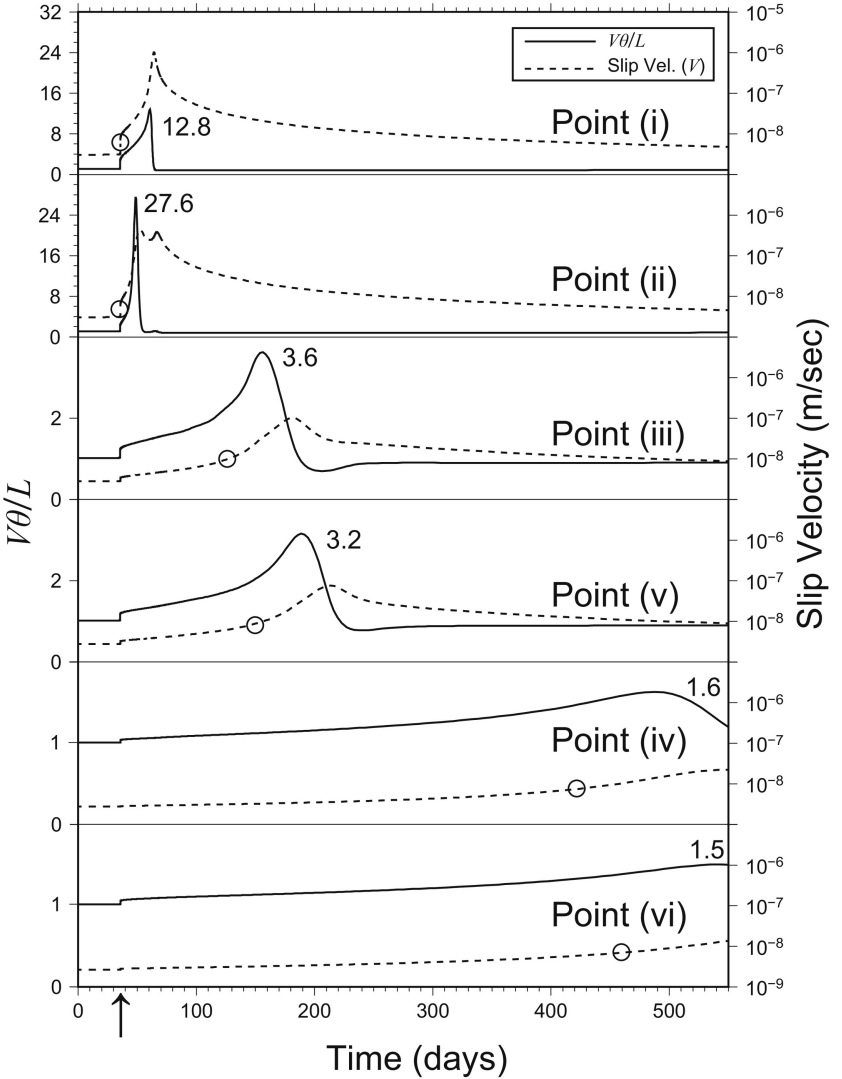
Vθ/L
Slip Vel. (V)
Point (i)
12.8
Point (ii)
27.6
Point (iii)
3.6
Point (v)
3.2
Point (iv)
1.6
Point (vi)
1.5
Vθ/L
Slip Velocity (m/sec)
Time (days)
0
100
200
300
400
500

Figure 6

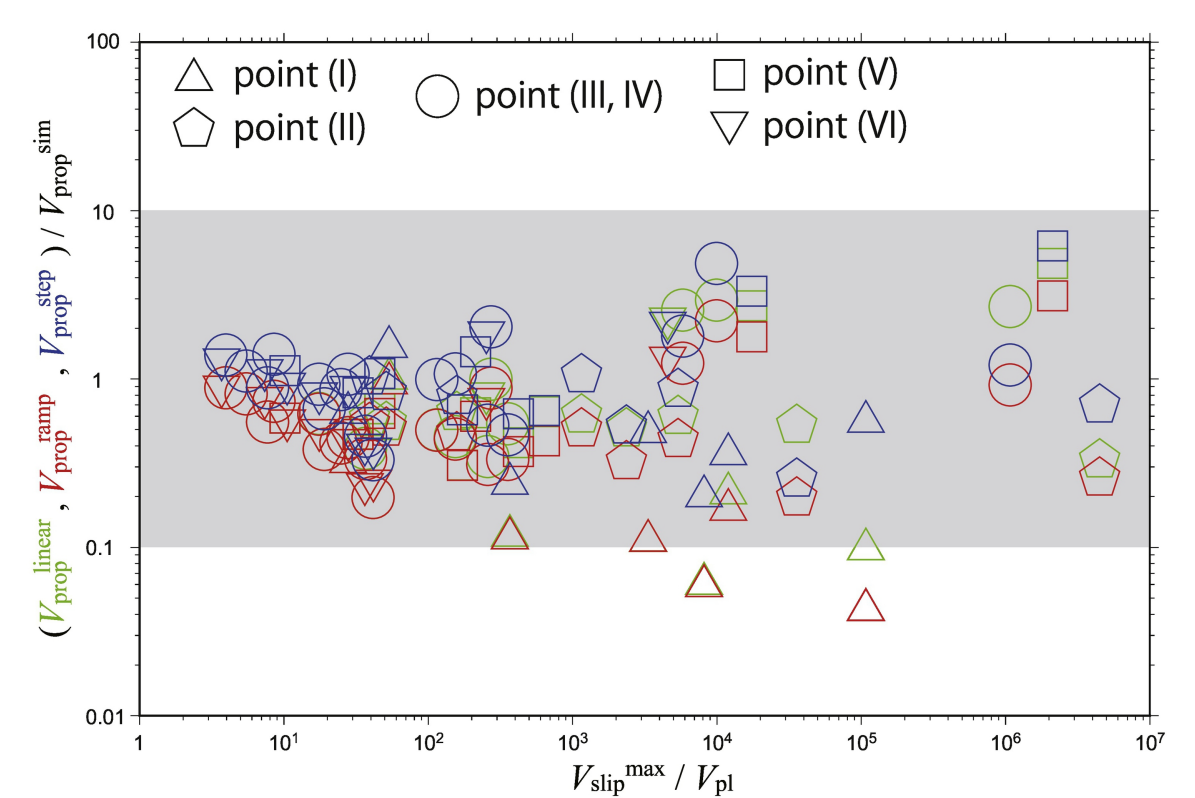
point (I)
point (II)
point (III, IV)
point (V)
point (VI)
100
10
1
0.1
0.01
1
10¹
10²
10³
10⁴
10⁵
10⁶
10⁷
(V_prop^linear , V_prop^ramp , V_prop^step) / V_prop^sim
V_slip^max / V_pl

Figure 7

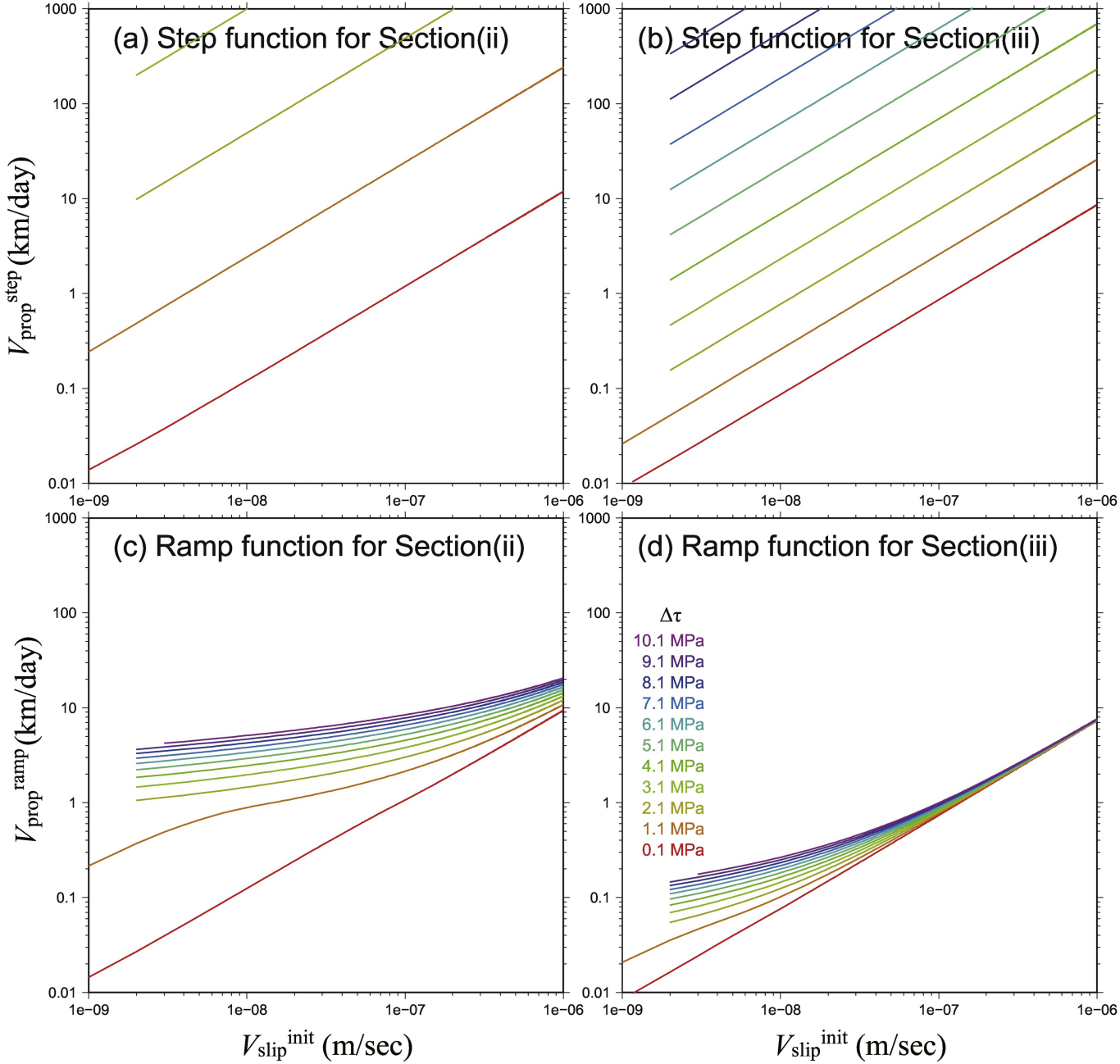
(a) Step function for Section(ii)
(b) Step function for Section(iii)
(c) Ramp function for Section(ii)
(d) Ramp function for Section(iii)
V_{prop}^{step} (km/day)
V_{prop}^{ramp} (km/day)
V_{slip}^{init} (m/sec)
V_{slip}^{init} (m/sec)
1000
100
10
1
0.1
0.01
1e−09
1e−08
1e−07
1e−06
Δτ
10.1 MPa
9.1 MPa
8.1 MPa
7.1 MPa
6.1 MPa
5.1 MPa
4.1 MPa
3.1 MPa
2.1 MPa
1.1 MPa
0.1 MPa

Figure 8

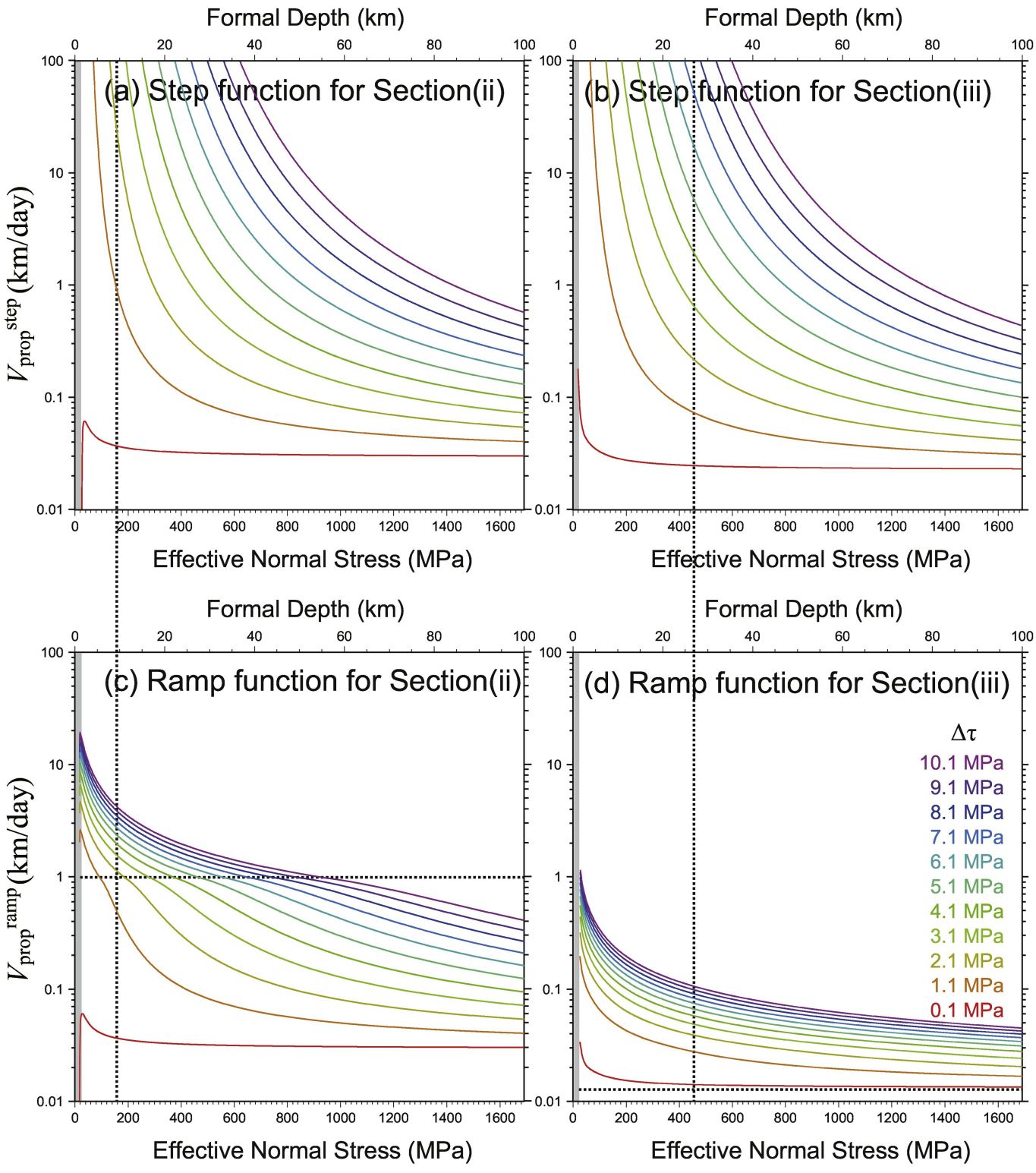
Formal Depth (km)
(a) Step function for Section(ii)
(b) Step function for Section(iii)
(c) Ramp function for Section(ii)
(d) Ramp function for Section(iii)
V_{prop}^{step} (km/day)
V_{prop}^{ramp} (km/day)
Effective Normal Stress (MPa)
Δτ
10.1 MPa
9.1 MPa
8.1 MPa
7.1 MPa
6.1 MPa
5.1 MPa
4.1 MPa
3.1 MPa
2.1 MPa
1.1 MPa
0.1 MPa

Figure 9

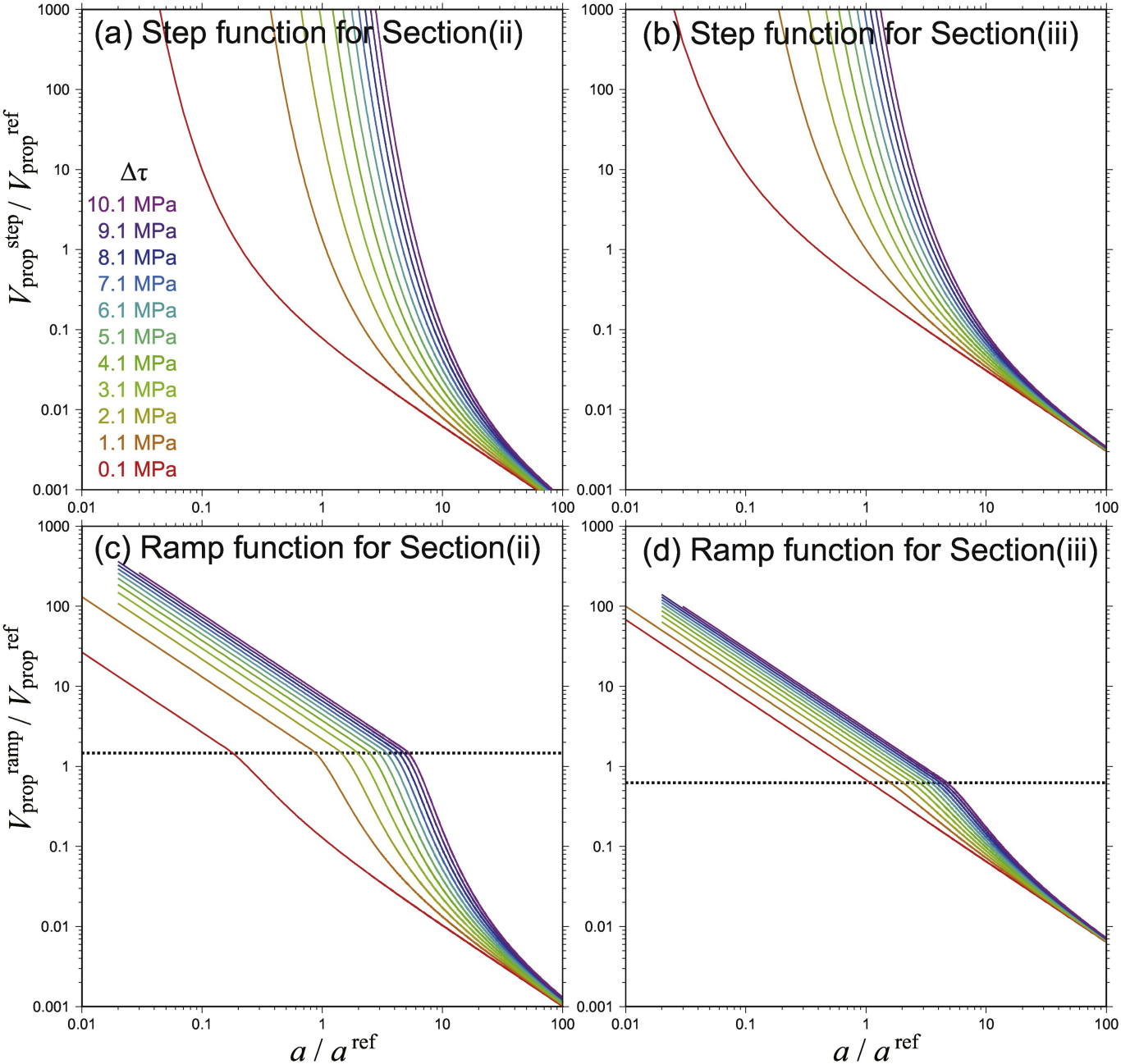
(a) Step function for Section(ii)
(b) Step function for Section(iii)
(c) Ramp function for Section(ii)
(d) Ramp function for Section(iii)
$V_{prop}^{step} / V_{prop}^{ref}$
$V_{prop}^{ramp} / V_{prop}^{ref}$
a / a^{ref}
Δτ
10.1 MPa
9.1 MPa
8.1 MPa
7.1 MPa
6.1 MPa
5.1 MPa
4.1 MPa
3.1 MPa
2.1 MPa
1.1 MPa
0.1 MPa
1000
100
10
1
0.1
0.01
0.001
0.01
0.1
1
10
100

Figure 10

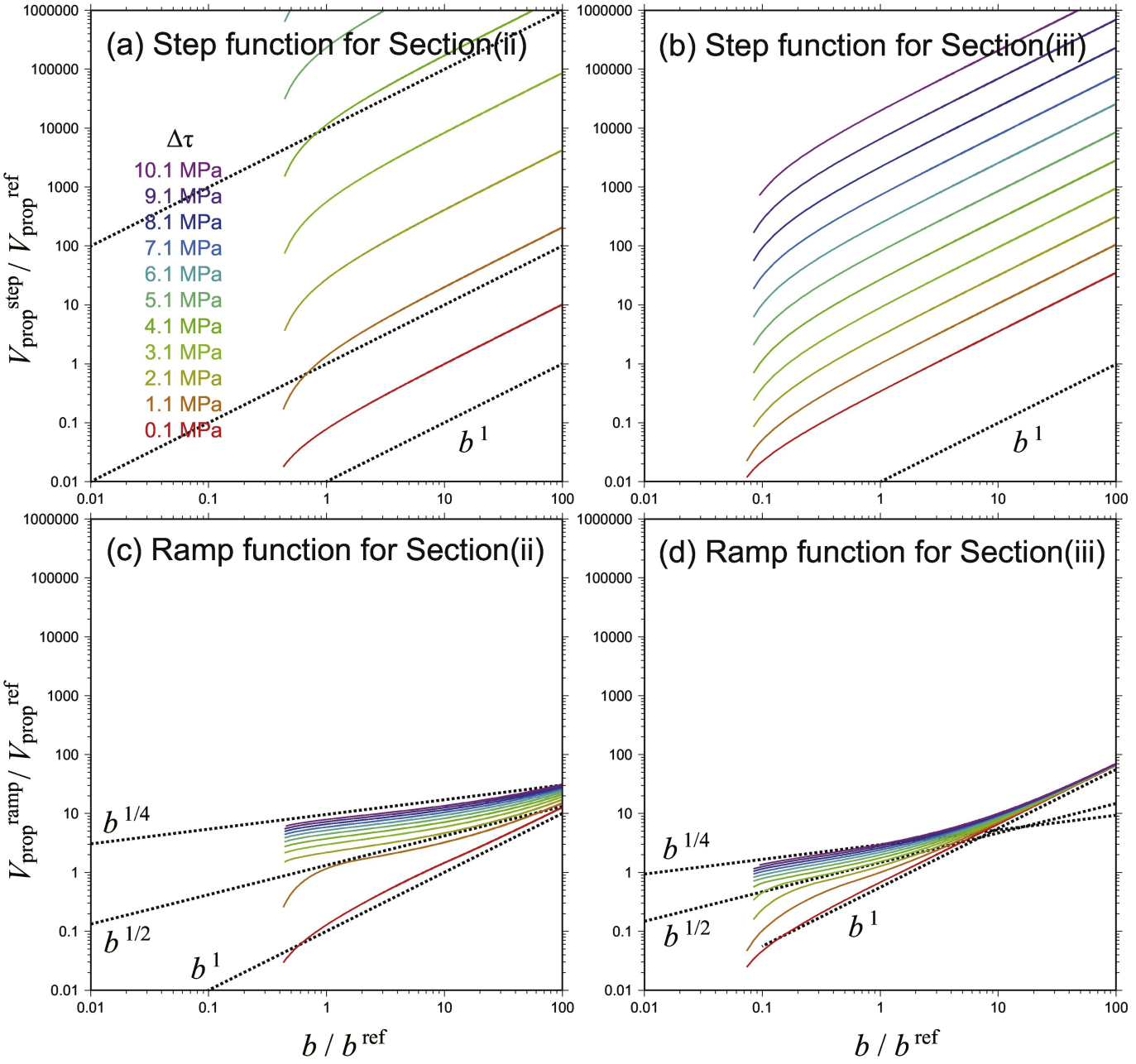
(a) Step function for Section(ii)
(b) Step function for Section(iii)
(c) Ramp function for Section(ii)
(d) Ramp function for Section(iii)
Δτ
10.1 MPa
9.1 MPa
8.1 MPa
7.1 MPa
6.1 MPa
5.1 MPa
4.1 MPa
3.1 MPa
2.1 MPa
1.1 MPa
0.1 MPa
V_prop^step / V_prop^ref
V_prop^ramp / V_prop^ref
b / b^ref
b^1
b^1/2
b^1/4
0.01
0.1
1
10
100
1000
10000
100000
1000000

Figure 11

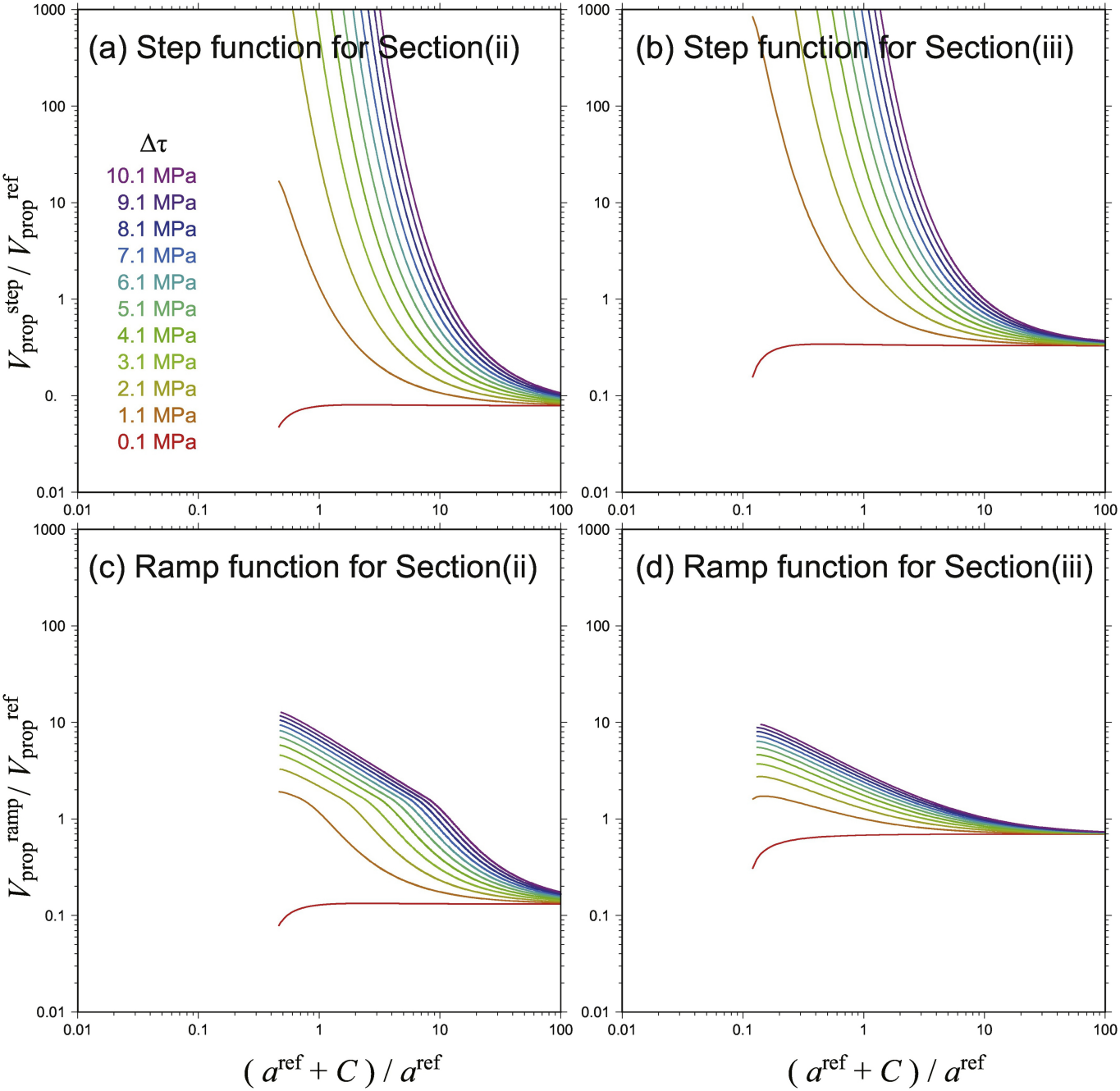
(a) Step function for Section(ii)
(b) Step function for Section(iii)
(c) Ramp function for Section(ii)
(d) Ramp function for Section(iii)
Δτ
10.1 MPa
9.1 MPa
8.1 MPa
7.1 MPa
6.1 MPa
5.1 MPa
4.1 MPa
3.1 MPa
2.1 MPa
1.1 MPa
0.1 MPa
$V_{prop}^{step} / V_{prop}^{ref}$
$V_{prop}^{ramp} / V_{prop}^{ref}$
$(a^{ref} + C) / a^{ref}$
1000
100
10
1
0.
0.1
0.01
0.01
0.1
1
10
100

Figure 12

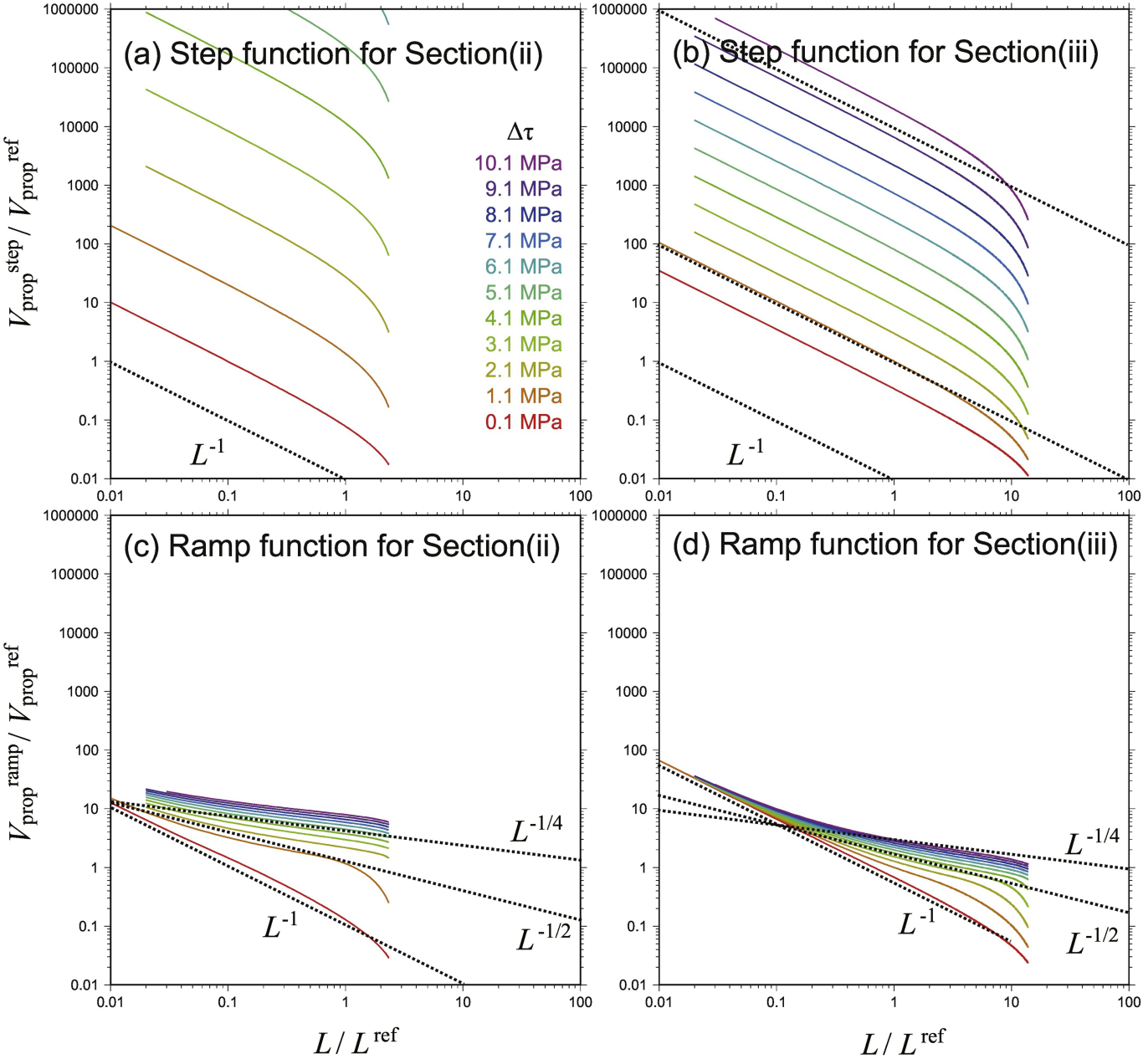
(a) Step function for Section(ii)
(b) Step function for Section(iii)
(c) Ramp function for Section(ii)
(d) Ramp function for Section(iii)
Δτ
10.1 MPa
9.1 MPa
8.1 MPa
7.1 MPa
6.1 MPa
5.1 MPa
4.1 MPa
3.1 MPa
2.1 MPa
1.1 MPa
0.1 MPa
L^-1
L^-1/4
L^-1/2
V_prop^step / V_prop^ref
V_prop^ramp / V_prop^ref
L / L^ref

Figure 13

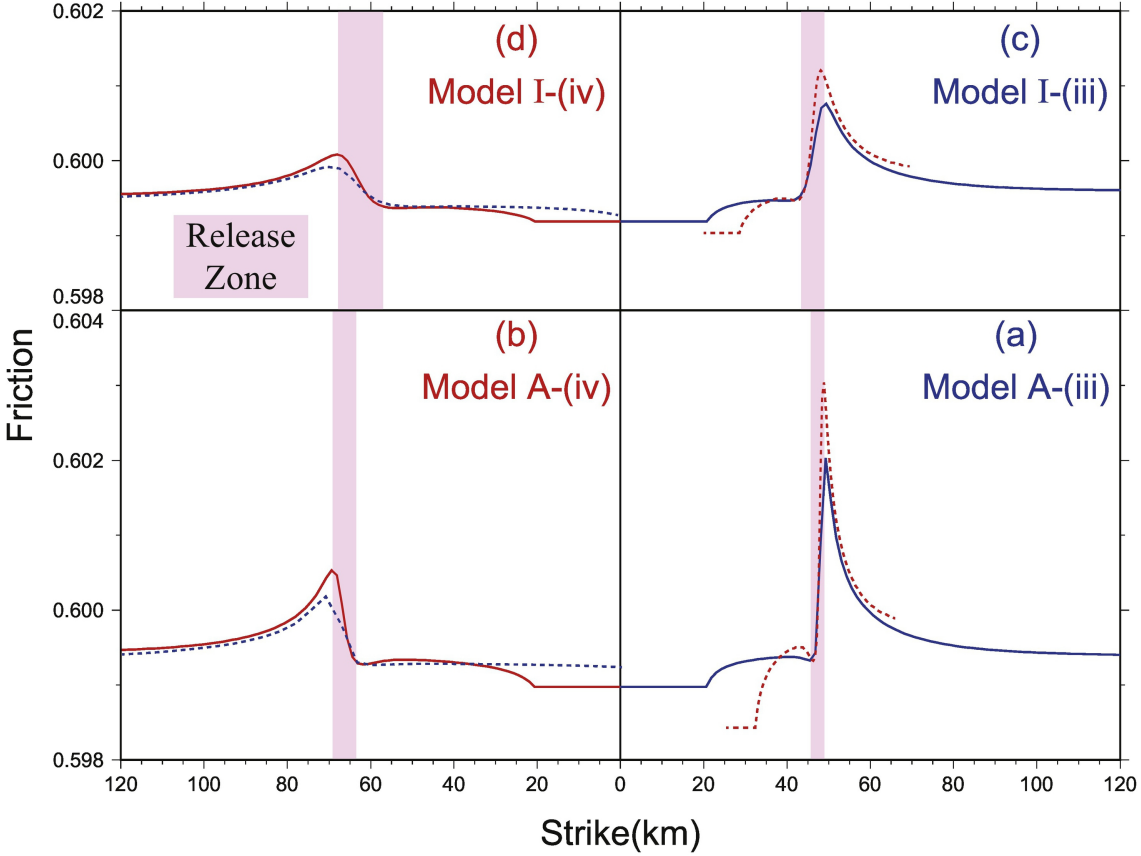
(d)
Model I-(iv)
(c)
Model I-(iii)
Release
Zone
(b)
Model A-(iv)
(a)
Model A-(iii)
Friction
0.602
0.600
0.598
0.604
0.602
0.600
0.598
120
100
80
60
40
20
0
20
40
60
80
100
120
Strike(km)

Figure 14

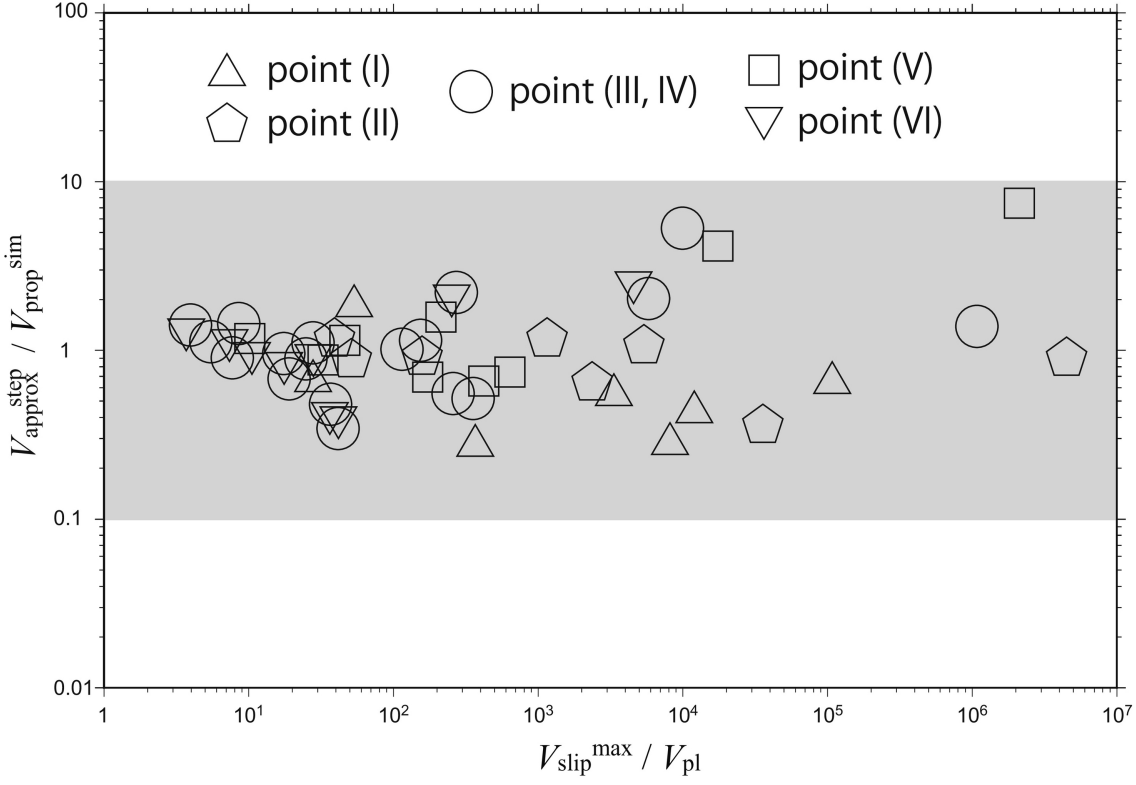
point (I)
point (II)
point (III, IV)
point (V)
point (VI)
100
10
1
0.1
0.01
1
10^1
10^2
10^3
10^4
10^5
10^6
10^7
$V_{\mathrm{approx}}^{\mathrm{step}} / V_{\mathrm{prop}}^{\mathrm{sim}}$
$V_{\mathrm{slip}}^{\mathrm{max}} / V_{\mathrm{pl}}$

Figure 15

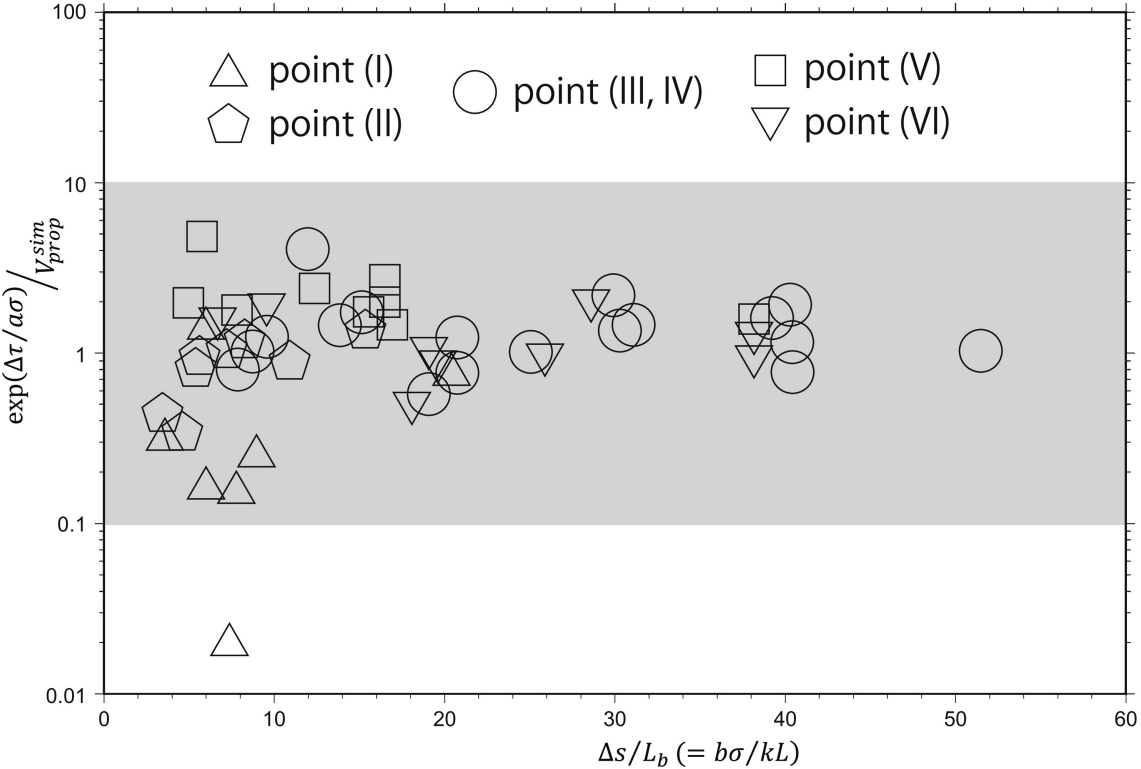
point (I)
point (II)
point (III, IV)
point (V)
point (VI)
100
10
1
0.1
0.01
0
10
20
30
40
50
60
$\exp(\Delta\tau/a\sigma)/V_{prop}^{sim}$
$\Delta s/L_b\ (= b\sigma/kL)$

Figure 16

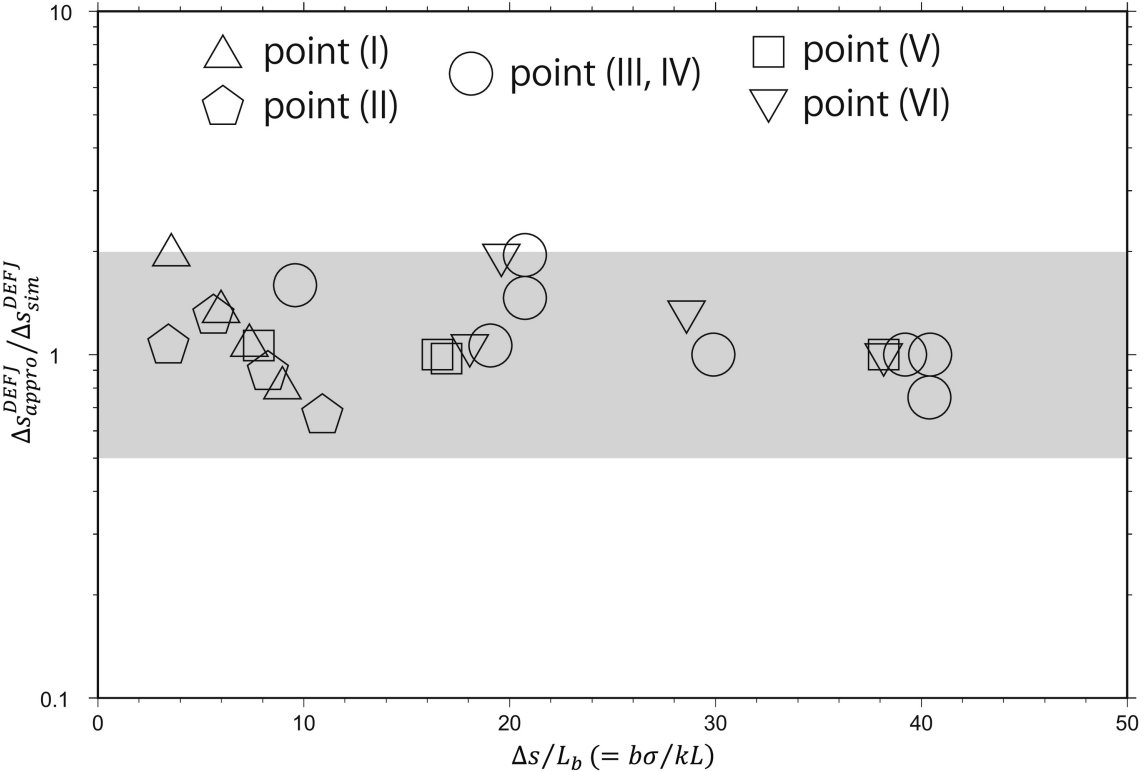
point (I)
point (II)
point (III, IV)
point (V)
point (VI)
10
1
0.1
0
10
20
30
40
50
$\Delta s_{appro}^{DEFJ} / \Delta s_{sim}^{DEFJ}$
$\Delta s / L_b \ (= b\sigma / kL)$

Figure 17